# UNIVERSITY OF READING
Department of Meteorology
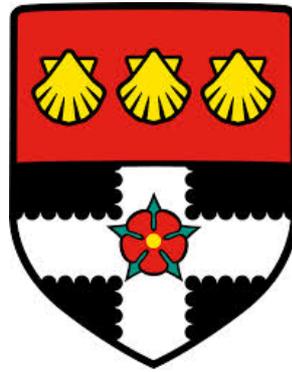
The Generation of Mechanical Work by Overturning Tropical Circulations

Jan Anthony Kamieniecki

A thesis submitted for the degree of Doctor of Philosophy
July 2018

DECLARATION

I confirm that this is my own work and the use of all material from other sources has been properly and fully acknowledged.

Jan A Kamieniecki

ABSTRACT

Global climate models inadequately represent aspects of tropical convection; many studies that underpin the parametrisation of convection incorporate the interactive effects of large-scale circulations using the Weak Temperature Gradient or Weak Pressure Gradient approximations. This thesis examines the thermodynamic consequences of these approximated circulations, in particular for the generation of mechanical work that they imply. It develops approximate analytical formulae for conversions from potential to kinetic energy by circulations generated by the Weak Temperature Gradient approximation and explores the energetic processes involved. Furthermore, a recently proposed isentropic analytical framework for the mechanical energy budget is extended and applied to results from two coupled cloud resolving models. This confirms that the use of the Weak Temperature Gradient approximation does not introduce any thermodynamic anomalies, and the results produced by the cloud resolving models provide confirmation of the analytical results derived earlier. Scaling arguments for the components of the mechanical energy budget are presented. The same technique is also applied to re-analysis data to show how the mechanical energy generated by circulations such as the Walker and Hadley circulations can be calculated from this data.

ACKNOWLEDGEMENTS

my funding agency NERC (grant number NE/K004034/1). I would like to record my thanks to Springer-Verlag GmbH Germany for permission to copy Figure 1.2 and to the American Meteorological Society for permission to copy Figures 3.3, 3.4, 3.5, A.5, A.6, A.7 and A.8.[1] I am also grateful to ECMWF for making available the re-analysis data used in Chapter 4.

I am conscious of a particular debt to the PhD group in Reading, in particular to my roommates in 2U06 who were so welcoming and supportive, did so much to broaden my understanding of those aspects of contemporary culture that would have otherwise remained an enigma to me and humoured my conceit that age is a socio-cultural construct. I would single out Dr David Flack, who was kind enough to comment on a draft on this thesis. My late father, Andrzej Kamieniecki, inculcated in me the greatest respect for academic endeavour from an early age, and my mother Danuta Kamieniecka taught me by her own example the perseverance and resilience needed to complete a project of this nature.

My wife Dominique Girardini has been extremely supportive of this endeavour in so many ways, despite the numerous constraints that this has imposed on our lives, and our regular interaction over the years has been excellent preparation for the questioning that I underwent in the *viva*. I dedicate this work to her.

Jan Kamieniecki, 21 November 2018

CONTENTS

Contents

CHAPTER 1

INTRODUCTION AND BACKGROUND

1.1 BACKGROUND AND MOTIVATION

Tropical convection plays a central role in "driving" atmospheric circulation. It acts by concentrating the effects of solar heating in relatively confined regions and distributes that heating through a deep layer of the atmosphere. This localized deep heating then results in large-scale circulations that spread the heating across large parts of the globe to balance radiative cooling. Despite its importance, aspects of tropical convection are poorly captured in General Circulation Models (GCMs). The various GCMs used in the Coupled Model Intercomparison Project Phase 5 (CMIP5)[1] show considerable variation in the response of the tropical precipitation signal to changes in temperature in an aquaplanet configuration, as shown in Figure 1.1, reproduced from Stevens and Bony (2013). Furthermore, well-established phenomena such as the Madden-Julian Oscillation (MJO)[2] remain inadequately represented, in spite of considerable research effort expended (Hung et al., 2013; Zhang et al., 2013).

In the tropics, the (apparent) Coriolis force (reflecting the perceived deflection of motion due to the Earth's rotation) is a less significant factor than in higher latitudes, where the significant role of baroclinic eddies is generally well captured in models (Stevens and Bony, 2013). Tropical systems on the other hand, to the extent to which they are not chaotic, or temporary

---

[1]A benchmarking exercise including 20 leading modelling groups and underlying the analyses shown in the IPCC's 5th Assessment report (AR5).

[2]A highly variable oscillation that is the main source of intraseasonal variation in the tropics, particularly the Indian Ocean and Western Pacific, with a time period in the range 30-60 days.
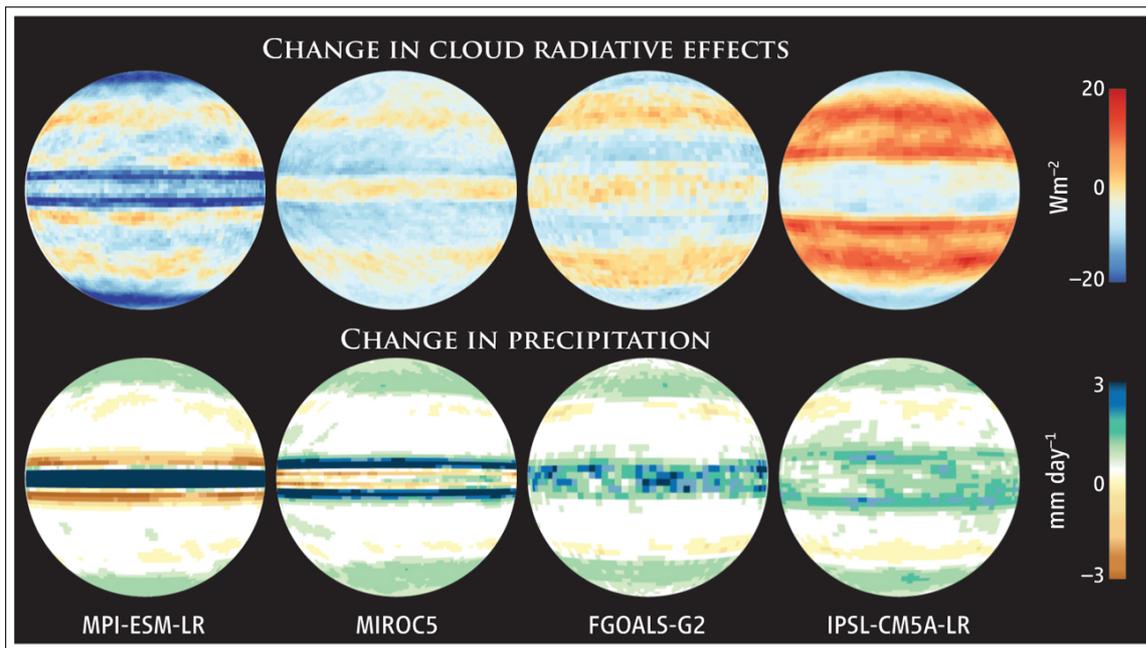
Figure 1.1: *Responses in cloud radiation and precipitation to a 4 K increase in uniform temperature in various CMIP5 models for a simplified aquaplanet set-up (from Stevens and Bony (2013)).*

features exhibiting high vorticity (such as tropical cyclones) which are subject to the collaborative intensification mechanism suggested by Ooyama (1982), are generally dominated by the balance between convective heating, radiative cooling and the advection of temperature and particularly moisture by the large-scale circulation (Raymond et al., 2015).

Even with current advances in computing power, GCMs largely continue to model convection as a parameterised process. More sophisticated studies over a restricted domain are possible using Cloud Resolving Models (CRMs), but given the two-way interaction with large-scale dynamics, this in turn will often require some parametrisation of large-scale circulations (sometimes referred to as supra-domain paramterisation, following Romps (2012b)). In order to achieve this, a number of different approaches have been proposed, notably (a relaxed form of) the Weak Temperature Gradient (WTG) approximation (see Daleu et al., 2012), but more recently the Damped Gravity Wave (DGW) or Weak Pressure Gradient (WPG) approximation (Romps, 2012b) and a spectrally decomposed variant of the WTG (Herman and Raymond, 2014). These parametrisations typically study a local domain ("test column") in conjunction with a reference profile with pre-determined characteristics, and diagnose a vertical

large-scale circulation in the test column based on temperature differences between the two. A number of researchers have tested aspects of these large-scale parametrisations, notably Romps (2012b,a) and also the Global Energy and Water Cycle Exchanges (GEWEX) international intercomparison project (see Daleu et al., 2015b, 2016), but no thorough analysis has been carried out of the fundamental energetics of these different approaches.

This thesis addresses that gap, looking at the energy cycle implied by parametrisations of a large-scale overturning circulation such as the WTG and WPG approximations, with a particular focus on the generation of kinetic energy that they imply. A number of different methodologies have been used in parallel, including an analytical treatment and the use of a simplified radiative/convective model as well as CRMs. Two related research questions are central to this project:

1. What are the local thermodynamic consequences of different coupling strategies?

2. What rate of conversion of Available Potential Energy (APE) into kinetic energy can be produced by overturning circulations in a coupled model?

1.2 TROPICAL CONVECTION AND THE ATMOSPHERIC ENERGY CYCLE

The incidence of solar radiation on the Earth's surface gives rise to an uneven distribution of incoming radiative energy with an annual mean maximum in the tropics, largely due to geometric considerations, but enhanced by the albedo effect at the polar caps. One consequence is that heat is exported from the tropics to the cooler regions (see e.g. Figures 6.14 and 6.15 in Peixoto and Oort (1992)) by both the oceans and the atmosphere (Carissimo et al., 1985; Trenberth and Caron, 2001).

In the atmosphere, important components of this transport include the Hadley cell, a zonal mean overturning circulation with large-scale ascent over the Inter-Tropical Convergence Zone (ITCZ) and descent in the subtropics, and a secondary circulation in the mid-latitudes (sometimes referred to as the Ferrel cell), where eddy fluxes transport heat and momentum poleward, associated with the ascent of cooler air at around 60° (Schneider, 2006). In addition, the tropical circulation exhibits zonal asymmetries, notably ascent over the Maritime Continent

in the West Pacific where surface temperatures are particularly high and descent over the East Pacific (the Walker cell). Anomalies in the Walker circulation, are closely linked to different phases of the El Niño Southern Oscillation (ENSO) (Philander, 1990).

The energetic pathways associated with energy transport in the atmosphere are frequently described in terms introduced by Lorenz (1955). Differential heating at the surface gives rise to a potential energy anomaly by creating horizontal temperature gradients in the atmosphere above. The excess of potential energy over a notional minimum energy state is termed Available Potential Energy (APE). This can be subdivided into mean and eddy APE, the latter being based on departures from the zonal average. Mean APE can be converted into eddy APE e.g. by baroclinic eddies in the mid-latitudes. Potential energy is converted into kinetic energy by convective processes as lighter air rises and cooler air descends. It is possible for kinetic energy to be converted back into potential energy, e.g. when cooler air is forced above warmer air. Ultimately, however, the fate of kinetic energy is to be dissipated in the boundary layer of the atmosphere.

A number of studies have estimated numerical values for the energy reservoirs and various conversion terms in the energy cycle outlined above, exhibiting a degree of variability across the studies. In particular, the conversion from mean APE to mean kinetic energy consists of a positive contribution corresponding to the direct overturning Hadley circulation in the tropics offset by a negative contribution arising from the indirect Ferrel mid-latitude circulation and different estimates can result in positive or negative totals, as seen in Figure 1.2. Huang and McElroy (2014) calculate the separate contributions of these two circulations to be 0.39 W m^{-2} and -0.54 W m^{-2} respectively, in total -0.15 W m^{-2}, using MERRA data. This can be compared with the total conversion using the same re-analysis product, albeit for a slightly different period, of -0.06 W m^{-2} or -0.13 W m^{-2} (depending on the calculation method used) shown in Figure 1.2.

All these studies are based on reanalysis data and neglect the role of sub-grid processes. APE is converted also into kinetic energy by smaller-scale processes than those resolved by the re-
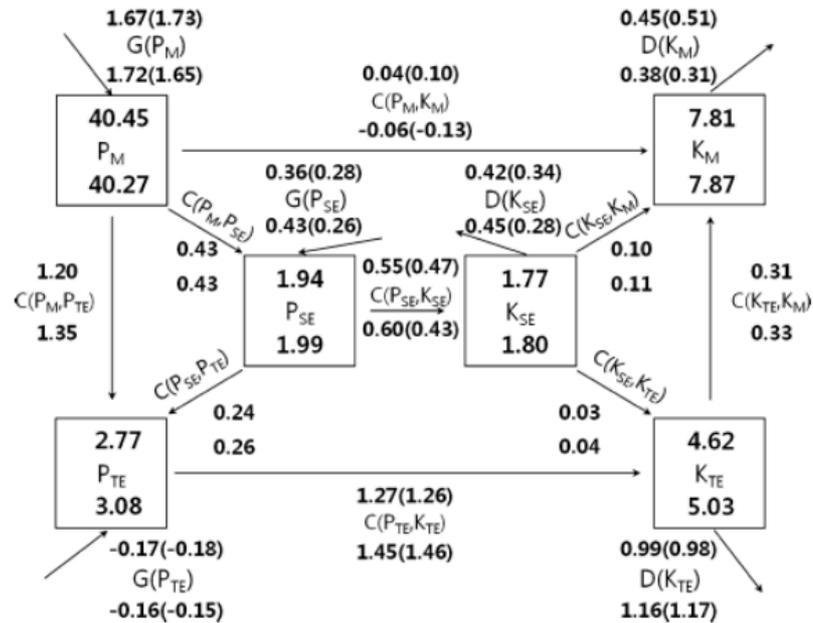
Figure 1.2: *Examples of estimated Lorenz energy cycles from Kim and Kim (2013). P represents APE, K kinetic energy, G generation, C conversion and D dissipation; the subscripts M represent zonal means, SE stationary eddies and TE temporal eddies. The numerical values are based on NCEP R2 (above) and MERRA (below) re-analyses, averaged over the period 1979-2008. The figures in parentheses are calculated using an alternative approach. The units for the reservoirs (P and K) are 10^5 J m^{-2} and W m^{-2} for the other terms.*

analysis data used. Steinheimer et al. (2008) have investigated the effect of including values in respect of the sub-grid elements for a one year run of the ECMWF climate model and produce values for conversion from APE to kinetic energy for the global circulation (mean and eddy combined) approximately twice as large as previously estimated once the sub-grid contribution is included.

There are reasons to believe that greater emphasis on the representation of the conversion process in numerical prediction models could improve their accuracy. For example, Holloway et al. (2013) investigated how well a number of models represent a particular MJO event, and found a correlation between increased generation of kinetic energy and accuracy.

1.3 ENTROPY AND POTENTIAL TEMPERATURE

The concept of entropy in physics was introduced by Clausius (1867) in its classical thermodynamic form, and later interpreted from a statistical perspective (see Boltzmann, 1896). At a fundamental level, the classical form represents the notion that not all the energy in a system is available for conversion into mechanical work - the statistical perspective links this to a notion of microscopic disorder in the system. Although generally accepted as fundamental, entropy remains a somewhat controversial concept [3].

Entropy is central to understanding non-equilibrium thermodynamic systems such as the Earth's atmosphere. Kleidon (2016) suggests that it can provide an organising principle for many of the complex systems that the Earth supports, and links this to the Gaia hypothesis (Lovelock and Margulis, 1974). More quantitative approaches seek to identify constraints that an entropic perspective can introduce to models representing climate features, for example Emanuel (1986) applies it to estimate a limit on the windspeed generated by a hurricane. Another example is the Maximum Entropy Production (MEP) conjecture (Paltridge, 1975), which purports to predict the mean state of the climate, given very weak constraints (see appendix).

An important result that underpins much of this work is the second law of thermodynamics, which in the Clausius version states that heat cannot of itself pass from a cooler body to a hotter body. It can be shown (e.g. Ambaum, 2010) that this is equivalent to the statement by Carnot (1824) that the work done by a theoretical heat engine $\dot{L}$ is limited by the energy input ($\mathcal{F}_{\text{in}}$) and the temperatures at which the energy throughput enters and leaves the system ($T_{\text{in}}, T_{\text{out}}$), thus:

---

[3]This is perhaps most notably expressed in John von Neumann's suggestion to Claude Shannon that he name an attenuation concept in information theory entropy because " ... nobody knows what entropy really is, so in a debate you will always have the advantage." (see Tribus and McIrvine, 1971). Paltridge (2005), one of the earliest advocates of the Maximum Entropy Production (MEP) conjecture (revisited in an appendix) is blunter: "For various rather obscure reasons, 'entropy' is a word that seems to attract the crackpots of the pseudo-scientific societies of the world". This prejudice is not new - Shaw (1930) mentions that "meteorologists generally express aversion from any suggestion to introduce the idea of entropy into meteorological reasoning on the ground that it is an incomprehensible entity which suggests no physical reality and therefore confuses the argument".

$$\dot{L} \le \left(1 - \frac{T_{\text{out}}}{T_{\text{in}}}\right)\mathscr{F}_{\text{in}} \quad . \tag{1.1}$$

Entropy is closely connected to the notion of irreversible transformations, where a physical system cannot subsequently return to its original state without the expenditure of additional energy. Examples of irreversibility in the atmosphere of particular relevance to this thesis include the frictional dissipation of kinetic energy, the mixing of two gases (or the evaporation of liquid into sub-saturated air), the precipitation of cloud water, and the absorption of radiation (Raymond, 2013; Peixoto et al., 1991).

The change of entropy (dS) in a system to which heat dQ is added by a reversible process can be defined by d$S = \frac{\text{d}Q}{T}$, where T is the temperature at which the heat is added. Entropy can be linked to a concept that is much more accepted by meteorologists namely potential temperature, the temperature that would result if dry air were adiabatically transformed to a standard pressure, first introduced by von Helmholtz (1891). Specific entropy for dry air (s) can be expressed as $s = c_p \log \theta / T_0$, where c_p is the heat capacity at constant pressure of dry air and θ is the potential temperature (subject to an arbitrary integration constant, here represented by T_0, the triple point of water). For systems including water in various phases this expression can be expanded to account for the heat stored as a result of phase transitions, but this introduces some further complications in that there is an arbitrary choice to be made for the integration constants for liquid water and water vapour (see Appendix A in Pauluis et al., 2008). The impact of this choice is of little importance where changes in entropy around closed circuits are studied as in this thesis. Yano and Ambaum (2017) argue more broadly that integration constants generally play no physically measurable role in many atmospheric contexts.

Equivalent potential temperature θ_e is a variable that is frequently used in place of moist entropy. A common definition is given in Emanuel (1994):

$$(c_p + r_T c_l)\log \theta_e = s + R_d \log p_0 \quad , \tag{1.2}$$

where R_d is the specific gas constant for dry air and p_0 is a reference pressure. This definition has the drawback of not necessarily being monotonically related with entropy, and alternative definitions have been proposed (e.g. Marquet, 2011). In this thesis, in order to preserve the monotonic relationship with entropy, the $r_T c_l$ term in Equation 1.2 is neglected, and a different integration constant used as in Ambaum (2010):

$$c_p \log^{\theta_e / T_0} = s \quad .$$

(1.3)

It should be noted that s in the above equation is the specific entropy per unit mass of dry air, even though moisture is now included. A Lagrangian analysis of an overturning circulation with varying water content, such as that presented in Chapter 3, is most meaningfully performed from a unit mass of dry air perspective, which will then be weighted by a streamfunction representing the mass flux of dry air to obtain numerical results. Marquet and Dauhut (2018) question whether the label "isentropic" can properly be applied to such an approach.

There is a close inter-relationship between the mechanical work generated by a system and the irreversible generation of entropy. Consider a system which converts the difference between energy input ($\mathscr{F}_{in}$) and output ($\mathscr{F}_{out}$) into mechanical work ($\dot{L}$). Using the weighted average temperature at which energy enters and leaves the system then, following the argument in Ambaum (2010, section 10.3) the irreversible entropy production ($\dot{S}_i$) can be expressed as:

$$\dot{S}_i = \frac{\mathscr{F}_{\text{out}}}{T_{\text{out}}} - \frac{\mathscr{F}_{\text{in}}}{T_{\text{in}}} \quad .$$

(1.4)

It is then possible to decompose the work done as follows:

$$\dot{L} = \mathscr{F}_{\text{in}} - \mathscr{F}_{\text{out}}$$

(1.5)

$$= \left(1 - \frac{T_{\text{out}}}{T_{\text{in}}}\right) \mathscr{F}_{\text{in}} - T_{\text{out}} \left(\frac{\mathscr{F}_{\text{out}}}{T_{\text{out}}} - \frac{\mathscr{F}_{\text{in}}}{T_{\text{in}}}\right)$$

(1.6)

$$= \eta \mathscr{F}_{\text{in}} - T_{\text{out}} \dot{S}_i \quad ,$$

(1.7)

where $\eta = (1 - {T_{\text{out}}}/{T_{\text{in}}})$ is the Carnot efficiency of the system. This is referred to as the Guoy-Stodola equation. The significance of this equation is that it shows that the difference between

the theoretical (Carnot) maximum work output and that actually realised is proportional to the irreversible entropy production.

Pauluis and Mrowiec (2013) analyse convective systems by considering averaged motions in a coordinate system defined by entropy and height. The mechanical energy budget for air parcels following closed paths in such a framework was subsequently expressed by Pauluis (2016) in a form that can be written as:

$$\underbrace{\oint T\mathrm{d}s}_{W_{Tds}} = \underbrace{\oint B\mathrm{d}z}_{W_b} + \underbrace{\oint r_T g\mathrm{d}z}_{W_p} + \underbrace{\sum_{w=v,l,i} \oint (-\mathcal{G}_w)\mathrm{d}r_w}_{\Delta\mathcal{G}}, \quad , \tag{1.8}$$

where B is the buoyancy of the parcel, z the height, g the acceleration due to gravity, r_T the total water mixing ratio and r_w the mixing ratio for each of the three phases of water ($w = v, l, i$) and $\mathcal{G}_w$, the Gibbs function or chemical potential. This is defined for the three phases of water as follows:

$$\mathcal{G}_v = c_l \left(T - T_0 - T\log\frac{T}{T_0} \right) + R_v T\log(\mathcal{H}) \quad , \tag{1.9}$$

$$\mathcal{G}_l = c_l \left(T - T_0 - T\log\frac{T}{T_0} \right) \quad , \tag{1.10}$$

$$\mathcal{G}_i = c_l \left(T - T_0 - T\log\frac{T}{T_0} \right) - L_{f0} \left(1 - \frac{T}{T_0} \right) \quad , \tag{1.11}$$

where c_l is the heat capacity of liquid water, T_0 is its triple point temperature, R_v is the specific gas constant for water vapour, $\mathcal{H}$ is relative humidity and L_{f0} is the specific freezing enthalpy of water. W_{Tds}, the left hand side of Equation 1.8, can be interpreted as the Carnot maximum work done by the parcel as it completes its circuit in $s-T$ coordinates. W_b, the first term on the right hand side can be shown to be the increase in kinetic energy arising as a result of warmer air convecting upwards and displacing cooler air, in other words the generation of mechanical energy by the system, and is referred to as the buoyancy term. W_p ("the elevator term") is the increase in the potential energy of total water lifted by the system, and $\Delta\mathcal{G}$ is the lost part of that work that is needed to evaporate liquid water at below saturation into the system in order to maintain the mean humidity profile against the hydrological cycle and is referred to as the "Gibbs penalty" by Pauluis who discusses it in detail in Pauluis and Held (2002a,b) and Pauluis

(2011). Note that for saturated parcels at equilibrium the Gibbs function for each phase is the same, so that any water transfer between phases cancels out in the integrals and does not contribute to the Gibbs penalty term. This mechanical energy budget is discussed in more detail in Chapter 3 where it is central to much of the analysis.

1.4 CONVECTION SCHEMES IN CLIMATE MODELS

The development of climate models is a complex process involving many inter-related components (Flato et al., 2013). A key element is sub-grid parametrisation, the use of approximations to express physical processes which are not represented explicitly within climate models. The extent of parametrisation required will thus depend on the size of the grid used within the model, and a small scale model such as the Large Eddy Model (LEM) used in this study (a CRM developed by the Met Office which underpins some of the work in Chapter 3 and is described in Section 3.2) does not require parametrisation of convection in contrast to larger scale models such as GCMs. Despite the availability of such models, even relatively high resolution models for climate and global NWP may still need to parametrise cumulus convection, given that the length-scale of this process is often of the order of 100m. Such compromises are not without cost - studies have shown that models that include a combination of high-resolution and explicit representation of convection can generate a great deal of "noise", often requiring a large ensemble approach (Bechtold, 2014).

Bechtold (2014) identifies three steps in convective parametrisation, which in turn determine:

1. the occurrence and localisation of convection ("triggering"),

2. the vertical distribution of heating, moistening and momentum changes (via a cloud model),

3. the amount of precipitation, which corresponds to energy conversion ("closure").

He provides a categorisation of convection schemes into those based on moisture budgets (such as the Kuo scheme), adjustment schemes (such as Betts Miller) and mass flux schemes (which now dominate). These last schemes usually represent the processes linked with up-

ward convection (generally) as a single entraining and detraining plume within each grid cell (see detailed description in Plant, 2010; Yano, 2016). Key assumptions made will include the amount of mixing between the ascending plume and the environment ("entrainment" and "detrainment"), and also the amount of mass-flux convection at some base level, connected to the precipitation and energy conversion, which is referred to as "closure". This last element is commonly assumed to be related to the large-scale circulation to maintain the quasi-equilibrium of some quantity (Yano and Plant, 2016), an approach first suggested by Arakawa and Schubert (1974), who hypothesised a statistical equilibrium between the production of potential energy by the large-scale processes and its destruction through convection. Thus an analysis of the energetic processes involved in convection and their relation to the large-scale can be central to the development of parametrisation schemes.

An alternative approach is that known as "superparametrisation", first suggested in Grabowski and Smolarkiewicz (1999), which consists of using (2 dimensional) cloud system resolving models at each grid cell to represent the convective processes. This appears to provide much better representation of phenomena such as the MJO (Benedict and Randall, 2009), but remains computationally expensive (Randall et al., 2003), a prohibitive factor for many applications.

1.5 THE USE OF SUPRA-DOMAIN PARAMETRISATION IN STUDIES OF CONVECTION

A number of studies which aim to deepen understanding of tropical convection have been carried out using the WTG, or similar, coupling mechanisms, to provide a linkage between studies of a limited area, generally using a CRM, and large-scale dynamics. The most common version of the WTG approach relates vertical velocity in a limited domain model (which may be studied analytically, or using a Single Column Model (SCM) or CRM) to the vertical profile of the mean temperature difference between the domain of the model and an external reference profile. The approach is to solve for the vertical velocity which will balance any heating anomalies by advection.

Sobel and Bretherton (2000) introduced this general approach (albeit in a "strict" version, i.e. with no notion of a finite time over which temperature differences are eliminated). They demonstrate that a disconnected set of single-column models in which the large-scale dynamics are replaced by a balance between the vertical advection and the diabatic heating can provide a realistic representation of many aspects of tropical convection. Sobel et al. (2001) subsequently combined the WTG approximation with a linear moist model to derive analytical expressions which suggest the existence of tropical modes of variability linked to moisture advection.

Raymond and Zeng (2005) introduced a variant of the WTG approximation where in addition to a relaxation timescale for temperature anomalies, the large-scale vertical velocity is modulated by a sinusoidal-term height dependency. They used this to study the effect of varying imposed cross-domain wind speeds or surface temperatures on precipitation, showing a relationship between that quantity and the difference between entropy sources at the surface and radiative entropy sinks in the atmosphere. Raymond (2007) subsequently used this approach to show how a simple cumulus parametrisation could be tuned and identified the sensitivity in the relationship between precipitation and surface wind. Sessions et al. (2010) also used a cloud resolving model linked to a reference atmosphere using this sinusoidal variant of WTG coupling. Their experiments demonstrated possible convergence of the column to one of two equilibria, with either a dry atmosphere with no precipitation, or a moist precipitating state, and generated insights into the factors driving this state selection.

The CRM studies referred to above have used a two-dimensional configuration to limit computational cost. Wang and Sobel (2011) carried out a comparison between 2-dimensional and 3-dimensional models, which gave broadly similar results, albeit the 2-dimensional runs exhibit greater sensitivity to SST contrasts, which they suggest may be due to a lesser entrainment effect in those configurations.

Daleu et al. (2012) used the WTG (without the sinusoidal term) to couple two two-dimensional CRMs and compared this with the reference atmosphere approach used in the studies above.

Subsequently Daleu et al. (2015a) investigated the timescales over which transition from suppressed to active convection occurs. Using such a configuration also permits the development of energy budgets and has inspired the model framework used in Chapter 3 of this thesis.

A number of researchers have sought to validate the use of the WTG approximation in the models discussed above. Sentić et al. (2015) compared WTG simulations of convection based on observations obtained during the DYNAMO campaign and concluded that they reproduce observed precipitation and other diagnostics reasonably well.

Alternative approaches have been used to model the supra-domain parametrisation. The most prominent of these is the WPG approximation, which instead of solving for the vertical advection (and hence velocity) consistent with a temperature difference profile, uses linearised equations of motion and assumes a gravity wave mechanism in order to diagnose the vertical velocity generated by a (virtual) temperature anomaly. This was introduced by Kuang (2008a), who showed that linear convectively coupled gravity waves similar to those identified in Haertel and Kiladis (2004) can develop spontaneously in such a framework. Kuang (2008b) further investigated how instability mechanisms can arise in such a context.

Wang et al. (2013) used both the WTG and WPG approaches to simulate variations in convective activity observed during the TOGA-COARE field campaign. They found that both have some success in simulating rainfall, although the WTG vertical velocity is too top-heavy relative to observations and the converse is true for the WPG based models.

Romps (2012b) compared the WTG and WPG approaches using simplified analytical methods and concluded that they cannot simultaneously replicate timescales for both transient and steady-state behaviour. In addition, he also suggested that WTG coupling may excessively favour deep convection (consistent with Wang et al., 2013), conclusions which were confirmed by numerical simulations in Romps (2012a). Edman and Romps (2014) subsequently proposed a modified version of the WPG approximation which eliminates potential buoyancy resonances in the system.

A systematic international comparison of a number of SCMs and CRMs approaches with identical Sea Surface Temperatures (SSTs) coupled using both the WTG and WPG is described in Daleu et al. (2015b). The study showed, inter alia, that SCMs exhibit a broader range of behaviours than CRMs, and the existence of multiple equilibria under WTG coupling, particularly at higher SSTs. Subsequently Daleu et al. (2016) confirmed the variability of SCMs where the two columns have different SSTs and further suggested that WPG simulations produce vertical velocities which are smoother and less top-heavy than those coupled by the WTG.

The top-heaviness of the WTG approach and the need for interpolation in the boundary layer inspired Herman and Raymond (2014) to suggest using a Fourier decomposition of the potential temperature anomaly profile to provide an expression for large-scale vertical velocity as a sum of the various Fourier modes. Additional approaches include that of Mapes (2004) who included a time lag in the description of the gravity wave. Bergman and Sardeshmukh (2004) instead based the vertical advection on the time history of the diabatic heating, decomposed into Fourier modes.

In this thesis, we concentrate on the energetic consequences of using WTG and (to a lesser extent) WPG coupling methodologies, in particular for the generation of mechanical work. The diagnostic methodologies developed are then applied to re-analysis data in Chapter 4, which permits some novel testing of how well these coupling methodologies represent large-scale circulations.

1.6 THESIS AIMS

This thesis has two broad aims:

- To explore the factors that limit the generation of mechanical energy by overturning circulations in cases where the rotational effects of the earth can be neglected, such as in the tropics or for small-scale convective systems.

- To provide insights into the thermodynamic implications of supra-domain parametrisations such as the WTG, in particular whether they introduce any anomalous energetic behaviour that would undermine their usefulness.

In order to meet these aims, a number of approaches of increasing sophistication are adopted. The generation of mechanical work is first studied for a simple case consisting of two coupled columns in the absence of moisture, using both analytical techniques and a simplified computer model. The insights that this suggests are then tested in a more realistic context, using two coupled CRMs. Finally, the diagnostic approach is applied to re-analysis data.

1.7 Thesis plan

Chapter 2 investigates the energetic implications of the WTG approximation using both analytical techniques and a simplified computer model. The focus is on an idealised system consisting of two dry columns, coupled by the WTG approximation, although extensions to a simple moist case and to the WPG approximation are also studied. Local and global expressions are derived (some approximate, and some dependent on the geometry assumed for the system) for the energy reservoirs and generation of mechanical work by the system. The relationship between the WTG parameter and frictional drag which permits the emergence of quasi-stable systems is also investigated. The chapter concludes with an analysis of the energetics of a dry overturning circulation, including results from the simplified model, identifying the processes which determine the mechanical work done, and relating this to the Guoy-Stodola Equation. Chapter 3 extends the diagnostic technique for partitioning the components of a mechanical energy budget introduced in Pauluis (2016) to a system consisting of two regions coupled by an overturning circulation. This analysis is then applied to the results produced by two coupled CRM models, representing a warm and cool region, coupled by a large-scale parametrisation, principally the WTG approximation. Scaling arguments are developed for the results obtained. Chapter 4 then explores how these techniques can be applied to re-analysis data. The focus here is on the tropical Pacific during the Year of Tropical Convection (YoTC), and notional Walker and Hadley circulations are identified and the work that they generate estimated. Conclusions are drawn and implications discussed in Chapter 5.

The simplified model described in Chapter 2 was also used to investigate the MEP conjecture.

This work is included in an appendix.

CHAPTER 2

A SINGLE COLUMN MODEL PERSPECTIVE ON THE ENERGETICS OF TWO COUPLED COLUMNS

2.1 INTRODUCTION

Our broad objective in this thesis is to deepen understanding of the manner in which temperature anomalies give rise to overturning circulations in the tropics, and the generation of mechanical work that this implies. This will depend on energy and entropy constraints as well as on the form in which the coupling that gives rise to the circulation is implemented. In order to identify the fundamental drivers of these processes, we start with a very simplified model: in this chapter we explore the energetic implications of a coupling parametrisation such as the Weak Temperature Gradient approximation in an idealised context, using both simplified single column models and analytical techniques, focussing on dry convective processes.

Romps (2012b) has investigated analytical solutions for both the Weak Temperature Gradient and Weak Pressure Gradient approximations. The work in this chapter builds on that, developing his equations to include energetic quantities.

As mentioned in section 1.5, we are applying the large-scale parametrisation to generate a large-scale vertical velocity. This is determined by the difference in temperature profile between two regions, and in a coupled system such as that presented here conservation of mass implies that the upward mass flux in one region will be matched by the downward mass flux

in the other. In this chapter each of the two regions are represented by a single column model, and the SST in each column is varied to generate a temperature contrast between the columns.

We first present the main features of the single column model that we have developed and explore some simple applications. We then introduce the Weak Temperature Gradient approximation as a parametrisation of the large scale circulation and show how this generates an overturning circulation between the two columns. We next develop a conceptual model of the energetic pathways within a two column WTG-coupled system and derive analytical expressions for key quantities such as the work generated. These are tested against the model, for the time being running it in a dry mode, i.e. excluding the impact of latent heating. This simple framework allows us to deduce the size of stable convective systems as a function of the characteristic timescales of the processes generating and destroying kinetic energy. We also explore the differences between the Weak Pressure Gradient and Weak Temperature Gradient approximations, and the effect of including moisture.

2.2 DESCRIPTION OF SIMPLIFIED SINGLE COLUMN MODEL

In order to explore the energetic implications of using coupling mechanisms such as the Weak Temperature Gradient (WTG), a simple two-column model was developed in FORTRAN based on a single-column radiative-convective model previously developed by Prof. Ambaum. The model assumes a fixed number (n_l) of layers of equal depth in pressure coordinates, from p_{SURF} (surface pressure, generally taken here as 1000 hPa) at the surface to 0 hPa at the top of the atmosphere. For most of the analyses, two columns of relative width $(1 - \epsilon)$ and ϵ are considered - the model itself just considers two vertical columns and does not require any particular horizontal two-dimensional structure although the assumed geometry has implications for the diagnosed horizontal winds. By convention "Column 2", which is usually the smaller column ($\epsilon \leq 0.5$), is the ascending warmer column and "Column 1" the descending cooler column. The physical meaning of ϵ varies according to the context in this thesis. For a small-scale two-column system it can be regarded as the size of a convecting plume relative to its environment, and can be compared to the convective area fraction - a feature than can be observed in field
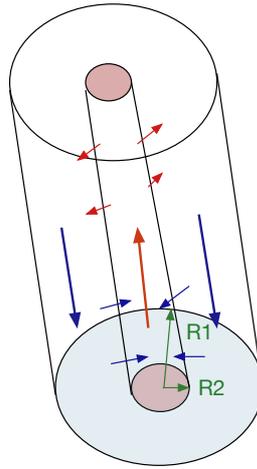
Figure 2.1: *A representation of the two-column framework with cylindrical horizontal geometry. Note that $\epsilon = R_2^2/R_1^2$.*

work (see for example Dorrestijn et al., 2015) where it generally has a value of the order of a few percent. However, in the subsequent chapters (where instead of two columns we examine two coupled CRMs or regions of the tropical Pacific) ϵ represents the relative size of an area dominated by convective ascent (even if it includes both ascending plumes and downward subsidence), as opposed to an area in which convection is suppressed. This will typically have much higher values, depending on the feature studied. As one of the aims in this chapter is to establish a theoretical foundation for the results obtained from the experiments or observational data in subsequent chapters, many of the numerical results in this chapter will be based on a value of $\epsilon = 0.5$. In addition, we attribute a physical significance to ϵ in section 2.7 where it represents the relative size of the active area of a stable convecting system.

In order to facilitate calculation of Available Potential Energy (APE), for reasons discussed in section 2.3, n_l is generally taken as 100, larger than would perhaps be otherwise used. A graphical representation of this set-up, showing a two-dimensional cylindrical geometry, is shown in Figure 2.1.

The model is initialised with temperature profiles for the two columns, consistent with the assumed surface temperatures and radiative-convective equilibrium. The radiative fluxes associated with Short Wave (SW) and Long Wave (LW) radiation are absorbed and emitted in the

two columns, in line with the radiative model described below. The coupling mechanism between the two columns, initially the WTG, advects heat (and moisture where relevant) across the system.

Hydrostatic balance is assumed, as is conservation of mass. The model is run through to equilibrium using a time-step dependent on key parameters, such as the WTG timescale, consistent with the CFL stability of the system. Any heat imbalance due to radiative forcing is balanced by vertical and horizontal heat transport, representing the coupling approach. To avoid introducing excessive complexity, no heat transport by turbulence in the boundary layer has been included.

A simple "gray" radiative transfer model is used, distinguishing SW and LW radiation. Incoming constant solar radiation of $S_0 = 1364$ W m^{-2}, (i.e. no diurnal cycle) is assumed as is a top of atmosphere (TOA) albedo of $\alpha = 0.3$, surface albedo being taken as 0. The atmosphere is assumed to have a SW optical depth $\tau_{SW} = 0.4$ and a LW optical depth of τ_{LW}, which is generally taken as 3, although some alternative values are used at times. The absorptivity and emissivity δ for each layer i of the atmosphere is assumed to vary in line with a simple linear pressure broadening model, implying as per Equation 9.44 in Ambaum (2010):

$$\delta_{LW,i} = \frac{2 p_i \Delta p \, \tau_{LW}}{p_{\mathrm{SURF}}^2}, \quad \delta_{SW,i} = \frac{2 p_i \Delta p \, \tau_{SW}}{p_{\mathrm{SURF}}^2} \quad, \tag{2.1}$$

with p_i the layer central pressure, Δ_p the depth of each layer and p_{SURF} the pressure at the surface. Radiative transfer equations give heat fluxes between each layer, evaluated at the top

of layer i thus:

$$L_{\downarrow,LW,nl} = 0 \quad , \tag{2.2}$$

$$L_{\downarrow,LW,i} = (1 - \delta_{LW,i})L_{\downarrow,LW,i+1} + \delta_{LW,i}\sigma T_i^4 \quad , \tag{2.3}$$

$$L_{\uparrow,LW,0} = \sigma T_s^4 \quad , \tag{2.4}$$

$$L_{\uparrow,LW,i} = (1 - \delta_{LW,i})L_{\uparrow,LW,i-1} + \delta_{LW,i}\sigma T_i^4 \quad , \tag{2.5}$$

$$L_{\downarrow,SW,nl+1} = (1 - \alpha)S_0/4 \quad , \tag{2.6}$$

$$L_{\downarrow,SW,i} = (1 - \delta_{SW,i})L_{\downarrow,SW,i+1} \quad , \tag{2.7}$$

$$L_{\uparrow,SW,i} = 0 \quad . \tag{2.8}$$

L represents the (upward/downward, LW/SW) radiation flux for layer i, σ is the Stefan-Boltzman constant and T_i is the temperature of layer i. The model uses the selected coupling parametrisation to determine vertical velocity in each column. The two coupling methodologies examined in the model are the WTG and the WPG which are described in sections 2.5 and 2.12 respectively. Horizontal mass fluxes are determined by the vertical velocity through conservation of mass. The quantity advected in the model is (specific, dry) entropy ($s = c_p \log\theta/T_0$), which is conserved by adiabatic processes.

Although the model was mainly used in a dry configuration, in order to introduce convective heating a simplified approach to modelling moisture has been included in section 2.11. A fixed profile of 100% relative humidity above the boundary layer is assumed for the ascending column - inspired by the discussion in Betts and Miller (1993) of observational evidence which suggests that convecting areas in the tropics maintain a vertical thermal structure that is similar to a moist adiabat. An additional convective heating term $L_v w \partial r_v/\partial z$ is then included, where L_v is the specific evaporation enthalpy of water and w is the vertical wind speed. Any moisture that condenses can be regarded as then precipitating out. This heating term is regarded as an energy input and the model does not track the conservation of moisture or the energy inputs necessary to maintain the humidity profile. The variable used to determine the WTG velocity remains θ, rather than θ_v. The saturated vapour pressure which determines condensation is

obtained from Bolton's version of Teten's formula (Bolton, 1980):

$$e_s(\text{hPa}) = 6.112 \exp\left(\frac{17.67\,T(°\text{C})}{T(°\text{C}) + 234.5} \right) \quad . \tag{2.9}$$

In order to avoid possible instabilities, a flux limiter was introduced to ensure that the temperature in Column 1 never exceeds that in Column 2, and the temperatures in the two columns at the top of the atmosphere were set equal to each other. Apart from verifying that the results are stable (e.g. for different time-steps or for longer runs), the model can also be validated by comparing the balance of radiative energy absorbed and emitted on the one hand with the mechanical work generated. Discrepancies of the order of 5% of the value of this quantity are found; the source of these appears to lie in the fact that the advected entropy is a very small proportion of the entropy in each layer, and truncation errors arise, despite the use of extended precision. Since the radiative energy emitted is a quartic function of temperature, such errors are amplified. The problem appears to be exacerbated in the WTG case by the discontinuity at the boundary layer, which enables computational modes to become evident in the form of trapped waves below the boundary layer and certain results will show this discrepancy. Given that the energy converted is a relatively small proportion of the energy input, this discrepancy was judged to be acceptable.

2.3   AVAILABLE POTENTIAL ENERGY FOR A TWO-COLUMN SYSTEM

APE, which has been introduced in section 1.2, is closely tied to other energetic quantities in the simplified system that is studied in this chapter and is central to much of this work. APE can be defined as that part of the potential energy of the system that is available for conversion to kinetic energy by an adiabatic re-distribution of mass that would result in a minimum potential energy configuration. This suggests that in an atmospheric model consisting of a single column with n_l discrete layers it should be possible to calculate APE by sorting the layers into a state where potential temperature θ increases with height and calculating the difference in total potential energy liberated by this sorting. This approach can be generalised to a model with n_c multiple columns by combining these into a single sorted column consisting of $n_l \times n_c$ layers. Model results indicate that the value of this "sorted APE" may decrease markedly with

increased resolution (i.e. number of horizontal layers) until a stable limit is reached, particularly if the component of APE above the boundary layer is considered separately. This suggests that for low resolution a sorting approach may overstate the value of APE, as explained below.

As pointed out in Lorenz (1955) the total potential (and internal) energy of a column of air is given by $c_p/g \int T \, dp$, where g is the acceleration due to gravity at the Earth's surface. Consider two columns, each of relative area $1 - \epsilon$ and $\epsilon = 0.5$ with potential temperature $\theta_2 = \theta_1 + \Delta\theta$. Suppose also that the model consists of n_l layers of depth Δp and that $\partial\theta/\partial p \Delta p > \Delta\theta$, i.e. the (potential) temperature difference between the columns is small relative to the stability. The potential energy P of the system can be expressed as:

$$P = \frac{c_p}{g p_0^\kappa} \sum_{i=1}^{n_l} \Delta p \left((1-\epsilon)\theta_{1,i}(p_i^\kappa) + \epsilon\theta_{2,i}(p_i^\kappa) \right) \quad , \tag{2.10}$$

where $\kappa = R_d/c_p$ and $\theta = T(p_0/p)^\kappa$, p_0 being a reference pressure used to convert between temperature and potential temperature. If one adiabatically re-orders this atmosphere into a sorted single column with $2n_l$ layers of depth $\Delta p/2$ that would suggest that the change in potential energy liberated by this transformation, i.e. the APE ($\bar{A}$) is given by:

$$\bar{A} = \frac{c_p}{g p_0^\kappa} \sum_{i=1}^{n_l} \Delta p \left((1-\epsilon)\theta_{1,i}\left(p_i^\kappa - \left(p_i + \frac{\Delta p}{2} \right)^\kappa \right) + \epsilon\theta_{2,i}\left(p_i^\kappa - \left(p_i - \frac{\Delta p}{2} \right)^\kappa \right) \right) \tag{2.11}$$

$$\approx \frac{R_d}{2 g p_0^\kappa} \sum_{i=1}^{n_l} (\Delta p)^2 p_i^{\kappa-1} \left(\epsilon\theta_{2,i} - (1-\epsilon)\theta_{1,i} \right) \quad . \tag{2.12}$$

It will be seen that this expression has a quadratic dependence on Δp, and thus for two column models where the temperature difference difference between the two columns is slight and APE is calculated by sorting, it is important to choose a model with a sufficient number of layers. This difference between "sorted" APE as described above, and "true" APE, which is independent of this discretisation effect is illustrated for an idealised study discussed below in Figure 2.2.

Lorenz derives a number of approximate expressions for APE, one of which (equation 8 in Lorenz (1955)) is particularly suited to multi-column models with isobaric levels:
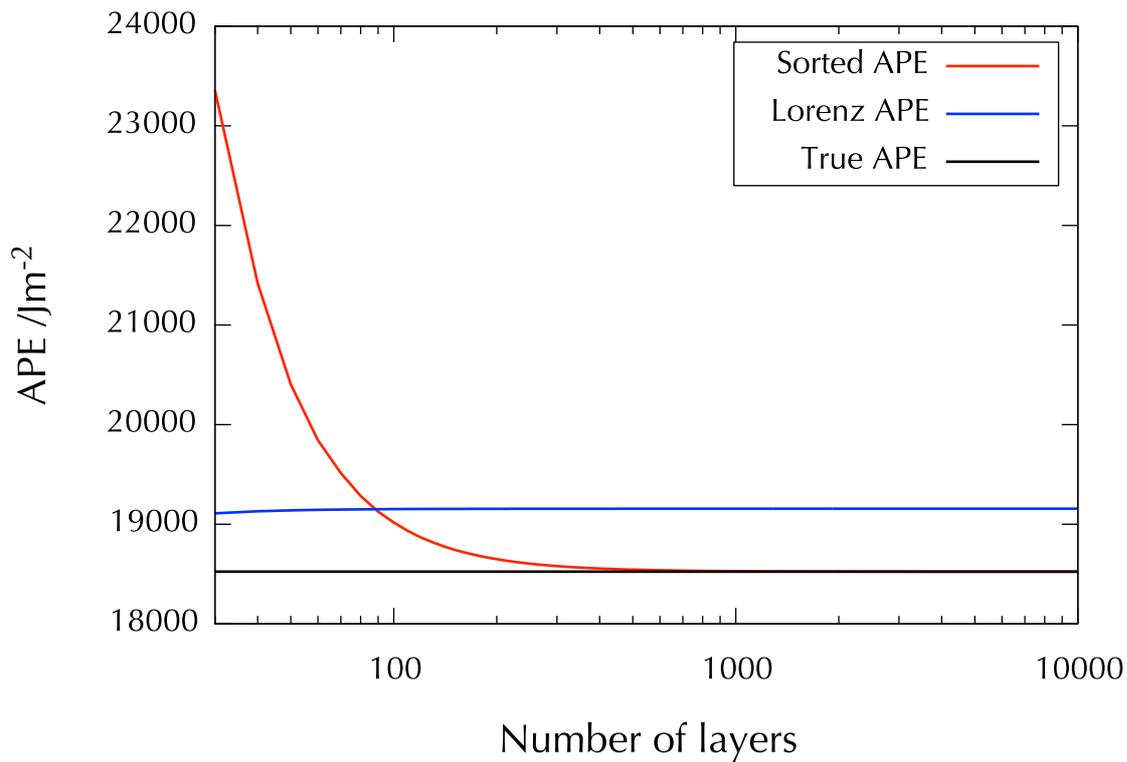
Figure 2.2: *Comparison of "sorted" APE and that calculated using Equation 2.13 ("Lorenz") with "true" APE (the sorted value as the depth of each layer tends to zero) for an idealised study consisting of two columns of equal size, with a temperature difference of 1K between the columns.*

$$\bar{A} = \frac{\kappa c_p}{2g \, p_0^{\kappa}} \int_0^{p_{\text{SURF}}} \bar{\theta}^2 \, \bar{p}^{-(1-\kappa)} \left(-\frac{\partial \bar{\theta}}{\partial p} \right)^{-1} \left(\frac{\theta'}{\bar{\theta}} \right)^2 \mathrm{d}p \quad , \tag{2.13}$$

where p_{SURF} is the pressure at the Earth's surface and θ' is the potential temperature anomaly at a given height. Model results indicate that the use of this expression generally overstates the value of APE when compared with "true APE"; the reason for this is that the formula can be regarded as transposing a potential temperature anomaly by a distance $\theta' / \frac{\partial \bar{\theta}}{\partial p}$ in pressure coordinates. For much of the atmosphere this is a reasonable approximation, but at the very top and bottom of the atmosphere it is clearly unrealistic.

This can be highlighted by using a simple linear model with surface temperature T_0 and a potential temperature profile varying linearly with pressure with gradient α, so $\theta_1 = T_1 + \alpha(p_{\text{SURF}} -$

p) and $\theta_2 = \theta_1 + \Delta$ and also taking $p_0 = p_{\text{SURF}}$. Consequently $\theta_{\text{ref}} = \bar{\theta} = \theta_1 + \Delta/2$, and the state corresponding to the minimum potential energy has a potential temperature profile given by:

$$\theta_{\min} = T_1 + 2\alpha(p_{\text{SURF}} - p) \qquad\qquad \text{for } p \geq p_{\text{SURF}} - p_\Delta \qquad (2.14)$$

$$= \theta_{\text{ref}} \qquad\qquad \text{for } p_{\text{SURF}} - p_\Delta \geq p \geq p_\Delta \qquad (2.15)$$

$$= T_1 + \Delta/2 + \alpha(p_{\text{SURF}} + p_\Delta - 2p) \qquad\qquad \text{for } p \leq p_\Delta \quad , \qquad (2.16)$$

where $p_\Delta = \Delta/2\alpha$. An exact expression for the available potential energy can be obtained as follows:

$$\bar{A}_{\text{exact}} = \frac{c_p}{g p_{\text{SURF}}^\kappa} \int_0^{p_{\text{SURF}}} (\theta_{\text{ref}} - \theta_{\min}) p^\kappa \, dp \qquad (2.17)$$

$$= \frac{c_p}{g p_{\text{SURF}}^\kappa} \left[\int_0^{p_\Delta} \alpha(p - p_\Delta) p^\kappa \, dp + \int_{(p_{\text{SURF}} - p_\Delta)}^{p_{\text{SURF}}} (\frac{\Delta}{2} - \alpha p_{\text{SURF}} + \alpha p) p^\kappa \, dp \right] \qquad (2.18)$$

$$= \frac{c_p}{g p_{\text{SURF}}^\kappa (\kappa + 1)(\kappa + 2)} \left[(\kappa + 2)(\Delta/2 - \alpha p_{\text{SURF}})(p_{\text{ref}}^{\kappa+1} - (p_{\text{SURF}} - p_\Delta)^{\kappa+1}) \right.$$

$$\left. + \alpha(\kappa + 1)(p_{\text{SURF}}^{\kappa+2} - (p_{\text{SURF}} - p_\Delta)^{\kappa+2}) - \alpha p_\Delta^{\kappa+2} \right] \quad . \qquad (2.19)$$

This exact expression can be approximated by a Taylor expansion in which we keep terms up to order $p_\Delta^{\kappa+2}$:

$$\bar{A}_{\text{exact}} \approx \frac{c_p}{g p_{\text{SURF}}^\kappa (\kappa + 1)(\kappa + 2)} \left[(\kappa + 2)(\Delta/2 - \alpha p_{\text{SURF}})((\kappa + 1) p_\Delta p_{\text{SURF}}^\kappa - 1/2(\kappa + 1)\kappa p_\Delta^2 p_{\text{SURF}}^{(\kappa-1)}) \right)$$

$$+ \alpha(\kappa + 1)((\kappa + 2) p_{\text{SURF}}^{\kappa+1} p_\Delta - 1/2(\kappa + 2)(\kappa + 1) p_{\text{SURF}}^\kappa p_\Delta^2) - \alpha p_\Delta^{\kappa+2} \right] \qquad (2.20)$$

$$\approx \frac{c_p}{g p_{\text{SURF}}^\kappa} \left[(\Delta/2 - \alpha p_{\text{SURF}}) p_\Delta p_{\text{SURF}}^\kappa + 1/2\alpha\kappa p_\Delta^2 p_{\text{SURF}}^\kappa \right.$$

$$\left. + \alpha(p_{\text{SURF}}^{\kappa+1} p_\Delta - 1/2(\kappa + 1) p_{\text{SURF}}^\kappa p_\Delta^2) - \frac{\alpha}{(\kappa + 1)(\kappa + 2)} p_\Delta^{\kappa+2} \right] \qquad (2.21)$$

$$\approx \frac{c_p \Delta^2}{8 g \alpha} \left[1 - \frac{2}{(\kappa + 1)(\kappa + 2)} \left(p_\Delta / p_{\text{SURF}} \right)^\kappa \right] \quad . \qquad (2.22)$$

We can also obtain an exact expression for the Lorenz APE for this example:

$$\bar{A}_{\text{Lorenz}} = \frac{\kappa c_p}{2g p_{\text{SURF}}^{\kappa}} \int_0^{p_{\text{SURF}}} \frac{p^{\kappa-1}\Delta^2}{4\alpha} \mathrm{d}p \tag{2.23}$$

$$= \frac{c_p \Delta^2}{8g\alpha} \quad . \tag{2.24}$$

It will be seen that this expression omits the second term in Equation 2.22. This suggests that the Lorenz approximation will in general overstate the true value of APE by a factor of the order of $(p_\Delta/p_{\text{SURF}})^\kappa$ where p_Δ is related to the temperature difference between the two columns and the stability of the average atmosphere.

To illustrate this and the sorting effect discussed above the various estimates of APE described above were calculated for a different number of layers in a simplified model, where the two equally sized columns have a temperature profile that on average is that of the US Standard Atmosphere (1976), but with a 1 K difference between the two columns (Figure 2.2) throughout the atmosphere. Although this linear model is somewhat unrealistic, similar effects have been at times observed in the results produced by the simplified coupled SCM used in this chapter.

2.4 ENTROPY GENERATION AND SYSTEM BOUNDARIES

The calculation of the generation of entropy is dependent on the definition of the system under consideration. To illustrate this consider the radiative equilibrium state which emerges from the model described above run in a single column configuration from two distinct perspectives, namely:

1. that of the system as a whole, as viewed from outside (where the focus is on the layer by which external radiation, both incoming SW and LW radiated by the surface, is first absorbed by the system, and on the layer by which any radiation emitted by the system both out to the space and down to the surface has been emitted) - these fluxes are represented by $\mathscr{F}_{\text{in}}$ and $\mathscr{F}_{\text{out}}$;

2. where the focus is on the absorption and emission of radiation (incoming SW and LW radiated by the surface) by each layer irrespective of the most recent source and next destination of that radiation - these fluxes are represented by F_{in} and F_{out}.

Clearly, at equilibrium each layer is in energetic balance, in other words the radiation absorbed $F_{\text{in}}(p) = F_{\text{out}}(p)$, the radiation emitted. However, when we consider the net absorption of external radiation $\mathscr{F}_{\text{in}}(p)$ and the contribution to the net emission of radiation by the entire system $\mathscr{F}_{\text{out}}(p)$ this is not the case, as the re-emission and subsequent absorption of radiation means that net emission occurs at a higher level than net absorption. Values for these fluxes produced by the model for the base case are shown in Figure 2.3.

(a) *Viewed from within each layer* (b) *Viewed from outside the system*
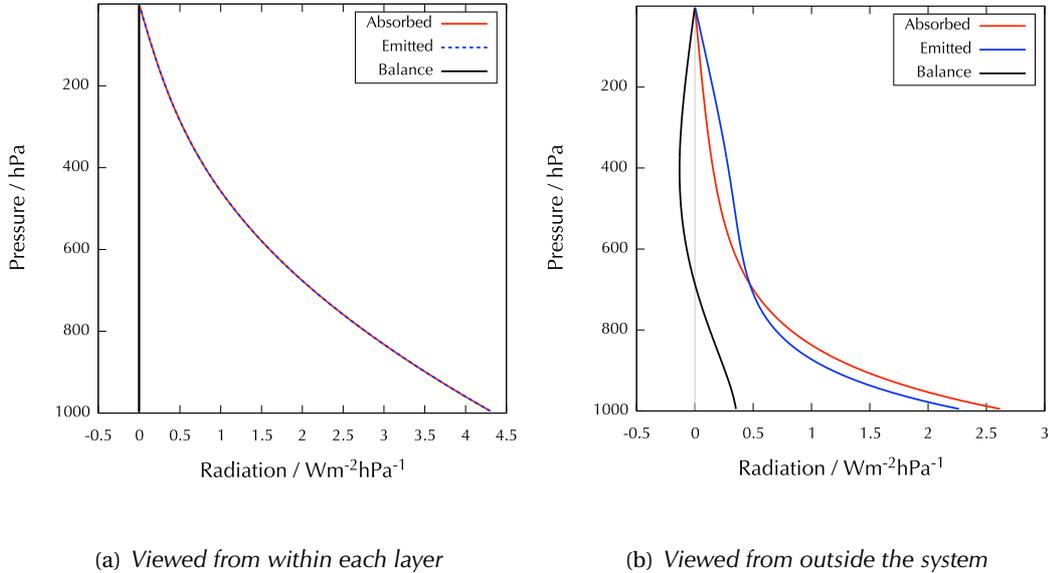
Figure 2.3: *Absorbed and emitted radiative flux by height for simplified mode at RCE with SST 295 K, $\epsilon = 0.5$ and $\delta_{\text{LW}} = 3$.*

The weighted temperature for both absorption and emission from the layer by layer perspective is 261.5 K, for the system perspective the absorption temperature is 267.5 K and the emission is 261.8 K - the entropy produced by this re-radiation is 39.2 mJ K^{-1} m^{-2}, whereas the layer-by-layer perspective does not involve any entropy production. This is because in this case it is the transport of energy between the different layers that gives rise to the entropy production, and this is not captured in the layer by layer perspective - the definition of entropy based on local entropy budgets is problematic. This underlines the need for clarity and con-

sistency when entropic processes are considered in a system.

In Chapters 3 and 4 we make use of Pauluis' diagnostic methodology (as expressed in Equation 1.8). This only considers processes that are linked to the heating or cooling of parcels of moist air or its vertical motion - for example the energy input or output is merely the entropy change of a parcel as it completes a closed trajectory in entropy - temperature space. From the perspective of the parcel, this net energy input is reversible and it does not directly include the effect of radiation absorbed and emitted by the atmosphere in any of the terms; this is not just a consequence of the fixed cooling rate used as a radiative model but due simply to the system boundaries implicit in the choice of methodology- under this methodology the system boundaries include temperature and phase changes in the parcels as they complete their averaged trajectories, but exclude other aspects of the absorption and radiation of heat. It should be remembered that a different methodological approach could include other processes that produce entropy and thus imply different efficiencies.

2.5   The Weak Temperature Gradient Approximation

A form of the WTG was initially suggested in Sobel and Bretherton (2000) as a prescription for vertical velocity in pressure coordinates ω. Starting from the primitive thermal energy equation in pressure coordinates:

$$\frac{\partial T}{\partial t} + \mathbf{u}_h . \nabla_h T + \frac{T\omega}{\theta}\frac{\partial \theta}{\partial p} = \frac{Q_{\text{source}}}{c_p} \quad , \tag{2.25}$$

where $\mathbf{u} = (u, v, w)$ is the wind velocity vector, $\mathbf{u}_h = (u, v, 0)$ is its horizontal component, and Q_{source} is a heating term. Assuming a steady state, and neglecting horizontal advection (which can be justified in the tropics since temperature gradients are observed to be small), this provides a diagnostic equation for ω:

$$\omega = \frac{Q_{\text{source}}\theta}{Tc_p \partial\theta/\partial p} \quad . \tag{2.26}$$

Sobel and Bretherton further suggested that vertical mixing in the Planetary Boundary Layer (PBL) can be represented by interpolating ω from its value at the top of the boundary layer to 0 at the surface. This ω has been referred to as the "WTG vertical velocity".

Inspired by this approach, Raymond and Zeng (2005) considered splitting the wind velocity into a component that is explicitly represented in CRMs and a further component representing the large-scale motion not captured by such models. The large scale circulation serves to relax the horizontally averaged potential temperature $\bar{\theta}$ to a reference profile θ_{ref} over a timescale τ_{WTG} ($=\lambda_{\text{T}}^{-1}$ in their notation), taken to be 2 hours. In order to allow for the fact that the adjustment process by gravity waves is expected to be most rapid in the middle troposphere, a factor of $\sin(\pi z/H_{\text{Trop}})$ is introduced, where H_{Trop} is the height of the troposphere. This approach gives the following expression for ω above the boundary layer:

$$\omega = \frac{(\bar{\theta} - \theta_{\text{ref}})}{\tau_{\text{WTG}} \partial\theta/\partial p} \sin(\pi z/H_{\text{Trop}}) \quad . \tag{2.27}$$

The boundary layer interpolation is retained, and in order to avoid weak vertical stability in the upper atmosphere giving rise to high vertical velocities, $\partial\theta/\partial z$ is limited to values above 1 K km^{-1}. It is common to simplify this expression by neglecting the sine dependence on height, giving the versions of the WTG velocity above the boundary layer that are mostly used in this work:

$$\omega = \frac{(\bar{\theta} - \theta_{\text{ref}})}{\tau_{\text{WTG}} \partial\theta/\partial p} \quad \text{in pressure coordinates, or} \tag{2.28}$$

$$w = \frac{(\bar{\theta} - \theta_{\text{ref}})}{\tau_{\text{WTG}} \partial\theta/\partial z} \quad \text{in height coordinates.} \tag{2.29}$$

These simplified expressions will be used to produce analytical expressions for various energetic quantities in the subsequent sections of this chapter. The coupled column model uses Equation 2.28, using a weighted mean of θ_1, θ_2 for $\theta_{\text{ref}} = (1-\epsilon)\theta_1 + \epsilon\theta_2$, to calculate ω above the boundary layer (taken as the model pressure level nearest to 850 hPa). The stability term in the denominator is calculated as $\partial\theta_{\text{ref}}/\partial p$ for consistency between the two columns. ω within the boundary layer is obtained by interpolation in pressure coordinates between ω_{BL} the value at the top of the boundary layer and 0 at the surface. The vertical velocity in height coordinates

w is derived from ω using $\omega = -\rho g w$. The vertical velocities are used to calculate vertical mass flux within the two columns, and the horizontal mass flux (between the columns) is determined by conservation of mass.

As the model was being tested it was discovered that if the vertical advection in Column i is calculated by $\omega_i \frac{\partial \theta_{\mathrm{ref}}}{\partial p}$ rather than using the potential temperature profiles within each column $\omega_i \frac{\partial \theta_i}{\partial p}$ this resulted in the heating due to advection in Column 1 being perfectly matched by the cooling in Column 2, and no explicit conversion from APE to kinetic energy, although a WTG velocity was generated. The final version of the model corrected this, by using the actual potential temperature (to be precise, entropy) profile in each column for the vertical advection.

Before embarking further, it is helpful to examine some of the final state results produced by this model. For the control case, the columns are assumed to be of equal size ($\epsilon = 0.5$) and the WTG timescale relaxation parameter τ_{WTG} is taken as 3 hours, a typical parameter value used in other studies (Daleu et al., 2015b). The SSTs in the two columns are, unless otherwise stated, taken as 298 K and 300 K respectively, i.e. a difference $\Delta T_s = 2$ K. Profiles of the potential temperatures in the two columns and the velocities generated are shown in Figure 2.4.

(a) θ (b) *LS velocity*
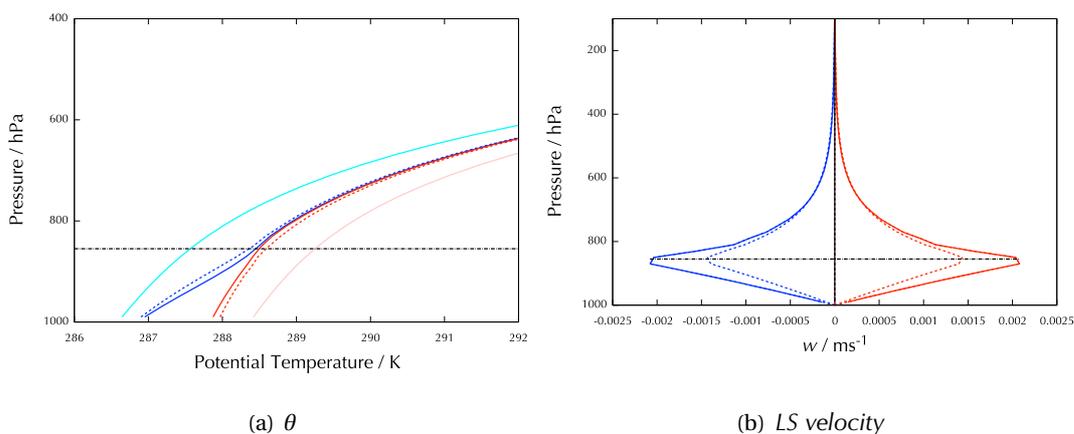
Figure 2.4: *Comparison of equilibrium states for τ = 3 hours (solid), τ = 24 hours (dashed) and uncoupled runs (pale colours). $\epsilon = 0.5$ and the SSTs in the two columns are 298K and 300K. The cool column is shown in blue/cyan and the warm column in red/pink.*

The effect of the coupling is to advect air between the two columns, reducing the potential temperature difference between them, particularly above the boundary layer. In the boundary layer the vertical wind is interpolated to zero at the surface, and consequently the effect of the coupling on the potential temperatures weakens. The vertical wind reduces with height above the PBL (note that there is no latent heating at this stage) as the temperature contrast between the two columns decreases and the stability increases.

2.6 Energy conversions and reservoirs under Weak Temperature Gradient coupling

Following Romps (2012b) one can express the primitive equations for a 2 dimensional system in linearised Boussinesq form in height coordinates as follows:

$$\frac{\partial u}{\partial t} = -\frac{1}{\bar{\rho}}\frac{\partial p'}{\partial x} - \frac{u}{\tau_{\mathrm{Ray}}} \quad , \tag{2.30}$$

$$\frac{\partial w}{\partial t} = -\frac{1}{\bar{\rho}}\frac{\partial p'}{\partial z} + B \quad , \tag{2.31}$$

$$\frac{\partial B}{\partial t} = -N^2 w + Q \quad , \tag{2.32}$$

$$\frac{\partial u}{\partial x} + \frac{\partial w}{\partial z} = 0 \quad , \tag{2.33}$$

where $B = \frac{g\theta'}{\bar{\theta}}$ is the buoyancy, p' is a pressure perturbation, τ_{Ray} represents friction through Rayleigh damping and N is the Brunt-Väisälä frequency $\left(N^2 = \frac{g}{\bar{\theta}}\frac{\partial\bar{\theta}}{\partial z}\right)$. We consider a system in which the vertical velocity is set by the WTG approximation (above the boundary layer) thus:

$$w = \frac{\theta'}{\tau_{\mathrm{WTG}}\partial\bar{\theta}/\partial z} = \frac{B}{\tau_{\mathrm{WTG}}N^2} \quad . \tag{2.34}$$

The Available Potential Energy (APE) is that part of the potential energy of the system that is available for conversion to kinetic energy by an adiabatic re-distribution of mass that would result in a minimum potential energy configuration (see Section 2.3 for a fuller discussion). The Lorenz APE $\bar{A}$ of the system can be described locally by "availability" $A = \frac{B^2}{2N^2}$. This can be

verified by considering the column integral of A:

$$\int_0^\infty \rho A \mathrm{d}z = \frac{1}{2} \int_0^\infty \frac{\rho B^2}{N^2} \mathrm{d}z = \frac{1}{2} \int_0^{p_{\text{SURF}}} \frac{\theta'^2}{\bar{\theta}(\partial\bar{\theta}/\partial z)} \mathrm{d}p = \frac{1}{2g} \int_0^{p_{\text{SURF}}} \frac{\theta'^2}{\rho\bar{\theta}(-\partial\bar{\theta}/\partial p)} \mathrm{d}p \tag{2.35}$$

$$= \frac{R}{2gp_0^\kappa} \int_0^{p_{\text{SURF}}} \frac{p^{\kappa-1}\theta'^2}{(-\partial\bar{\theta}/\partial p)} \mathrm{d}p = \bar{A} \quad \text{(see Eq 2.13).} \tag{2.36}$$

The time derivative of this availability (for N constant with respect to time) is given by:

$$\frac{\partial A}{\partial t} = \frac{2B}{2N^2} \frac{\partial B}{\partial t} = \frac{BQ}{N^2} - Bw = \frac{BQ}{N^2} - \frac{2A}{\tau_{\text{WTG}}} \quad . \tag{2.37}$$

This can be interpreted as indicating that availability is increased by a heating term $\frac{BQ}{N^2}$ (note that net heating is input at higher temperatures for this to be positive, as thermodynamic theory requires if work is to be generated) being balanced by a conversion term from APE to kinetic energy of:

$$C_{A\rightarrow K} = \frac{2\bar{A}}{\tau_{\text{WTG}}} \quad . \tag{2.38}$$

This result, Equation 2.38, which needs to be modified for layers in the boundary layer by increasing the effective timescale, provides a simple relationship between the APE and the work generated by a WTG-coupled system.

Vertical kinetic energy (per unit mass) can be expressed as $K_v = 1/2w^2$. The time derivative of this is given by:

$$\frac{\partial K_v}{\partial t} = w\frac{\partial w}{\partial t} = -\frac{1}{\bar{\rho}} w\frac{\partial p'}{\partial z} + Bw = -\frac{1}{\bar{\rho}} \frac{\partial(wp')}{\partial z} + \frac{1}{\bar{\rho}} p'\frac{\partial w}{\partial z} + Bw \quad . \tag{2.39}$$

The same conversion term $C_{A\rightarrow K} = Bw$ appears in Equation 2.37 and there are also two terms involving vertical velocity and the perturbed pressure field. Likewise for horizontal kinetic energy (using a two-dimensional approach for simplicity):

$$\frac{\partial K_h}{\partial t} = u\frac{\partial u}{\partial t} = -\frac{1}{\bar{\rho}}u\frac{\partial p'}{\partial x} - \frac{u^2}{\tau_{\text{Ray}}} = -\frac{1}{\bar{\rho}}\frac{\partial(up')}{\partial x} + \frac{1}{\bar{\rho}}p'\frac{\partial u}{\partial x} - 2\frac{K_h}{\tau_{\text{Ray}}} \quad . \tag{2.40}$$

Since $\frac{\partial u}{\partial x} = -\frac{\partial w}{\partial z}$ we can identify a conversion term between vertical and horizontal kinetic energy $C_{KE_v \to KE_h} = -\frac{p'}{\bar{\rho}}\frac{\partial w}{\partial z} = \frac{p'}{\bar{\rho}}\frac{\partial u}{\partial x}$, as well as the destruction of kinetic energy due to friction in the last term. There is also an energy sink of $1/\bar{\rho}\nabla.(\mathbf{u}p')$, the horizontal and vertical components of which appear in the horizontal and vertical equations respectively. This term represents work of flow against internal pressure anomalies. Over the entire system we can write:

$$\int \nabla.(\mathbf{u}p')dV = \int p'\mathbf{u}.\mathbf{dS} \quad , \tag{2.41}$$

where V is the volume of the system and $\mathbf{S}$ is the surface vector. For a closed system this will be zero, so does not represent any energy input into the system. This system can be described schematically as shown in Figure 2.5:
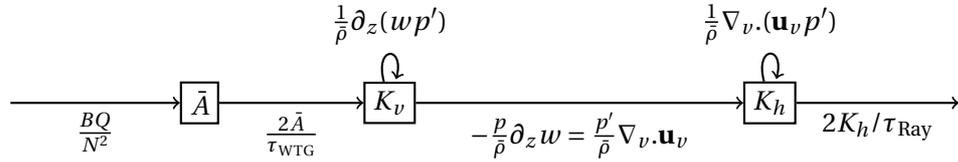
Figure 2.5: *Schematic representation of energy pathways in WTG-coupled SCM (above PBL).*

We now consider relationships between the energy reservoirs $\bar{A}, K_v, K_h$ rather than the conver-
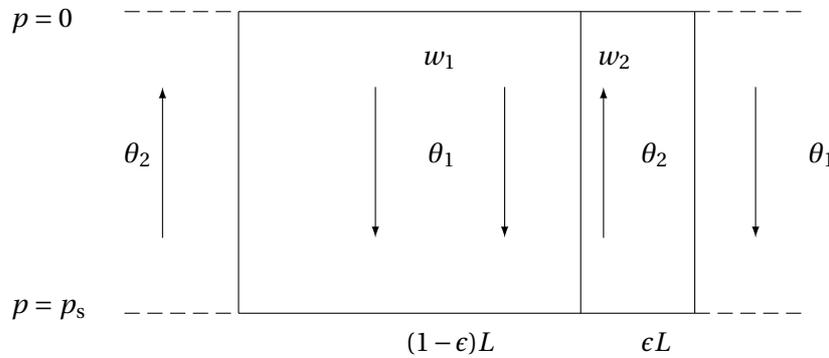
Figure 2.6: *Model structure*

sion terms. Particularly in as far as the horizontal components of kinetic energy are concerned, this will require some assumptions about the geometry of the system. First consider a two-dimensional model repeating over a length-scale L with descending and ascending columns, of width $(1-\epsilon)L$ and ϵL respectively and with a potential temperature structure given by θ_1 and θ_2 respectively, with $\theta_2 > \theta_1$ (see Figure 2.6). Defining $\theta_{\text{ref}} = (1-\epsilon)\theta_1 + \epsilon\theta_2$ as before, the WTG approximation (Equation 2.29) implies that:

$$w_1 \frac{\partial \theta_{\text{ref}}}{\partial z} = \frac{(\theta_1 - \theta_{\text{ref}})}{\tau_{\text{WTG}}} \tag{2.42}$$

and likewise for column 2. At this stage one can ignore the interpolation in the boundary layer. As before, we use the Lorenz (1955) expression for available potential energy (APE) per unit surface area which for this two-column case can be written as:

$$\bar{A} = \frac{\kappa c_p}{2g p_0^\kappa} \int_0^{p_{\text{SURF}}} \bar{p}^{(\kappa-1)} \left(\frac{-\partial \theta_{\text{ref}}}{\partial p} \right)^{-1} \left[(1-\epsilon)(\theta_1 - \theta_{\text{ref}})^2 + \epsilon(\theta_2 - \theta_{\text{ref}})^2 \right] \mathrm{d}p \tag{2.43}$$

$$= \frac{\kappa c_p}{2g p_0^\kappa} \int_0^{p_{\text{SURF}}} \bar{p}^{(\kappa-1)} \left(-\frac{\partial \theta_{\text{ref}}}{\partial p} \right)^{-1} \left[\epsilon(1-\epsilon)(\theta_2 - \theta_1)^2 \right] \mathrm{d}p \quad . \tag{2.44}$$

Expressing $\frac{\partial \theta_{\text{ref}}}{\partial p}$ as $-\frac{\theta_{\text{ref}} N^2}{\bar{\rho} g}$, we can obtain an expression for $\bar{A}$:

$$\bar{A} = \frac{g\epsilon(1-\epsilon)\kappa c_p}{2p_0^\kappa} \int_0^{p_{\text{surf}}} \bar{\rho}\bar{p}^{(\kappa-1)} \frac{(\theta_2 - \theta_1)^2}{N^2 \theta_{\text{ref}}} \mathrm{d}p \tag{2.45}$$

$$= \frac{g\epsilon(1-\epsilon)\kappa c_p}{2R} \int_0^{p_{\text{surf}}} \frac{(\theta_2 - \theta_1)^2}{N^2 \theta_{\text{ref}}^2} \mathrm{d}p \tag{2.46}$$

$$= \frac{g\epsilon(1-\epsilon)}{2} \int_0^{p_s} \frac{(\theta_2 - \theta_1)^2}{N^2 \theta_{\text{ref}}^2} \mathrm{d}p \quad . \tag{2.47}$$

Next, we can calculate a column-integrated vertical kinetic energy per unit surface area K_v as follows:

$$K_v = \frac{1}{2\tau_{\text{WTG}}^2} \int_0^\infty \bar{\rho} \left[(1-\epsilon)(\theta_1 - \theta_{\text{ref}})^2 + \epsilon(\theta_2 - \theta_{\text{ref}})^2 \right] \left(\frac{d\theta_{\text{ref}}}{dz} \right)^{-2} dz \tag{2.48}$$

$$= \frac{\epsilon(1-\epsilon)}{2g\tau_{\text{WTG}}^2} \int_0^{p_{\text{SURF}}} (\theta_1 - \theta_2)^2 \left(\frac{d\theta_{\text{ref}}}{dz} \right)^{-2} dp \tag{2.49}$$

$$= \frac{\epsilon(1-\epsilon)g}{2\tau_{\text{WTG}}^2} \int_0^{p_{\text{SURF}}} \frac{(\theta_1 - \theta_2)^2}{N^4 \theta_{\text{ref}}^2} dp \tag{2.50}$$

$$\approx \frac{\bar{A}}{\tau_{\text{WTG}}^2 N^2} \quad , \tag{2.51}$$

having assumed a constant value of N for the two columns. The calculation of the horizontal component of kinetic energy requires the use of the continuity equation in the Boussinesq form: $\frac{\partial w}{\partial z} = -\frac{\partial u}{\partial x}$. One can express $\frac{\partial w_i}{\partial z}$ for $i = 1, 2$ as follows:

$$\frac{\partial w_i}{\partial z} = \frac{1}{\tau_{\text{WTG}}} \frac{\partial[(\theta_i - \theta_{\text{ref}})(\frac{\partial \theta_{\text{ref}}}{\partial z})^{-1}]}{\partial z} \tag{2.52}$$

$$= \frac{g}{N^2 \tau_{\text{WTG}}} \frac{\partial[\frac{(\theta_i - \theta_{\text{ref}})}{\theta_{\text{ref}}}]}{\partial z} \tag{2.53}$$

$$= \frac{g}{N^2 \tau_{\text{WTG}}} \left[\frac{1}{\theta_{\text{ref}}} \frac{\partial(\theta_i - \theta_{\text{ref}})}{\partial z} - \frac{(\theta_i - \theta_{\text{ref}})}{\theta_{\text{ref}}^2} \frac{\partial \theta_{\text{ref}}}{\partial z} \right] \quad . \tag{2.54}$$

Again one can use the assumption that N is constant for the two columns. The first term on the RHS depends on $\frac{\partial(\theta_i - \theta_{\text{ref}})}{\partial z}$. If one regards column 2 as a perturbation to column 1 arising from additional surface heating, $\frac{\partial(\theta_i - \theta_{\text{ref}})}{\partial z}$ will to first order be the ratio of optical depth to geometric depth times $\theta' = (\theta_i - \theta_{\text{ref}})$. In the simplified model described in section 2.2, this ratio varies with height due to pressure broadening, but for these purposes can be approximated using a scale height:

$$H_{\text{LW}} = -\frac{\theta'}{\partial \theta'/\partial z} \quad . \tag{2.55}$$

The second term on the RHS poses less difficulty:
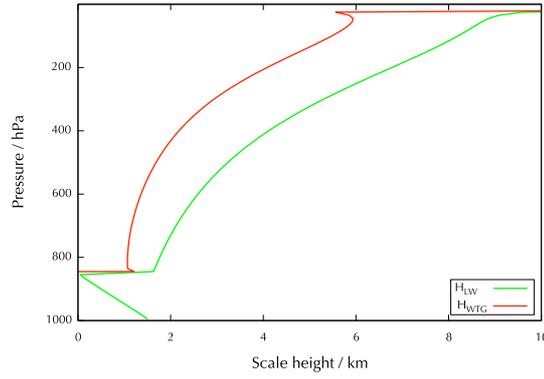
Figure 2.7: *Scale heights derived from a simplified model with pressure broadening for an atmospheric optical depth of 3.*

$$\frac{\partial w_i}{\partial z} = \frac{g}{N^2 \tau_{\text{WTG}}} \frac{(\theta_i - \theta_{\text{ref}})}{H_{\text{LW}} \theta_{\text{ref}}} - \frac{1}{\tau_{\text{WTG}}} \frac{(\theta_i - \theta_{\text{ref}})}{\theta_{\text{ref}}} \tag{2.56}$$

$$= w_i \left(\frac{-1}{H_{\text{LW}}} - \frac{N^2}{g} \right) \quad . \tag{2.57}$$

Defining a scale height for the WTG model, H_{WTG}:

$$\frac{1}{H_{\text{WTG}}} = \frac{1}{H_{\text{LW}}} + \frac{N^2}{g} \quad . \tag{2.58}$$

Figure 2.7 shows values of $H_{\text{WTG}} = \frac{w}{\partial w / \partial z}$ and $H_{\text{LW}} = -\frac{\theta'}{\partial \theta' / \partial z}$ produced by the simplified model described in section 2.2 for an optical depth of 3. Above the PBL but in the lower troposphere, where the contribution to kinetic energy will be greatest in a dry configuration (see vertical velocities in Figure 2.4), a value for H_{WTG} of 2 km seems reasonable.

Using $u(x) = \int_0^x \frac{\partial u}{\partial x'} dx'$, and assuming $x = 0$ in the centre of each column, in the ascending column we have $u_2 = -\frac{w_2 x}{H_{\text{WTG}}}$ reaching values of $u_2^* = \mp \frac{w_2 \epsilon L}{2 H_{\text{WTG}}}$ at the edges of the column, where x is the distance from the centre of the column. Likewise in the descending column we have $u_1 = \frac{w_1 x'}{H_{\text{WTG}}}$, with extrema of $u_1^* = \pm \frac{w_1 (1-\epsilon) L}{2 H_{\text{WTG}}}$ which equals u_2 at the edges of the columns since $(1-\epsilon) w_1 = -\epsilon w_2$.

These values of u can be used to calculate a value for the Horizontal Kinetic Energy per unit surface area K_h as follows:

$$K_h = \frac{1}{2LH_{\text{WTG}}^2} \int_0^\infty \bar{\rho} \left[\int_{-\epsilon L/2}^{\epsilon L/2} w_2^2 x^2 \mathrm{d}x + \int_{-(1-\epsilon)L/2}^{(1-\epsilon)L/2} w_1^2 x'^2 \mathrm{d}x' \right] \mathrm{d}z \tag{2.59}$$

$$= \frac{1}{24LH_{\text{WTG}}^2} \int_0^\infty \bar{\rho} \left[\epsilon^3 L^3 w_2^2 + (1-\epsilon)^3 L^3 w_1^2 \right] \mathrm{d}z \tag{2.60}$$

$$= \frac{\epsilon^2 L^2}{24 H_{\text{WTG}}^2} \int_0^\infty \bar{\rho} w_2^2 \mathrm{d}z \quad . \tag{2.61}$$

Noting that:

$$K_v = \frac{1}{2} \int_0^\infty \bar{\rho} \left[(1-\epsilon) w_1^2 + \epsilon w_2^2 \right] \mathrm{d}z \tag{2.62}$$

$$= \frac{\epsilon}{2(1-\epsilon)} \int_0^\infty \bar{\rho} w_2^2 \mathrm{d}z \quad . \tag{2.63}$$

one can conclude that

$$K_h = \frac{\epsilon(1-\epsilon)L^2}{12 H_{\text{WTG}}^2} K_v \tag{2.64}$$

$$= \frac{\epsilon(1-\epsilon)L^2}{12 \tau_{\text{WTG}}^2 N^2 H_{\text{WTG}}^2} \bar{A} \quad . \tag{2.65}$$

It is possible to extend the above analysis to a three-dimensional model in which the ascending column ($\theta_2 > \theta_1$) is contained within a cylinder of radius R_1, itself within a larger cylinder of radius R_2 the remainder of which contains the descending column. It will be seen that $\epsilon = R_1^2 / R_2^2$ and the previously derived expressions for APE and vertical kinetic energy per unit surface area remain valid. The horizontal velocity can be calculated using the continuity equation in cylindrical coordinates:

$$\frac{1}{r} \frac{\partial(ru)}{\partial r} = -\frac{\partial w}{\partial z} \quad . \tag{2.66}$$

For $r < R_1$ one can write:

$$\frac{\partial(r u)}{\partial r} = -\frac{r w_2}{H_{\text{WTG}}} \quad , \tag{2.67}$$

and since by symmetry $u = 0$ at the centre of the system this implies:

$$u = -\frac{r w_2}{2 H_{\text{WTG}}} \quad . \tag{2.68}$$

This gives a maximum value of $u^* = -\frac{R_1 w_2}{2 H_{\text{WTG}}}$ for $r = R_1$. For $R_1 \leq r \leq R_2$ (remembering that $w_2 \geq 0$ and $w_1 \leq 0$):

$$u = \frac{R_1 u^*}{r} - \frac{r w_1}{2 H_{\text{WTG}}} + \frac{R_1^2 w_1}{2 H_{\text{WTG}} r} \tag{2.69}$$

$$= \frac{-r w_1}{2 H_{\text{WTG}}} - \frac{R_1^2 (w_2 - w_1)}{2 H_{\text{WTG}} r} \tag{2.70}$$

$$= \frac{-r w_1}{2 H_{\text{WTG}}} + \frac{R_1^2 w_1}{2 H_{\text{WTG}} r \epsilon} \quad . \tag{2.71}$$

One can note that when $r = R_2 = R_1 \epsilon^{-1/2}$ that $u = 0$. For $r \geq R_2$ we have $u, w = 0$.

The horizontal kinetic energy contained in one vertical level of the ascending column is thus:
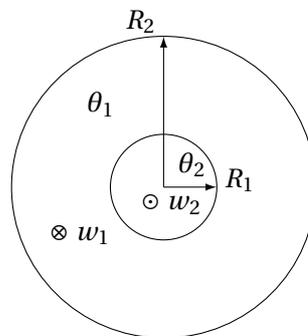
Figure 2.8: *Cross-section of model structure for 3 dimensions (looking down).*

$$\delta K_h = \frac{1}{2} \int_0^{R_1} \bar{\rho} \left[2\pi u^2 r \right] \mathrm{d}r \tag{2.72}$$

$$= \frac{\pi \bar{\rho} w_2^2}{4 H_{\text{WTG}}^2} \int_0^{R_1} r^3 \mathrm{d}r = \frac{\pi \bar{\rho} w_2^2 R_1^4}{16 H_{\text{WTG}}^2} \quad . \tag{2.73}$$

Likewise for the descending cylinder:

$$\delta K_h = \frac{1}{2} \int_{R_1}^{R_2} \bar{\rho} \left[2\pi u^2 r \right] \mathrm{d}r \tag{2.74}$$

$$= \frac{\pi \bar{\rho} w_1^2}{4 H_{\text{WTG}}^2} \int_{R_1}^{R_2} \left(r - \frac{R_2^2}{r} \right)^2 r \mathrm{d}r \tag{2.75}$$

$$= \frac{\pi \bar{\rho} w_1^2}{4 H_{\text{WTG}}^2} \int_{R_1}^{R_2} \left(r^3 - 2 R_2^2 r + \frac{R_2^4}{r} \right) \mathrm{d}r \tag{2.76}$$

$$= \frac{\pi \bar{\rho} w_1^2}{4 H_{\text{WTG}}^2} \left(\frac{R_2^4}{4} - \frac{R_1^4}{4} - R_2^4 + R_2^2 R_1^2 + R_2^4 \log \frac{R_2}{R_1} \right) \tag{2.77}$$

$$= \frac{\pi \bar{\rho} w_1^2 R_2^4}{16 H_{\text{WTG}}^2} \left(4\epsilon - 3 - \epsilon^2 - 2 \log \epsilon \right) \quad . \tag{2.78}$$

The total kinetic energy per unit area for the entire layer is thus:

$$\delta K_h = \frac{\bar{\rho} w_2^2 R_2^2}{16 H_{\text{WTG}}^2} \left[\epsilon^2 + \frac{\epsilon^2}{(1-\epsilon)^2} \left(4\epsilon - 3 - \epsilon^2 - 2 \log \epsilon \right) \right] \tag{2.79}$$

$$= \frac{\bar{\rho} w_2^2 R_2^2 \epsilon^2}{16 H_{\text{WTG}}^2} \frac{(2\epsilon - 2 - 2 \log \epsilon)}{(1-\epsilon)^2} \quad . \tag{2.80}$$

Integrating over the column:

$$K_h = \frac{\epsilon R_2^2}{4 H_{\text{WTG}}^2} \left(-1 - \frac{\log \epsilon}{(1-\epsilon)} \right) K_v \tag{2.81}$$

$$= \frac{\epsilon R_2^2}{4 \tau_{\text{WTG}}^2 N^2 H_{\text{WTG}}^2} \left(-1 - \frac{\log \epsilon}{(1-\epsilon)} \right) \bar{A} \quad . \tag{2.82}$$

Given that the mechanism which serves to eliminate the buoyancy deviation between the two columns is a gravity wave one can reasonably assume a relationship between the group veloc-

ity of the gravity wave, the distance between the two columns and the WTG relaxation time. In the linear (two dimensional) case one can consider that the relaxation time corresponds to the time that it takes for the gravity wave to transfer energy across the length of the domain:

$$c_{gx} = \frac{L}{\tau_{\text{WTG}}} = \frac{N m^2}{(k^2 + m^2)^{3/2}} \quad , \tag{2.83}$$

where k and m represent horizontal and vertical wave numbers respectively (see Holton and Hakim, 2013, Equation 5.67). This implies that (using Equation 2.65):

$$K_h = \frac{\epsilon(1-\epsilon) m^4}{12(k^2 + m^2)^3 H_{\text{WTG}}^2} \bar{A} \quad . \tag{2.84}$$

It is reasonable to assume that $m \gg k$ and so taking $m = \frac{\pi}{H_{\text{Trop}}}$:

$$\tau_{\text{WTG}} = \frac{L\pi}{N H_{\text{Trop}}} \tag{2.85}$$

$$K_h = \frac{\epsilon(1-\epsilon) H_{\text{Trop}}^2}{12\pi^2 H_{\text{WTG}}^2} \bar{A} \quad . \tag{2.86}$$

Figure 2.7 suggested a value for H_{WTG} of 2 km, and taking H_{Trop} as 15 km (appropriate for the tropics) one can estimate:

$$K_h = \frac{\epsilon(1-\epsilon) H_{\text{Trop}}^2}{12\pi^2 H_{\text{WTG}}^2} \bar{A} \approx 0.47 \epsilon(1-\epsilon) \bar{A} \quad . \tag{2.87}$$

The dependency of $K_h / \bar{A}$ on ϵ is plotted in Figure 2.9. The maximum value of $\epsilon(1-\epsilon)$ is 0.25 and for a typical value of ϵ of 0.02 the value would also be 0.02. Thus this implies a maximum value for horizontal kinetic energy of 12% of $\bar{A}$ and a more typical value one tenth of that.

In the 3 dimensional cylindrical case, one can associate the relaxation time to the time taken for the wave to transfer energy across the radius of the system:

$$c_{gx} = \frac{R_2}{\tau_{\text{WTG}}} \quad . \tag{2.88}$$
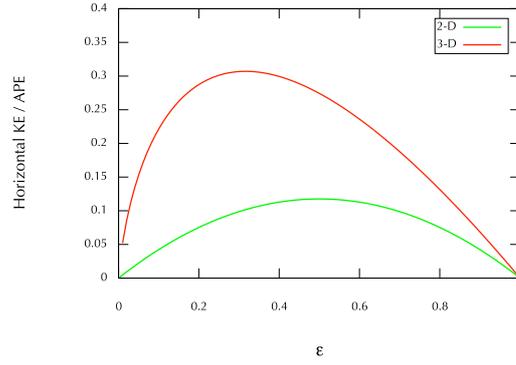
Figure 2.9: *The dependency of the ratio of horizontal kinetic energy to APE with the convective fraction ϵ for the linear (two-dimensional) and cylindrical (three-dimensional) geometries.*

As before, this produces:

$$K_h = \frac{H_{\text{Trop}}^2 \epsilon}{4\pi^2 H_{\text{WTG}}^2} \left(-1 - \frac{\log\epsilon}{(1-\epsilon)} \right) \bar{A} = 1.42\epsilon \left(-1 - \frac{\log\epsilon}{(1-\epsilon)} \right) \bar{A} \quad . \tag{2.89}$$

This has a maximum of 30% of $\bar{A}$ (for $\epsilon \approx 0.32$) and a more typical value of 8%$\bar{A}$.

The vertical kinetic energy depends on the aspect ratio of the system irrespective of the geometry considered:

$$K_v = \frac{\bar{A}}{\tau_{\text{WTG}}^2 N^2} = \frac{H_{\text{Trop}}^2}{\pi^2 L^2} \bar{A} \quad , \tag{2.90}$$

and will be very much less than the horizontal terms except for systems where L is of the order of 10 km or less.

Extending this model to include friction with Rayleigh damping, with a timescale τ_{Ray}, then one can assume that the friction term balances the creation of horizontal kinetic energy through the WTG. Thus:

$$\frac{2\bar{A}}{\tau_{\text{WTG}}} = \frac{2K_h}{\tau_{\text{Ray}}} \quad . \tag{2.91}$$

$$\implies \tau_{\text{Ray}} = \frac{K_h}{\bar{A}} \tau_{\text{WTG}} \quad . \tag{2.92}$$

This gives, for example in the 3D case:

$$\tau_{\text{Ray,3D}} = \frac{H_{\text{Trop}}^2 \epsilon}{4\pi^2 H_{\text{WTG}}^2} \left(-1 - \frac{\log \epsilon}{(1-\epsilon)} \right) \bar{A} = 1.44 \epsilon \left(-1 - \frac{\log \epsilon}{(1-\epsilon)} \right) \tau_{\text{WTG}} \quad . \tag{2.93}$$

Given that τ_{WTG} is typically in a range 3-12 hours, the above analyses suggest timescales for τ_{Ray} of the order of 1 hour, very much less than the day or so typically observed (see Romps (2013)). In the dry case analysed above, where the majority of the motion occurs within the boundary layer, the effective τ_{WTG} is of course greater than those values, but as the relationship in Equation 2.93 will also apply in general another explanation is also necessary. This point is investigated further in section 2.7.

Note also that a similar approach with a geometrical framework based on a continuous field in Romps (2012b, Equation 13) gives:

$$\tau_{\text{Ray}} = \frac{\pi^2 L^2}{N^2 H_{\text{Trop}}^2 \tau_{\text{WTG}}} \quad . \tag{2.94}$$

Substituting from Equation 2.85, one can obtain $\tau_{\text{Ray}} = \tau_{\text{WTG}}$, which is again inconsistent with typical values used for these timescales. The next section shows how introducing azimuthal as well as radial winds can produce a more consistent set of values.

2.7 Stable convecting systems with azimuthal winds

The previous section showed how the energy cycle in a WTG model could be expressed in terms of conversions from APE to vertical kinetic energy and hence to horizontal kinetic energy in an overturning circulation with a geometry based on a cylinder of ascending air contained within a larger cylinder of descending air. We saw that for this set-up to achieve a stable equilibrium the effect of friction would have to be significantly greater than that typically modelled in idealised studies. In order to identify a stable equilibrium one can introduce a tangential (azimuthal) component of wind velocity as shown in Figure 2.10

The Boussinesq continuity equation can be written in cylindrical coordinates as
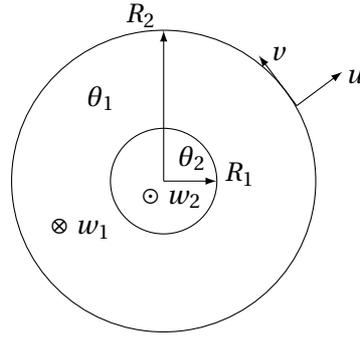
Figure 2.10: *Cross-section of model structure for 3 dimensions (looking down).*

$$\nabla.\mathbf{u} = \frac{1}{r}\frac{\partial(r u)}{\partial r} + \frac{1}{r}\frac{\partial v}{\partial \phi} + \frac{\partial w}{\partial z} = 0 \quad , \tag{2.95}$$

where ϕ is the azimuthal angle. Assuming an axisymmetric solution $\frac{\partial v}{\partial \phi} = 0$ gives the same relationship between u and w as in the case without axial motion. The momentum equations for the two horizontal dimensions can be expressed in cylindrical form as:

$$\frac{\partial u}{\partial t} + \frac{v}{r}\frac{\partial u}{\partial \phi} + u\frac{\partial u}{\partial r} - v\left(\frac{v}{r} + f\right) + w\frac{\partial u}{\partial z} = \mathcal{U} \quad , \tag{2.96}$$

$$\frac{\partial v}{\partial t} + \frac{v}{r}\frac{\partial v}{\partial \phi} + u\frac{\partial v}{\partial r} + u\left(\frac{v}{r} + f\right) + w\frac{\partial v}{\partial z} = \mathcal{V} \quad , \tag{2.97}$$

where $\mathcal{U}$ and $\mathcal{V}$ are forcing terms and $f = 2\Omega \sin(\text{latitude})$ is the Coriolis parameter, Ω being the rate of rotation of the Earth. Assuming an axisymmetric solution one can derive equations for the rate of change of the two horizontal components of kinetic energy:

$$\frac{\partial \frac{1}{2} u^2}{\partial t} + u^2\frac{\partial u}{\partial r} - uv\left(\frac{v}{r} + f\right) + wu\frac{\partial u}{\partial z} = u\mathcal{U} \quad , \tag{2.98}$$

$$\frac{\partial \frac{1}{2} v^2}{\partial t} + uv\frac{\partial v}{\partial r} + uv\left(\frac{v}{r} + f\right) + wv\frac{\partial v}{\partial z} = v\mathcal{V} \quad . \tag{2.99}$$

This indicates that the conversion from radial to tangential kinetic energy is given by $uv\left(\frac{v}{r} + f\right)$, and one can express the energy cycle diagrammatically as in Figure 2.11, where K_{Tang} and

K_{Rad} are the tangential and radial horizontal components of kinetic energy respectively. This diagram can be compared with Figure 2.5, but now includes conversion between the radial and tangential components of the flow.
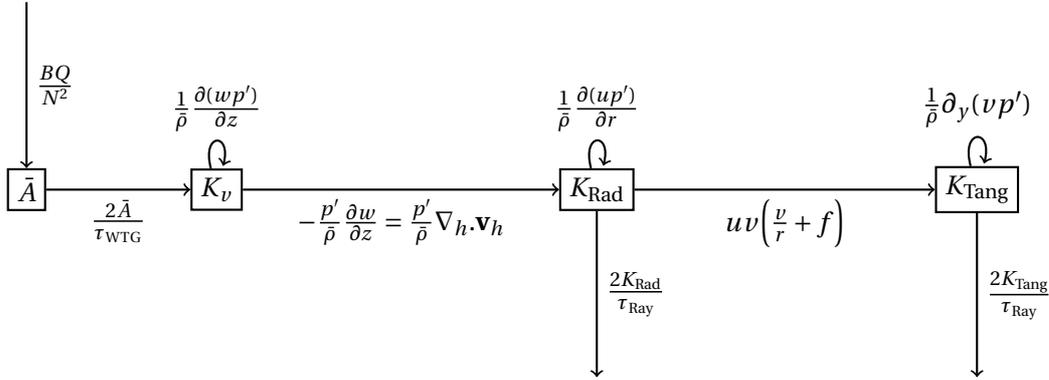
Figure 2.11: *Energy cycle for two cylinder model with tangential wind component*

For this system to achieve an equilibrium we need two separate conditions to hold globally across the system:

$$\frac{2\bar{A}}{\tau_{\text{WTG}}} = \frac{2K_{\text{Rad}}}{\tau_{\text{Ray}}} + \frac{2K_{\text{Tang}}}{\tau_{\text{Ray}}} \quad . \tag{2.100}$$

$$\frac{2K_{\text{Tang}}}{\tau_{\text{Ray}}} = uv\left(\frac{v}{r} + f\right) \quad . \tag{2.101}$$

Of course, the conversion of external heating to APE (BQ/N^2) will also need to balance the dissipation of kinetic energy, but our focus here is on the relationship between the creation and destruction of kinetic energy. We can simplify the problem further, by approximating azimuthal wind by $v = \eta u$, where η is constant throughout the system. This is suggested by the observed structure of the primary circulation inside a tropical cyclone where there is evidence of constant mean in-flow angles (Frank, 1977). The first relationship above (Equation 2.100) can be used to derive:

$$\eta^2 = \frac{\tau_{\text{Ray}}\bar{A}}{\tau_{\text{WTG}}K_{\text{Rad}}} - 1 \quad \text{or} \tag{2.102}$$

$$\eta^2 = \frac{4\pi^2\tau_{\text{Ray}}H_{\text{WTG}}^2}{\tau_{\text{WTG}}H_{\text{Trop}}^2\epsilon\left(-1 - \frac{\log\epsilon}{(1-\epsilon)}\right)} - 1 \quad , \tag{2.103}$$

using the relationship previously developed (in the absence of boundary layer effects). These expressions suggest that there is a maximum value of τ_{WTG} for a given value of ϵ for which $\eta = 0$; for greater values of τ_{WTG} no overturning circulation can be sustained, which implies a maximum size L for convective systems - at this limit there is no azimuthal circulation so the second condition is trivially met. The second relationship less straightforward. Locally it can be rewritten as:

$$\frac{\eta^2 u^2}{\tau_{\mathrm{Ray}}} = \frac{\eta^2 u^3}{r} + \eta f u^2 \quad , \tag{2.104}$$

but this remains relatively intractable analytically.

More usefully, we can obtain numeric values of η for the entire system which represent an equilibrium for fixed values of $\tau_{\mathrm{WTG}}, \tau_{\mathrm{Ray}}, \epsilon$ and f. Using Equation 2.88 we can in fact replace τ_{WTG} by R_2. The model also allows for the boundary layer effects which have hitherto been neglected in the analysis. The two graphs in Figure 2.12 show values of η and R_2 for which the two conditions (Equations 2.103 and 2.104) hold for values of f corresponding to 15°N and 30°N and $\epsilon = 0.05$ and 0.3. The value of τ_{Ray} used in these calculations is 1 day.

The results with $\epsilon = 0.30$ (a value of ϵ which maximises vertical kinetic energy) indicate that a stable rotating convecting system can exist in the tropics with radius ≈ 1350 km in the lower tropics and 700 km in the higher tropics. The maximum size for a non-rotating convecting system is of the order of 4000 km, which would correspond to a τ_{WTG} of the order of around 25 hours. If $\epsilon = 0.05$ these length scales become 2000 km, 1000 km and 7000 km respectively.

It is intriguing that a relatively simple model produces results for the sizes of stable convecting systems in the tropics which are similar to those observed in practice (Wing and Emanuel, 2014), despite many of the moist and radiative processes that contribute to the development of such systems not being represented here. This suggests that a possible analysis based on the timescales at which these processes operate and the speed at which their effects are prop-

$$\epsilon = 0.05 \qquad\qquad\qquad \epsilon = 0.30$$
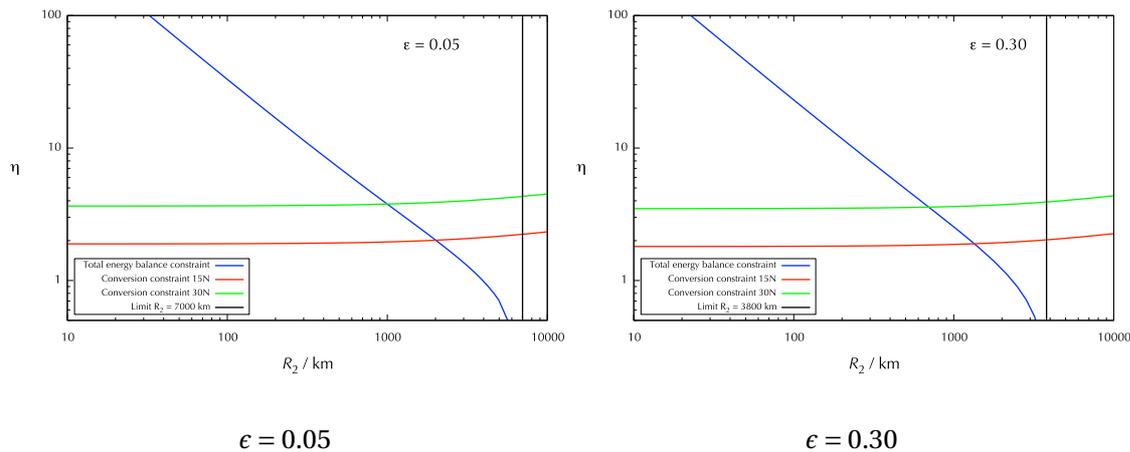
Figure 2.12: *Values of η (the ratio of axial to radial motion) implied by the two conditions on energy balance. A equilibrium state exists where the total energy balance constraint (blue, Equation 2.103) crosses the conversion constraint curve (Equation 2.104) for the appropriate latitude (green for $30°\mathrm{N}$ and red for $15°\mathrm{N}$). A second equilibrium state exists where the energy balance curve crosses the x axis - this value of R_2 is indicated by a black line. The timescale parameter for frictional dissipation is taken to be 1 day and ϵ, the convective area fraction, is 0.05 in the left hand panel and 0.3 in the right.*

agated might give rise to a better understanding of the length-scales in tropical convection.

2.8 How WTG coupling modifies temperature profiles

We can develop expressions for the potential temperature profile in two WTG-coupled columns based on a linear approximation, and use this to calculate certain energetic diagnostics. These depend on the equilibrium potential temperature profiles in the two-column system with no WTG coupling and on a heuristically obtained radiative relaxation timescale T_{Rad}, which varies with height and the depth of the boundary layer over which the WTG approximation is interpolated (discussed below), but does not depend on any other aspects of the system. Versions of these expressions are also valid within the boundary layer. These elements can be combined to obtain an understanding of the dependence of the key energetic variables of the system on the coupling strength of the WTG approximation.

Consider the model previously discussed, consisting of two columns representing two regions with distinct fixed SSTs in an equilibrium state with potential temperature profiles θ_1 and θ_2 and of respective size$(1-\epsilon)$ and ϵ coupled through the WTG approximation with timescale τ_{WTG}

- with interpolation of ω in the boundary layer. Let $\theta' = \theta_2 - \theta_1$. Also let Θ_1, Θ_2, Θ' represent these quantities in the case $\tau = \infty$, i.e. the equivalent values for two uncoupled columns.

Above the boundary layer, at equilibrium, one can express a relationship between the radiative forcing in terms of a relaxation time T_{Rad} and the advection implied by the WTG. For column 2 this has the form:

$$\frac{(\Theta_2 - \theta_2)}{T_{\text{Rad}}} = \frac{(\theta_2 - \theta_{\text{ref}})}{\tau_{\text{WTG}}} \tag{2.105}$$

$$= (1 - \epsilon)\frac{(\theta_2 - \theta_1)}{\tau_{\text{WTG}}} \quad . \tag{2.106}$$

Combining this with a similar expression for Column 1:

$$\frac{(\theta_1 - \Theta_1)}{\epsilon T_{\text{Rad}}} = \frac{(\theta_2 - \theta_1)}{\tau_{\text{WTG}}} = \frac{(\Theta_2 - \theta_2)}{(1 - \epsilon)T_{\text{Rad}}} \quad . \tag{2.107}$$

There is no reason to suspect that T_{Rad} has a dependence on the other parameters of the system, so we will assume that it is only a function of height. This hypothesis will be validated below. We also assume that to first order the WTG-coupling serves to eliminate horizontal anomalies and does not result in vertical heat transport across the entire system, hence that $(1 - \epsilon)\Theta_1 + \epsilon\Theta_2 = (1 - \epsilon)\theta_1 + \epsilon\theta_2$. (A comparison of the results obtained with these assumptions and results from the model will confirm that these assumptions are reasonable at this stage, although this point will be revisited in sections 2.9 and 2.10.) Equation 2.107 can be manipulated to produce:

$$\theta' = \frac{\tau_{\text{WTG}}}{(\tau_{\text{WTG}} + T_{\text{Rad}})}\Theta' \quad . \tag{2.108}$$

We can express the effect of the interpolation in the boundary layer in terms of an effective relaxation timescale $\tau^* = \beta(\tau_{\text{WTG}}, p)\tau_{\text{WTG}}$ where $\beta(\tau_{\text{WTG}}, p)$ is a coefficient representing the effect of the boundary layer interpolation. Then - assuming the interpolation in the boundary layer is linear in pressure coordinates- we can write:

$$\beta(\tau_{\text{WTG}}, p) = \frac{(p_{\text{SURF}} - p_{\text{BL}})\theta'}{(p_{\text{SURF}} - p)\theta'_{\text{BL}}} \quad . \tag{2.109}$$

where p_{BL} is the pressure at the top of the boundary layer and θ'_{BL} the potential temperature difference at that height. The algebra is simpler if we define T_{Rad} in the boundary layer so that $T^*_{\text{Rad}} = \beta(\infty, p) T_{\text{Rad}}$ is the radiative relaxation timescale. $\beta(\infty, p)$ will depend on the profile of two uncoupled columns and is not dependent on the WTG-coupling parameters:

$$\beta(\infty, p) = \frac{(p_{\text{SURF}} - p_{\text{BL}})\Theta'}{(p_{\text{SURF}} - p)\Theta'_{\text{BL}}} \quad . \tag{2.110}$$

The equilibrium values of θ' can as before be obtained from:

$$\frac{(\theta_1 - \Theta_1)}{\epsilon T^*_{\text{Rad}}} = \frac{(\theta_2 - \theta_1)}{\tau^*} = \frac{(\Theta_2 - \theta_2)}{(1 - \epsilon) T^*_{\text{Rad}}} \quad . \tag{2.111}$$

This gives:

$$\theta' = \frac{\tau^* \Theta'}{(\tau^* + T^*_{\text{Rad}})} = \frac{\tau_{\text{WTG}} \Theta'}{\tau_{\text{WTG}} + T_{\text{Rad}} \frac{\theta'_{\text{BL}} \Theta'}{\Theta'_{\text{BL}} \theta'}} = \frac{\tau_{\text{WTG}} \Theta'}{\tau_{\text{WTG}} + T_{\text{Rad}} \frac{\Theta' \tau_{\text{WTG}}}{(\tau_{\text{WTG}} + T_{\text{Rad}}|_{\text{BL}})\theta'}} \quad . \tag{2.112}$$

Rearranging:

$$\theta' = \left[\frac{\tau_{\text{WTG}} + T_{\text{Rad}}|_{\text{BL}} - T_{\text{Rad}}}{\tau_{\text{WTG}} + T_{\text{Rad}}|_{\text{BL}}} \right] \Theta' \quad . \tag{2.113}$$

At the top of the boundary layer, these two expressions (Equations 2.108 and 2.113) for θ' coincide. If suitable values of T_{Rad} are available and Θ_1 and Θ_2 are known, then θ_1 and θ_2 can be easily calculated. Thus once the radiative equilibrium of a two column system with no WTG coupling is known, it is possible to determine the state of the system for any value of the WTG parameter τ_{WTG}, and using the expressions derived above calculate many of the energetic parameters directly.
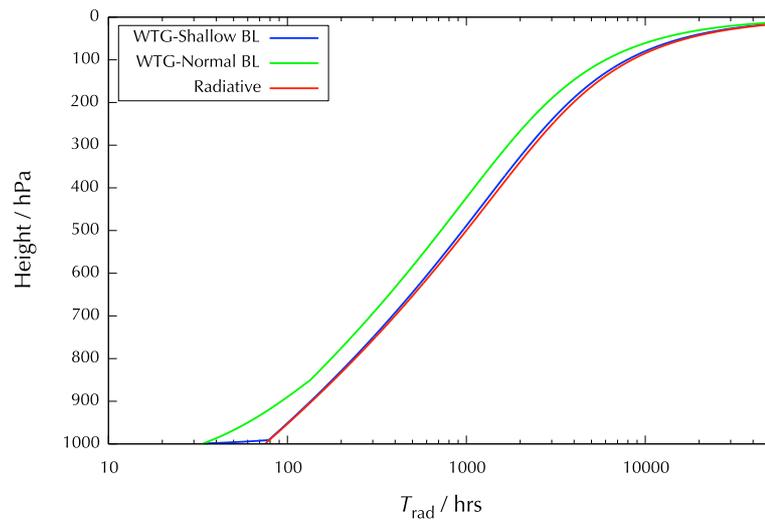
Figure 2.13: *Values of T_{Rad} estimated directly from a radiative model and those implied by the temperature profiles produced by iterative models with a boundary layer of 150 hPa ("Normal") and 8 hPa ("Shallow").*

T_{Rad} could perhaps be estimated by perturbing a radiative model for the system at equilibrium with no WTG linkage and calculating the relaxation timescale reflecting the system's return to equilibrium. Unfortunately, values obtained in this way produce an unsatisfactory result in that the values of θ' that result do not match those obtained from the coupled single column model. It is possible to solve for T_{Rad} from that model (using a fixed value of τ_{WTG}), and these values indicate that there is a strong dependency on the depth of the boundary layer in the WTG approximation, and that for very shallow boundary layers the values so derived match those from the pure radiative model (see Figure 2.13) referred to above. This dependency on the depth of the boundary layer can be explained by the fact that the values of T_{Rad} will be influenced by the entire profile, that in the boundary layer any deviation from equilibrium will be damped and that consequently there will be greater forcing towards equilibrium above the BL than would otherwise be expected, leading to a shorter relaxation time. The results shown in later sections are therefore calculated with values of T_{Rad} obtained from the model described in section 2.2.

The values of θ' derived above permit the calculation of various energetic quantities. For example APE can be expressed as:

$$\bar{A} = \frac{g\epsilon(1-\epsilon)}{2} \int_0^{p_{\text{SURF}}} \frac{\theta'^2}{N^2\theta_{\text{ref}}^2} \mathrm{d}p \quad , \tag{2.114}$$

$$= \frac{g\epsilon(1-\epsilon)}{2} \int_0^{p_{\text{BL}}} \frac{\Theta'^2 \tau_{\text{WTG}}^2}{N^2\theta_{\text{ref}}^2 (\tau_{\text{WTG}} + T_{\text{Rad}})^2} \mathrm{d}p + \frac{g\epsilon(1-\epsilon)}{2} \int_{p_{\text{BL}}}^{p_{\text{SURF}}} \frac{\Theta'^2 (\tau_{\text{WTG}} + T_{\text{Rad}}|_{\text{BL}} - T_{\text{Rad}})^2}{N^2\theta_{\text{ref}}^2 (\tau_{\text{WTG}} + T_{\text{Rad}}|_{\text{BL}})^2} \mathrm{d}p \quad . \tag{2.115}$$

The graphs in Figure 2.14 compare values of APE and of the conversion of APE to kinetic energy obtained directly from the simplified model of section 2.2 and estimated using this linearised approach for varying values of τ_{WTG}. The linear approach generally provides a satisfactory estimate for these quantities, except for unrealistically short values of τ_{WTG}, which can be attributed to convergence issues in the coupled single column model (where the CFL criterion requires very short model timesteps to ensure numerical stability, and even with quadruple precision truncation will affect advected quantities), and around the maximum conversion rate, which occurs for values of τ_{WTG} very much higher than generally used. The level of accuracy of the linearised model for a wide range of coupling parameter values suggests that the dependency of T_{Rad} on τ_{WTG} is minimal. The graphs also indicate that both APE and the conversion term tend towards a non-zero value as $\tau_{\text{WTG}} \to 0$. This is a result of the boundary layer interpolation. The APE graph also demonstrates the relationship between sorted and Lorenz APE discussed in section 2.3.

2.9 TOWARDS AN ANALYTICAL EXPRESSION FOR WORK GENERATED

Equations 2.108 and 2.113 provide an expression for the convergence of the (potential) temperature of any two columns by the WTG approximation in terms of heuristically obtained height-dependent values T_{Rad} and the WTG parameter τ_{WTG} (hereafter referred to as τ).

Consider now the potential temperature difference between two uncoupled columns; examination of model results supports the natural hypothesis that this can be expressed as a height-dependent multiple of the temperature difference at the surface ΔT_s: $\Theta_2(p) - \Theta_1(p) = R_{\text{fac}}(p)\Delta T_s$, where ΔT_s is the SST difference between the columns. A plot of values of $\Pi(p)R_{\text{fac}}$ obtained

APE
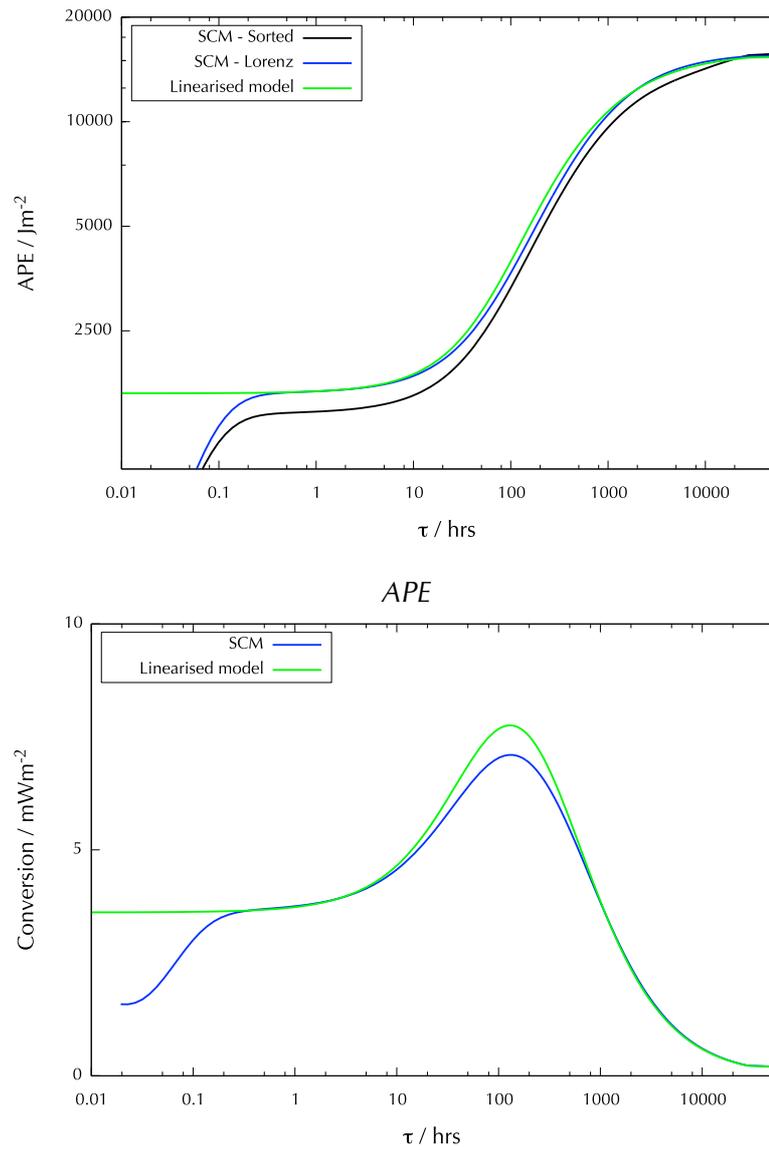
Conversion of APE to kinetic energy

Figure 2.14: *Comparison of values obtained directly from the coupled single column model of section 2.2 of with those calculated using the linearised model approach for varying values of τ_{WTG}. Note also the relationship between "Sorted' and "Lorenz" APE. Model parameters are $\epsilon = 0.1$ and SST difference of 2 K.*

from the model is shown in Figure 2.15. The Exner function $\Pi(p) = \left(\frac{p}{p_0}\right)^\kappa$ is included in the plot purely for presentational reasons. This approximation seems to work for a wide range of ΔT_s.

Above the boundary layer one can use Equation 2.38 for conversion of APE to kinetic energy:

$$\dot{L} = 2\bar{A}/\tau \; .$$

$$\dot{L}_{>\text{BL}} = \frac{R_d}{g p_0^\kappa \tau} \int_0^{p_{\text{BL}}} \frac{p^{\kappa-1}\theta'^2}{-\frac{\partial \theta_{\text{ref}}}{\partial p}} \mathrm{d}p \quad , \tag{2.116}$$

$$= \frac{R_d \epsilon (1-\epsilon)\tau}{g p_0^\kappa} \int_0^{p_{\text{BL}}} \frac{p^{\kappa-1} R_{\text{fac}}^2}{-\frac{\partial \theta_{\text{ref}}}{\partial p}(\tau + T_{\text{Rad}})^2} \mathrm{d}p (\Delta T_s)^2 \quad , \text{which can be written in the form:}$$

$$\tag{2.117}$$

$$= L_1(\tau)(\Delta T_s)^2 \quad . \tag{2.118}$$

Within the boundary layer we rely on a different expression for $\dot{L}$. The local conversion term can be written in (x, y, z) space as $-\rho w g$ (see Ambaum, 2010, p. 205). This gives:

$$\dot{L} = \int_0^{z_{\text{BL}}} -\rho w g \, dz \quad , \tag{2.119}$$

$$= \int_{p_{\text{SURF}}}^{p_{\text{BL}}} w \, dp \quad . \tag{2.120}$$

Using $w_i = \frac{-\omega_i}{\rho_i g} = \frac{-\omega_i R T_i}{p g}$, and $\omega_i(p) = \omega_i(p_{\text{BL}}) \frac{(p - p_{\text{SURF}})}{(p_{\text{BL}} - p_{\text{SURF}})}$:

$$\dot{L}_{<\text{BL}} = \int_{p_{\text{BL}}}^{p_{\text{SURF}}} ((1-\epsilon) w_1 + \epsilon w_2) \mathrm{d}p \quad , \tag{2.121}$$

$$= \frac{R_d \epsilon (1-\epsilon)}{g \tau} \int_{p_{\text{BL}}}^{p_{\text{SURF}}} \frac{(T_2 - T_1)(\theta_2(p_{\text{BL}}) - \theta_1(p_{\text{BL}})(p - p_{\text{SURF}})}{-p \frac{\partial \theta_{\text{ref}}}{\partial p}\big|_{\text{BL}} (p_{\text{BL}} - p_{\text{SURF}})} \mathrm{d}p \quad , \tag{2.122}$$

$$= \frac{R_d \epsilon (1-\epsilon)}{g p_0^\kappa} \int_{p_{\text{BL}}}^{p_{\text{SURF}}} \frac{R_{\text{fac}}(p_{\text{BL}}) R_{\text{fac}}(p) p^{\kappa-1} (\tau + T_{\text{Rad}}|_{\text{BL}} - T_{\text{Rad}}))(p - p_{\text{SURF}})}{-\frac{\partial \theta_{\text{ref}}}{\partial p}\big|_{\text{BL}} (\tau + T_{\text{Rad}}|_{\text{BL}})^2 (p_{\text{BL}} - p_{\text{SURF}})} \mathrm{d}p (\Delta T_s)^2$$

$$\tag{2.123}$$

$$= L_2(\tau)(\Delta T_s)^2 \quad \text{(as for } L_1 \text{ above).} \tag{2.124}$$

Thus:

$$\dot{L} = (L_1(\tau) + L_2(\tau))(\Delta T_s)^2 \quad . \tag{2.125}$$

In order to calculate values of L_1, L_2, we can use the values of $\frac{\partial \theta_{\text{ref}}}{\partial p}$ derived from the convective equilibrium state which will not depend on the coupling strength. These expressions are complex, and are best calculated numerically. A comparison of $\dot{L}$ as expressed above based on the uncoupled profile for θ_{ref} and values obtained from the numerical model is shown in Figure
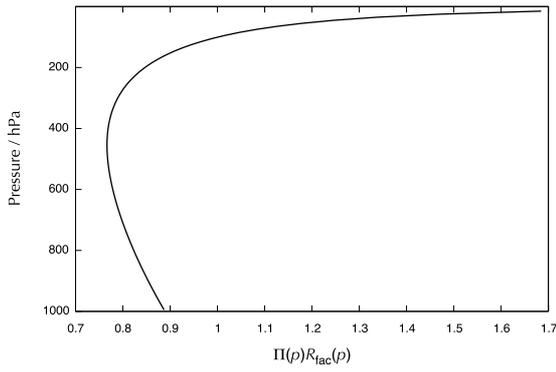
Figure 2.15: *Values of $\Pi(p)R_{\mathrm{fac}}(p)$ estimated from the numerical model for $\delta_{\mathrm{LW}} = 3$.*
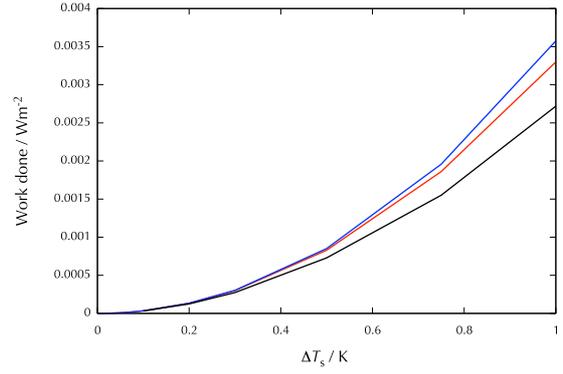
Figure 2.16: *Estimates of the mechanical work done from numerical model (black), using Equation 2.125 with the $\partial\theta/\partial p$ profile for the radiative-convective equilibrium state (red) and with the actual $\partial\theta/\partial p$ profile (blue). Model parameters include $\epsilon = 0.5$ and constant heat input consistent with an SST of 295 K for $\Delta T_s = 0$.*

2.16. The model keeps the heat input into the system constant, by reducing T_1, T_2 as ΔT_s is increased - this assumption has a minimal effect on $\dot{L}$. Results indicate that the approximation is accurate to within 80 % for $\Delta T_s < 1$ K. A calculation based on the $\frac{\partial\theta_{\mathrm{ref}}}{\partial p}$ of the actual temperature profile, rather than that of the radiative equilibrium is also shown. The difference between the model and the values calculated from the analytical expressions arises from the fact that the θ_{ref} profile changes as the temperature difference between the two columns increases (Figure 2.17), as do the values of T_{rad} (Figure 2.18).

The effect of increasing ΔT_s from 0 is for the resulting advection to modify the θ_{ref} profile quadratically (Figure 2.17) as both the vertical wind and temperature difference between the columns increase linearly. This results in cooling in the lowest layers of this atmosphere and warming near the top of the boundary layer.
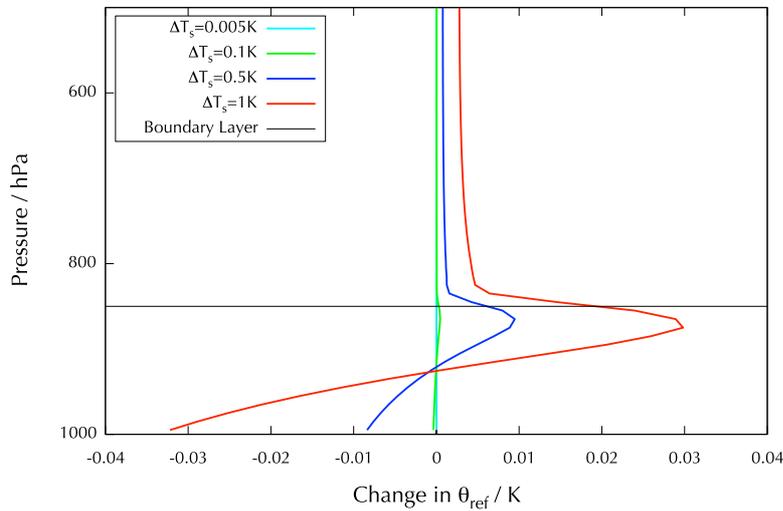
Figure 2.17: *Change in θ_{ref} for various values of ΔT_s. Model parameters as in Figure 2.16. The black line indicates the top of the boundary layer.*
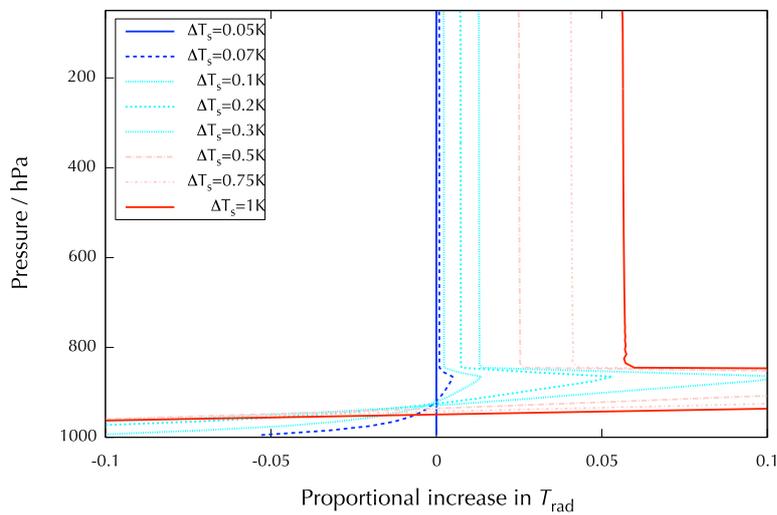
Figure 2.18: *Proportional increase in T_{rad} for increasing ΔT_s. Model parameters as in Figure 2.16.*

2.10 A GUOY-STODOLA PERSPECTIVE ON WORK GENERATED

The Guoy-Stodola equation (Equation 1.7) relates the work done by a system to the work input $\mathscr{F}_{\text{in}}$ and the irreversible entropy production $\dot{S}_i$, given by

$$\dot{S}_i = \frac{\mathscr{F}_{\text{out}}}{T_{\text{out}}} - \frac{\mathscr{F}_{\text{in}}}{T_{\text{in}}} \quad , \tag{2.126}$$

thus:

$$\dot{L} = \eta \mathscr{F}_{\text{in}} - T_{\text{out}} \dot{S}_i \quad , \tag{2.127}$$

where $\eta = (1 - {}^{T_{\text{out}}}/_{T_{\text{in}}})$ is the Carnot efficiency of the system. We are now in a position to investigate how the Carnot efficiency and irreversible entropy production change as we increase from zero the surface temperature difference between two WTG-coupled columns ΔT_s and generate mechanical work. Section 2.9 suggests that the temperature profile in each column i, $T_i(p)$, can be expressed as $T_0(p)$, the temperature profile for a single column above SST T_s at radiative equilibrium, plus a quadratic expression in ΔT_s:

$$T_1(p) = T_0(p) - \alpha(p)\Delta T_s - \beta(p)\Delta T_s^2 \quad , \tag{2.128}$$

$$T_2(p) = T_0(p) + \alpha(p)\Delta T_s - \beta(p)\Delta T_s^2 \quad . \tag{2.129}$$

The coefficients in the quadratic expression $\alpha(p)$ and $\beta(p)$ can be fitted to model results for low values of ΔT_s. $\mathscr{F}_{\text{out,i}}(p)$, the radiation emitted by layer p of column i and leaving the system, can then be estimated by use of the Stefan-Boltzman law and emissivity factors. $\mathscr{F}_{\text{in,i}}(p)$, the radiation (both SW and LW) absorbed by each layer, is similarly largely dependent on the surface temperatures in the two columns.

This framework enables us to start with the system at radiative-convective equilibrium and then incrementally perturb the system until the result of the SCM run is obtained, recalculating the Guoy-Stodola equation after each step. We do so in the following order:

1. The starting point is the radiative equilibrium in two equally-sized columns with no SST

difference between them.

2. The temperature profile in each column is changed to $T_0(p) \pm \alpha(p)\Delta T_s$ and values of the terms of the Guoy-Stodola equation are recalculated on the basis of this temperature profile and the heat fluxes that it implies.

3. The second order temperature term is included, and the terms are recalculated.

4. The final step is to replace the estimated temperature profiles by those obtained from the coupled single column model. As in the previous section, the model keeps the heat input constant, thus slightly reducing T_1, T_2 as ΔT_s increases.

The cumulative effects of introducing each of these steps on the values of the components of the Guoy-Stodola equation are shown in Table 2.1. Model parameters include SST for $\Delta T_s = 0$ of 295 K and ϵ =0.5. The model was run with quadruple precision as some of the changes are small relative to the base values.

	Radiative Equilibrium	+ Linear Term	+ Quadratic Term	+ Discrepancy	= Modelled
T_{in} (K)	267.474848	0.49E-03	-0.55E-03	0.27E-08	267.474789
T_{out} (K)	261.833152	0.16E-03	-0.13E-02	0.15E-09	261.832001
η	0.021092	0.12E-05	0.29E-05	0.93E-11	0.021097
$\eta \mathscr{F}_{\text{in}}$ (Wm^{-2})	10.266813	0.58E-03	0.14E-02	0.14E-07	10.268804
$\dot{S}_i$ (Wm^{-2}K^{-1})	0.039211	0.22E-05	-0.48E-05	-0.17E-08	0.039209
$T_{\text{out}}\dot{S}_i$ (Wm^{-2})	10.266813	0.58E-03	-0.13E-02	-0.45E-06	10.266085
$\dot{L}$ (Wm^{-2})	0.000000	-0.25E-31	0.27E-02	0.47E-06	0.002719

Table 2.1: *Contribution of linear and quadratic temperature terms to components of Guoy-Stodola equation. See text for fuller explanation.*

It will be seen that the final step in this decomposition has a minimal impact on all the terms, indicating that the quadratic expression for the temperature profiles produces a good fit. The linear impacts of increasing ΔT_s cancel in the expression for work done, as expected, and it is only the second order term that contributes to the generation of mechanical work, consistent with the quadratic dependency of $\dot{L}$ on ΔT_s that we have found.

This second order temperature term cools the bottom 75hPa (approximately) of the atmosphere (Figure 2.17), and warms a layer of equivalent size immediately above. As the radiation emitted by a layer has a quartic dependency on its temperature this cooling will reduce $\mathcal{F}_{\text{out}}$ without having an impact on $\mathcal{F}_{\text{in}}$, and so create an energy imbalance which corresponds to the mechanical work generated. It will also reduce T_{out} (which is weighted by $\mathcal{F}_{\text{out}}$) to a greater extent than T_{in}, and thus increase the Carnot efficiency η, but also have a compensating effect on $\dot{S}_i$. However, in addition $\dot{S}_i$ will also decrease by $\dot{L}/T_{\text{out}}$.

This analysis indicates that the linear changes in T_{in} and T_{out} impact the Carnot efficiency and the lost work terms of the Guoy-Stodola equation in a manner that cancels out in total. It is only once the second order radiation term is introduced that the impact on $\mathcal{F}_{\text{out}}$ results in a decrease in the irreversible entropy production and a corresponding increase in the work done.

To some extent the Guoy-Stodola equation is a tautologous restatement of the energy conservation equation; it quite simply reminds us that the work output is equal to the difference between the heat flux input and the heat flux output. What is perhaps more interesting is the insight that changes in the Carnot efficiency in themselves are not sufficient to change the mechanical work output - what matters are changes in the Carnot efficiency that are not balanced by changes in irreversible entropy production. In this particular case, the production of entropy arises from absorption and re-radiation of long and short wave fluxes and hence these two elements will be intimately linked.

2.11 An approximate extension to the moist case

Hitherto the analyses performed have all been limited to dry convection, ignoring the additional heating effect arising from the condensation of upward-advected moisture on the system. In order to gain some insight into the impact of this effect, a simple representation of the main features of this impact was added to the simplified coupled SCM. This approach is

inspired by the Betts-Miller parametrisation (Betts and Miller, 1993) and assumes that the relative humidity in the warm column above the boundary layer is constrained to 100%, with a constant mixing ratio within the boundary layer. Any upward advection of moisture in that column will therefore generate condensation which will give rise to heating. The radiative model previously used is retained; we are merely introducing moisture here to estimate the latent heating effect. The WTG is used to obtain a vertical wind velocity based on the temperature difference between the two columns as before - note that it is the temperature difference between the columns rather than the virtual temperature difference that gives rise to the velocity. This point is considered further in the next chapter.

The profile of the warm (moist) column produced is shown in the tephigram in Figure 2.19. The potential temperature profiles generated and the resulting vertical velocities are shown in Figure 2.20. It will be seen there is significant heating in the warm column centred at approximately 700hPa leading to large upward velocities and an increased potential temperature difference between the columns. Minor numerical convergence problems just below the top of the boundary layer are also apparent.

The generation of mechanical work by a temperature difference between the two columns was analysed (Figure 2.21) and is compared with the work generated by an otherwise comparable dry model. One can note that as $\Delta T_s \rightarrow 0$ self-sustaining moist convection continues to occur, resulting in work done (the $\Delta T_s = 0$ run is initialised with two identical columns, but the model nonetheless converges to a self-sustaining solution). As the model could also permit a solution with no vertical motion, even if it does not converge to that solution, this points to the existence of multiple equilibria. These have been observed in more sophisticated models (see e.g. Sobel et al., 2007; Sessions et al., 2010; Daleu et al., 2015b; Sentić and Sessions, 2017). The latent heat input into the system likewise remains non-zero as the difference between the columns is reduced.

The work done in the moist case is greater than that done in the comparable dry case - this result is at first sight inconsistent with the demonstration in Pauluis (2011) that a moist ener-
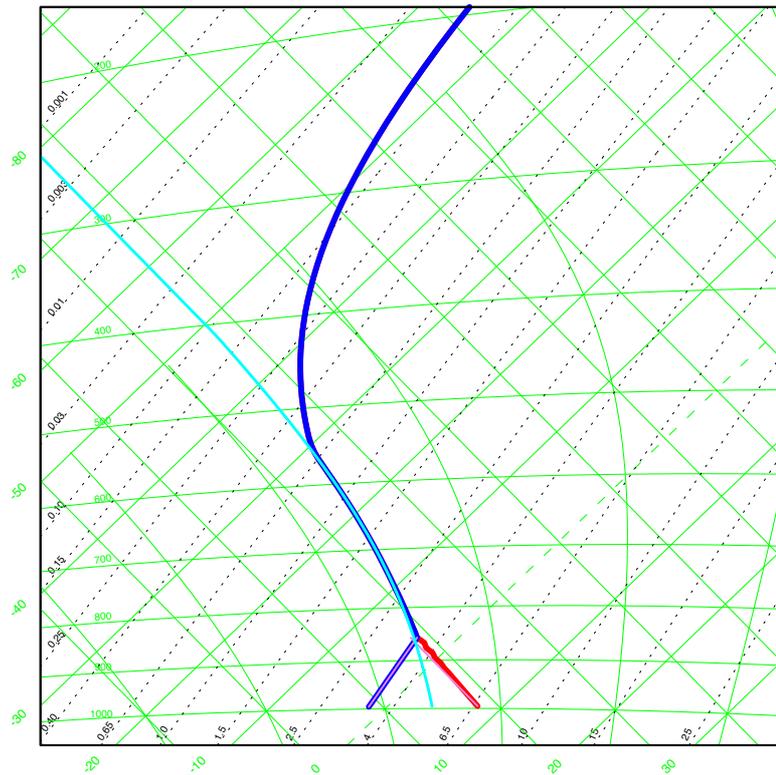
Figure 2.19: *Tephigram for warm column. The red line represents the temperature profile, and the blue line the wet-bulb temperature. The cyan line is a moist adiabat plotted through the LCL. Model parameters include $\epsilon = 0.1$ SST of 295 K and $\tau = 3$ hours.*

(a) θ (b) *LS velocity*
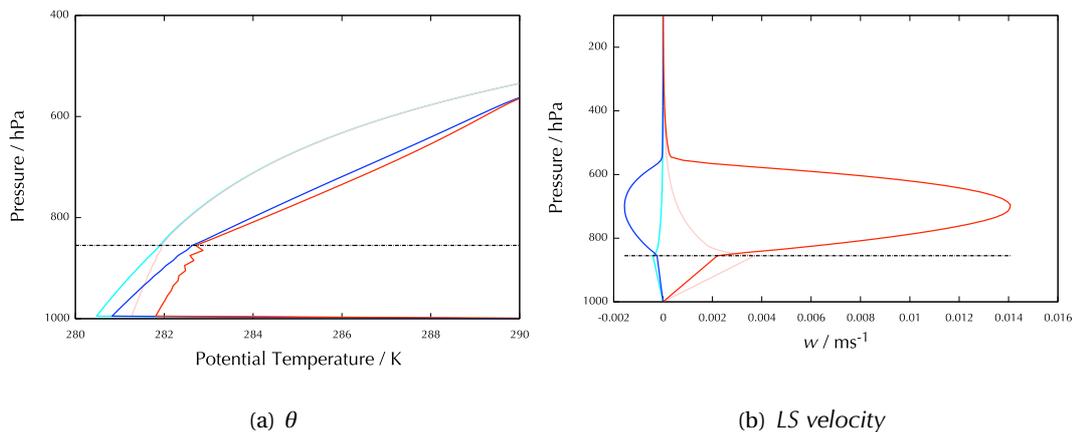
Figure 2.20: *Comparison of equilibrium states for moist (blue, red) and dry (cyan, pink) WTG coupling. Model parameters include $\epsilon = 0.1$, SST of 295 K and 297 K and $\tau = 3$ hours*

getic cycle will be less efficient than a comparable dry cycle. The two results however are not directly comparable. Firstly, Pauluis fixes the temperatures at which energy enters and leaves
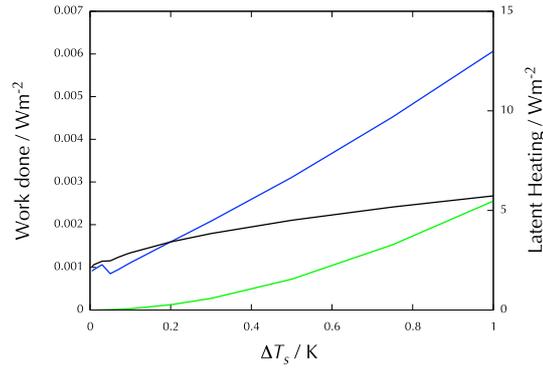
Figure 2.21: *Mechanical work done by moist model (blue) and comparable values for dry model(green) for varying SST differences. The latent heat generated by the system is shown in black (right hand scale). Model parameters include $\epsilon = 0.5$ and SST in the cool column of 295K.*

the system and studies the effect of increasing humidity - in this case it is the SSTs that are fixed and the temperature profiles of the system result from advective and convective processes. In addition, the energy input here includes latent heat in the moist case and not in the dry case.

One can gain some insight into this process of self-sustaining convection following the approach of Equation 2.107. Consider two columns with no SST difference, but where upward convection occurs in one of the columns. One can then write for the warm column:

$$\frac{(1-\epsilon)\theta'}{T_{\text{rad}}} = \frac{L_v}{c_p} \frac{\partial r_v}{\partial z} w \tag{2.130}$$

$$= \frac{L_v}{c_p \tau} \frac{\partial r_v}{\partial z} \frac{\theta'}{\partial \theta_{\text{ref}}/\partial z} \quad , \tag{2.131}$$

where L_v represents the specific enthalpy of vaporization for water and r_v is the mixing ratio for water vapour (determined by the reference temperature profile). Depending on the relationship between θ_{ref}, T_{rad} and τ_{WTG} this equation may permit non-zero solutions for θ' and hence w at some heights. Thus the heating produced by condensation can be compensated exactly by the upward advection of lower entropy air by the WTG velocity.

2.12 COUPLING COLUMNS WITH THE WEAK PRESSURE GRADIENT APPROXIMATION

Although the focus of this thesis is on a large-scale circulation parametrised by the WTG approximation, it is instructive to compare the results obtained with those which arise from an alternative parametrisation, in this case the Weak Pressure Gradient (WPG), otherwise referred to as the Damped Gravity Wave (DGW) approach. Whereas the WTG equation is obtained by assuming that vertical advection eliminates horizontal temperature anomalies, the WPG equations are derived from perturbed equations of motion in order to diagnose the vertical velocity that a particular buoyancy perturbation generates. By expressing the approach in Kuang (2008a) in pressure coordinates we can write the anelastic equations of motion and continuity for perturbations to an equilibrium state as:

$$(\frac{\partial}{\partial t} + \epsilon_{\mathrm{WPG}})\bar{\rho} u' = -\frac{\partial p'}{\partial x} \quad , \tag{2.132}$$

$$\frac{\partial p'}{\partial p} = -\frac{T_v'}{T_{v,\mathrm{ref}}} \quad , \tag{2.133}$$

$$\frac{\partial u'}{\partial x} + \frac{\partial \omega'}{\partial p} = 0 \quad , \tag{2.134}$$

where ϵ_{WPG} is the inverse of the Rayleigh damping timescale τ_{RAY}. By eliminating u' and p' between these equations and then using the gas law we can obtain:

$$(\frac{\partial}{\partial t} + \epsilon_{\mathrm{WPG}}\bar{\rho})\frac{\partial^2 \omega'}{\partial p^2} = -\frac{1}{T_{v,\mathrm{ref}}}\frac{\partial^2 T_v'}{\partial x^2} \quad , \tag{2.135}$$

$$= -\frac{R_d}{p_{\mathrm{ref}}}\frac{\partial^2 T_v'}{\partial x^2} \quad . \tag{2.136}$$

If we look for gravity wave solutions for T_v' with horizontal wavenumber k, with no time dependency, we obtain the following partial differential equation for ω':

$$\epsilon_{\mathrm{WPG}}\frac{\partial^2 \omega'}{\partial p^2} = \frac{k^2 R_d}{\bar{p}_{\mathrm{ref}}}T_v' \quad . \tag{2.137}$$

This elliptical equation can be solved numerically using a triangular solver. The boundary conditions used are that $\omega' = 0$ at the surface and at an assumed tropopause at 100 hPa. Values typically taken for the parameters are $\epsilon_{\mathrm{WPG}} = 1 \text{ day}^{-1}$ for the damping coefficient, and $k = 10^{-6}$

m^{-1} for the wavenumber (Daleu et al., 2015b).

The simplified SCM has been run with WPG coupling for a dry case. The temperature difference between the two converged columns and the large scale velocity diagnosed are shown in Figure 2.22, with analagous values for a WTG-coupled system with $\tau_{\mathrm{WTG}} = 3$hrs. It will be seen that the values produced in both graphs are similar in the lower boundary layer, but that the temperature difference between the columns reduces more gradually for the WPG results than for those obtained from the WTG approximation, in particular persisting beyond the boundary layer. (It should be noted, of course, that there is no explicit notion of a boundary layer in the WPG approximation.) The velocities produced by this WPG implementation are very much smoother than the WTG velocities, reaching a smaller maximum value around the top of the boundary layer and then reducing much more gradually. These results are not consistent with the observation that WTG velocities are more top-heavy than WPG velocities noted in section 1.5 — this will at least in part be due to the fact that the WTG approximation more directly reflects local heating anomalies and that this is a dry model with very little heating in the upper troposphere.

(a) θ' (b) *LS velocity*
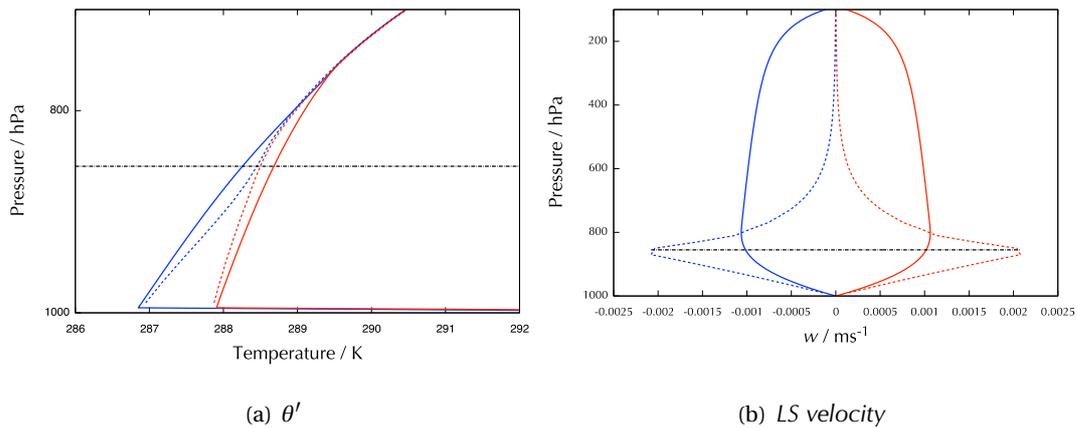
Figure 2.22: *Comparison of equilibrium states between WPG (solid) and WTG (dashed) coupling. Model parameters include $\epsilon = 0.5$, SSTs of 298 K and 300 K.*

As the velocities produced by the two models are broadly similar at the heights where the temperature difference between the columns is significant, and those temperature differences are also broadly similar, one might expect the work done generated by the two models to be com-

parable. This is in fact the case, as shown in Figure 2.23, which also shows that as with the WTG approximation the work done for WPG coupling has a quadratic dependency on the surface temperature difference between the two columns.
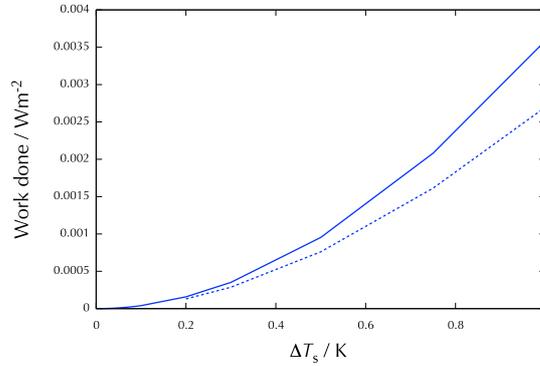
Figure 2.23: *Work done by WPG coupled system - sensitivity to SST difference between columns. Comparable results for the WTG are shown by a dashed line. The parameters used are as above.*

The sensitivity of the results, particularly the generation of mechanical work, to the WPG parameter was investigated. Although there are two parameters, they only appear in Equation 2.137 as k^2/ϵ, so it is sufficient to consider multiples of this parameter - in fact to facilitate comparison with the WTG results, sensitivities are described by a "Coupling" timescale coefficient which divides ϵ, (i.e. multiplies τ_{RAY}), so that a coupling coefficient of 0 corresponds to very strong coupling and infinity corresponds to no coupling between the columns. Results for the resulting APE and generation of mechanical work in Figure 2.24.

The APE decreases for stronger coupling, as would be expected, although there is no plateau as seen in the WTG results (see Figure 2.14), and the values for a coupling parameter of 1 are higher than those for $\tau_{\mathrm{WTG}} = 3$ hours, consistent with the fact that temperature differences persist at higher altitudes. The generation of mechanical energy reaches a maximum close to the point where the coupling parameter is 1.

By analogy with the result obtained for the WTG approximation (Equation 2.38), we can consider an implied relaxation time ($\dot{L}/2\bar{A}$). A plot of this against the coupling timescale coef-

(a) *APE* (b) *Generation of mechanical work*
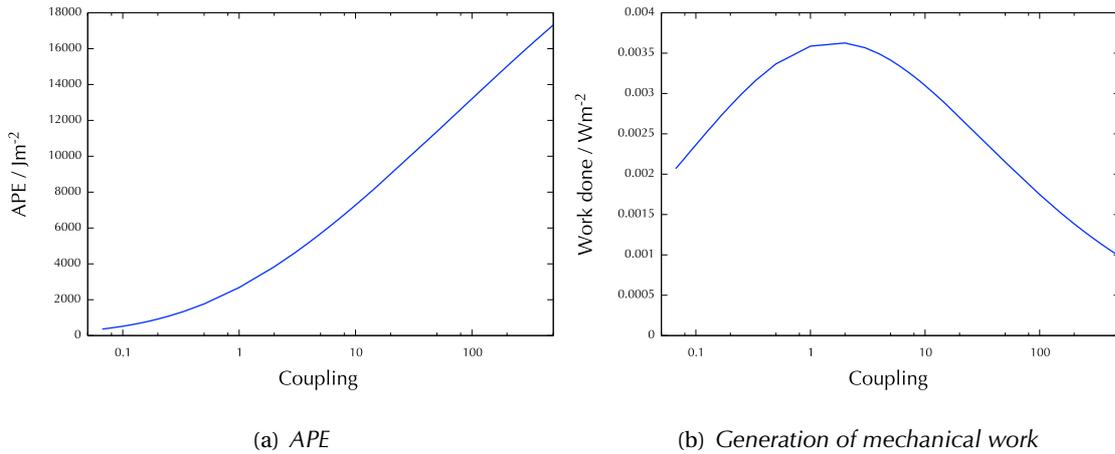
Figure 2.24: *APE and Work done for WPG coupled system - sensitivity to coupling strength (where 0 represents very strong coupling). Other parameters as above.*

ficient (FIgure 2.25) on a log log scale is very close to a line of slope 0.5, implying that $\bar{A}/\dot{L} \sim \sqrt{\epsilon}/k$. This can be interpreted as implying that the timescale is proportional to the length scale of the system for a given damping coefficient (c.f. the argument in section 2.7).
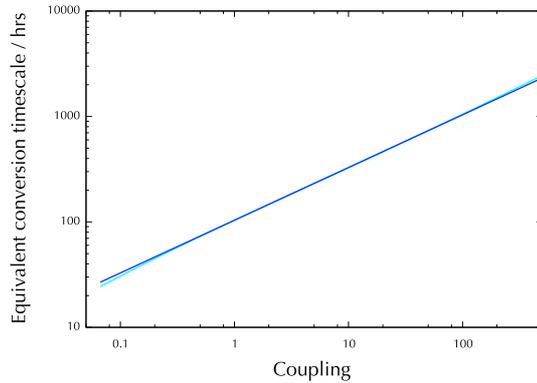
Figure 2.25: *Effective timescale for conversion of APE to kinetic energy for WPG-coupled columns (blue). A line of slope 0.5 is shown in cyan.*

2.13 CONCLUSION

In this chapter we investigated the generation of mechanical work by an overturning circulation using a simple SCM. The model was first presented, and then some difficulties which arise when a model such as this is used to calculate APE are discussed. The model was also used to explore the MEP conjecture as described in the Appendix, confirming results previously pub-

lished that show that this can be used can predict lapse rates in the lower atmosphere.

The WTG approximation was introduced as a coupling mechanism between two columns and the impact that this has on temperature profiles and the associated vertical winds is shown. Approximate analytical expressions for the energy pathways are developed, including the key result that the conversion from APE $\bar{A}$ to kinetic energy by a WTG-driven circulation with timescale parameter τ is given by $2\bar{A}/\tau$. Expressions for the vertical and horizontal kinetic energy were developed for a number of different geometrical configurations, and it is shown that in order for commonly used values of the τ parameter and the Rayleigh damping parameter to be consistent, the introduction of radial winds in a three-dimensional structure is necessary. It is also shown that this approach can be extended to identify latitude-dependent constraints on the size of self-aggregating convective systems.

A simple expression for how Weak Temperature Gradient coupling reduces the temperature difference between two columns is developed, and this is used to confirm model values for the coupling timescale dependency for the generation of mechanical work by the system. This same expression underpins an analytical result for the work generated as a quadratic function of the SST difference between the two columns. The mechanical work generated by this coupling is balanced by reduced radiation emitted by the system, due to cooling in the lower atmosphere. This analysis is used to explore how changes in the Carnot efficiency arising from such cooling and the generation of irreversible entropy interact to produce mechanical work.

A simple extension to a moist case is explored, which identifies the potential for multiple equilibria that have been seen elsewhere. Finally, the WTG coupling mechanism is replaced with the WPG for the dry case and we see that the velocity profiles and temperature differences are smoother, but that the generation of mechanical work exhibits largely similar features to that under the WTG.

CHAPTER 3

A MECHANICAL ENERGY BUDGET FOR COUPLED CLOUD RESOLVING MODELS

3.1 INTRODUCTION

The previous chapter explored the energetic pathways resulting from two columns coupled by a large-scale circulation in a highly idealised context. We focused particularly on the generation of mechanical work, deriving expressions linking this generation to the Available Potential Energy in the system. We now return to this same general question in a more realistic context, using two coupled cloud resolving models that were developed previously for studies of transitions from suppressed to active convection (Daleu et al., 2015a) in order to assess the relevance of the results of the previous chapter are in a more complex context. We use these models to represent separate regions, over surfaces with different SSTs, but linked by a parametrised large-scale circulation. In order to identify the work generated, we make use of an isentropic diagnostic framework introduced in Pauluis (2016) that permits the expression of a mechanical energy budget for a convective system. It relates the Carnot maximum work done for the system to the sum of the kinetic energy generated, the work done in lifting water and a component representing lost work associated with the irreversible production of entropy through evaporation. As we are working with two separate regions and are particularly interested in the overturning circulation between them we will need to modify and extend this diagnostic approach.

We first present the cloud resolving model that we are using and discuss the results that it produces for a single region at radiative convective equilibrium. We show how the Pauluis diagnostic methodology can be improved in the case of an anelastic model such as that used here, and that its extension to two coupled regions requires us to introduce a further refinement. We next present results for the mechanical energy budget for varying strengths of WTG coupling, for varying SST differences between the regions and for varying sizes of the two regions; scaling arguments explaining many of these results are then developed. The energy balance of the system and the kinetic energy associated with it are analysed. We also apply this diagnostic approach to Weak Pressure Gradient coupling and examine a number of other sensitivities. Finally, we replace the parametrised coupling by a model which explicitly includes both regions side by side in one domain.

Much of the work discussed in this chapter has been published in Kamieniecki et al. (2018), together with some material from the previous chapter.

3.2 Overview of Large Eddy Model used

Cloud Resolving Models (CRMs) provide a powerful tool to study the details of convection. A grid-length is chosen that can filter the main variables into (explicitly modelled) large and (parametrised) subgrid scale components, essentially cloud microphysics, radiation and subgrid scale turbulence. This project follows on from projects which have used the Met Office's Large Eddy Model (hereafter called the LEM) in CRM mode to analyse the effect of coupling two regions by a large-scale circulation and so has built on the configuration previously developed (Daleu et al., 2012; Daleu, 2013; Daleu et al., 2015a)

This section provides an overview of the features of the LEM (version 2.4) used to provide the runs which underly the results in this chapter. The underlying structure of the LEM is described in Gray et al. (2004) and the particular configuration used is set out in more detail in Daleu (2013).

The LEM is used in a two dimensional configuration, of width 128 km (with 500 m grid spacing) along the x axis and 60 vertical levels on a stretched grid (providing finer resolution near the surface) and extending up to 20 km, with periodic lateral boundary conditions. A Lorenz grid is applied in the vertical and an Arakawa C-grid in the horizontal. Both the top and bottom of the model are rigid lids, with Newtonian damping at the highest levels to eliminate gravity wave perturbations. Horizontal wind along the x axis is relaxed to zero with a time-scale of 2 hours to avoid propagation of convective cells (see Tompkins, 2000; Mapes and Wu, 2001) and the development of artificial wind-shear, and is a constant 5 m s^{-1} along the y axis to enhance surface fluxes and reduce the impact of fluctuations in wind speed. The lower boundary is an ocean with a base SST of 302.7 K. The model is run until a stable equilibrium emerges (see section 3.3).

The LEM works with a non-hydrosatic Boussinesq set of equations, expressed as perturbations about a reference state that is defined for dry air in hydrostatic equilibrium:

$$\frac{Du_i}{Dt} = -\frac{\partial}{\partial x_i}\left(\frac{p'}{\rho_{\text{ref}}}\right) + \delta_{i3}B + \frac{1}{\rho_{\text{ref}}}\frac{\partial \tau_{ij}}{\partial x_j} - 2\epsilon_{ijk}\Omega_j u_k \tag{3.1}$$

$$\frac{\partial}{\partial x_i}(\rho_{\text{ref}}u_i) = 0 \tag{3.2}$$

$$\frac{D\theta}{Dt} = \frac{1}{\rho_{\text{ref}}}\frac{\partial h_3^\theta}{\partial z} + \left(\frac{\partial \theta'}{\partial t}\right)_{\text{mphys}} + \left(\frac{\partial \theta'}{\partial t}\right)_{\text{rad}} \tag{3.3}$$

$$\frac{Dr_w}{Dt} = \frac{1}{\rho_{\text{ref}}}\frac{\partial h_i^{r_w}}{\partial x_i} + \left(\frac{\partial r_w}{\partial t}\right)_{\text{mphys}} \tag{3.4}$$

$$\frac{D\theta'}{Dt} + w\frac{d\theta_{\text{ref}}}{dz} = \frac{1}{\rho_{\text{ref}}}\frac{\partial h_i^{\theta'}}{\partial x_i} + \frac{1}{\rho_{\text{ref}}}\frac{\partial h_3^{\theta_{\text{ref}}}}{\partial z} + \left(\frac{\partial \theta'}{\partial t}\right)_{\text{mphys}} + \left(\frac{\partial \theta'}{\partial t}\right)_{\text{rad}} \tag{3.5}$$

$$B = g\theta'_v/\theta_{\text{ref}} \tag{3.6}$$

$$\theta'_v = \theta' + \sum_{w=v,l,i} \theta_{\text{ref}}c_w r_w \tag{3.7}$$

$$c_v = 0.608 \tag{3.8}$$

$$c_l, c_i = -1 \tag{3.9}$$

Here δ_{ij} is the Kronecker delta function, τ_{ij} is the turbulent stress tensor, ϵ_{ijk} is the three-dimensional Levi-Civita pseudo-tensor, Ω_j represents the Earth's rotation, h are various sub-grid scalar fluxes, and the subscripts $_{\text{mphys}}$, $_{\text{rad}}$ represent terms due to the microphysics and

radiation. Other symbols have their usual meteorological meanings. The model allows for water vapour and five species of hydrometeor, of which cloud liquid water and cloud ice are of particular interest in the analyses that follow. τ_{ij} is parametrised using a modified first-order Smagorinksy-Lilly approach, where viscosity depends on a local Richardson number and the mixing length λ depends on surface roughness z_0 and the basic mixing length λ_0:

$$\frac{1}{\lambda^2} = \frac{1}{\lambda_0^2} + \frac{1}{[k(z+z_0)]^2} \quad , \tag{3.10}$$

where k is the von Karman constant and z is the height. For consistency with previous studies, a basic mixing length λ_0 of 250 m was used for the majority of the runs, but the impact of this choice is investigated in section 3.16 below. Bulk aerodynamic formulae are used to provide the heat fluxes from the surface. Cloud microphysics are represented by a three-phase parametrisation. In order to avoid introducing complexities due to interactive radiation, fixed cooling of 1.5 K day^{-1} from the surface to 220 hPa, then reducing linearly to 0 at 120 hPa and above was adopted (in this respect the CRM set-up is less realistic than the interactive radiation in the previous chapter). The centred-difference scheme suggested in Piacsek and Williams (1970) is used to advect momentum, and scalars are advected using a total variance diminishing scheme proposed by Leonard et al. (1993), known as ULTIMATE. The timestep is constrained to reflect the CFL criterion and to ensure stability of the mixing.

3.3 CONVERGENCE OF RUNS

The LEM was run for 120 days, with the first 20 days discarded to avoid spin-up features distorting the results. Results for the subsequent 100 days were stored every 30 minutes, giving 4,800 data points in total. A number of indicators were analysed to confirm that the runs had converged and there was no drift - such indicators for a single region run with no coupling (referred to as the uncoupled control run) over an SST of 302.7 K are shown in Figure 3.1. Similar indicators were studied for a number of the other runs, although not exhaustively.

The indicators show a good degree of convergence for the model. There is clearly evidence of random fluctuations in the three time-series plots, but there is no overall trend. The plot of the

(a) θ_e for successive dekads in last 100 days of 120 day run

(b) Latent Heat (24 hour rolling average)

(c) Precipitation (24 hour rolling average)

(d) Resolved Kinetic Energy (24 hour rolling average)
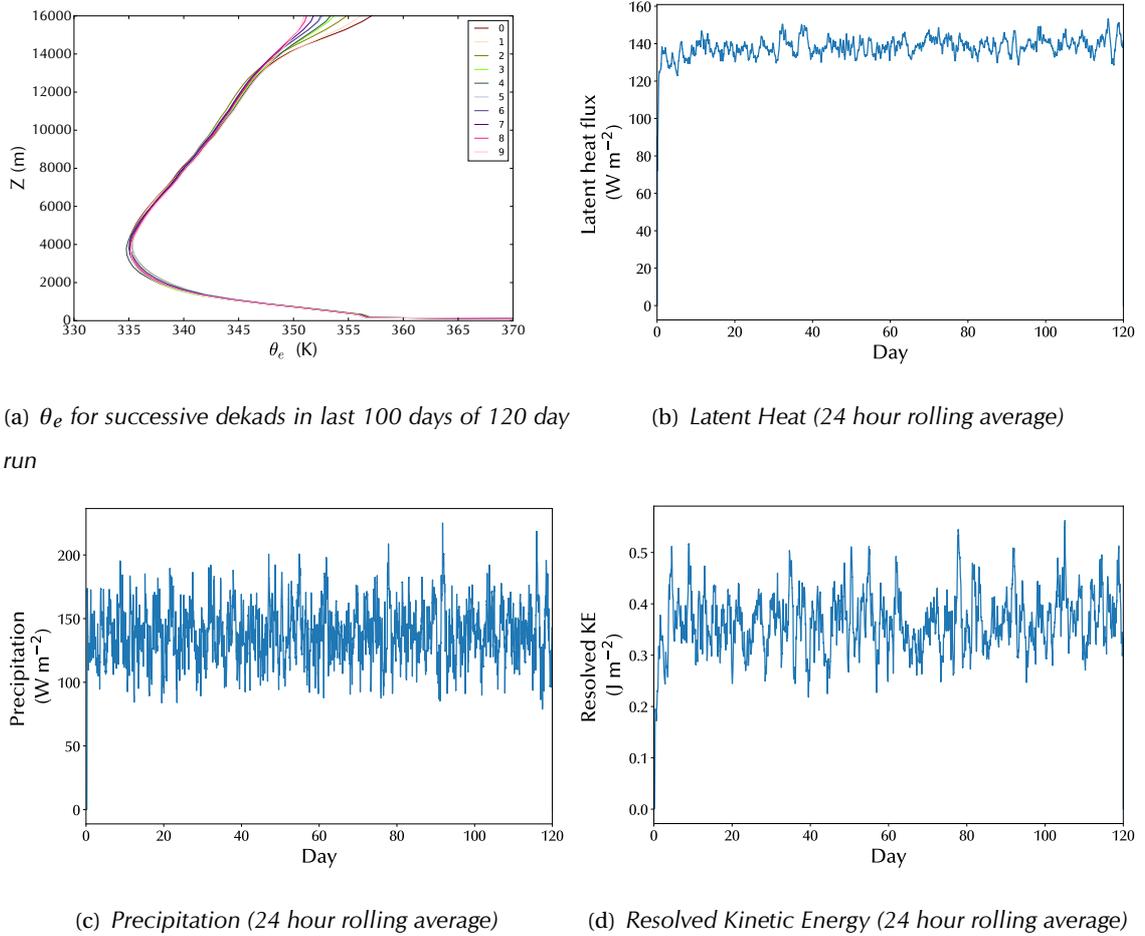
Figure 3.1: *Convergence tests for uncoupled control run. Note that although precipitation (panel c) exhibits greater variability than latent heat input (panel b), the long term averages broadly correspond, indicating that a moisture equilibrium has been reached.*

average values of θ for successive 10 day periods (Figure 3.1(a)) indicates good convergence below 14 km, but a consistent upward drift in the values of θ_e above that as a result of the fixed cooling radiation model which decreases between 220 hPa (approximately 12 km) and 120 hPa (approximately 15.5 km) and is zero above that. As the features analysed in this section all occur below 14 km (see e.g. Figure 3.6), the convergence overall was considered suitable.

3.4 Isentropic analysis of state variables for a single column

Although this chapter focuses on the results produced by two coupled regions, it is instructive to first compare the results produced by the Cloud Resolving Model run in an uncoupled configuration run to Radiative-Convective Equilibrium with those from a run of the System for Atmospheric Modelling published in Pauluis and Mrowiec (2013) (abbreviated as PM13). PM13 introduces the notion of isentropic slices as the intersection of a surface of constant height with an isentrope, and derives a probability distribution function for the equivalent potential temperature of air parcels at a given height level. Likewise, conditional averages of various observed variables in (θ_e, z) space can be obtained, for example if $\langle f \rangle (z, \theta_{e0})$, the isentropic distribution of f, is given by:

$$\langle f \rangle (z, \theta_{e0}) = \frac{1}{PL_x} \int_0^P \int_0^{L_x} f(x, z, t) \delta(\theta_{e0} - \theta_e(x, z, t)) \mathrm{d}x \mathrm{d}t \quad , \tag{3.11}$$

where P is the time period over which averaging is performed and L_X the horizontal range of the model. Then the conditional average of temperature $\tilde{T}(z, \theta_e)$ can be derived as:

$$\tilde{T}(z, \theta_e) = \frac{\langle \rho T \rangle (z, \theta_e)}{\langle \rho \rangle (z, \theta_e)} \quad . \tag{3.12}$$

A vertical mass flux distribution in (θ_e, z) is similarly calculated, which in turn can be used to define a convective streamfunction Ψ:

$$\Psi(z, \theta_e) = \int_0^{\theta_e} \langle \rho w \rangle (z, \theta_e') \mathrm{d}\theta_e' \quad . \tag{3.13}$$

Figure 3.2 shows results obtained from the uncoupled control run, run to equilibrium (see Sections 3.3 and 3.7). For the purposes of this plot the mass flux and stream function have been smoothed using spline interpolation with a zoom factor of 2. Results from PM13 are shown in Figures 3.3-3.5.
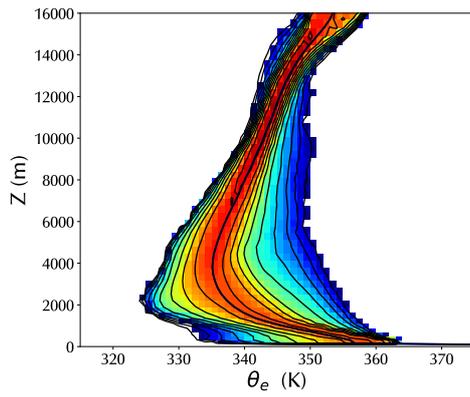
(a) log_{10} of mass density function in (θ_e, z) space normalised at each height level
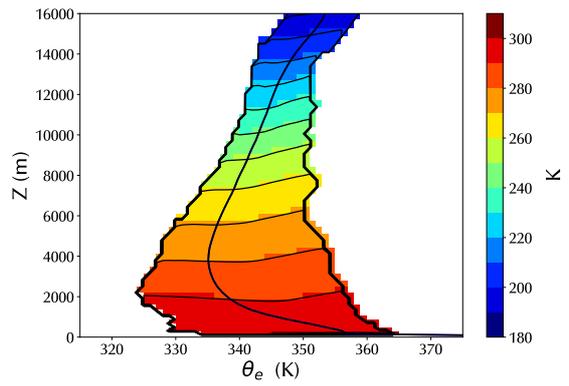
(b) Conditional average of temperature
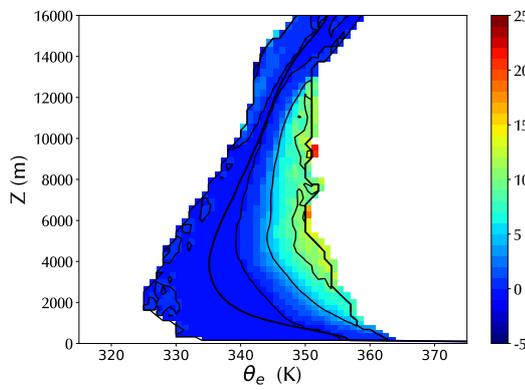
(c) Conditional average of vertical velocity
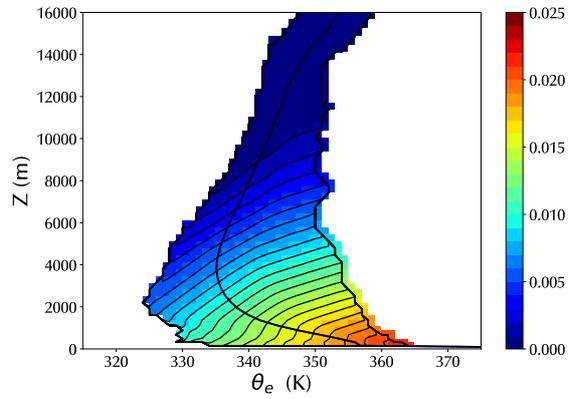
(d) Conditional average of water vapour mixing ratio
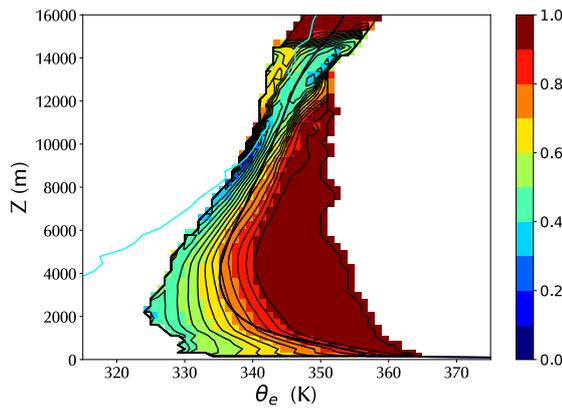
(e) Conditional average of relative humidity (cyan line represents RH = 0)
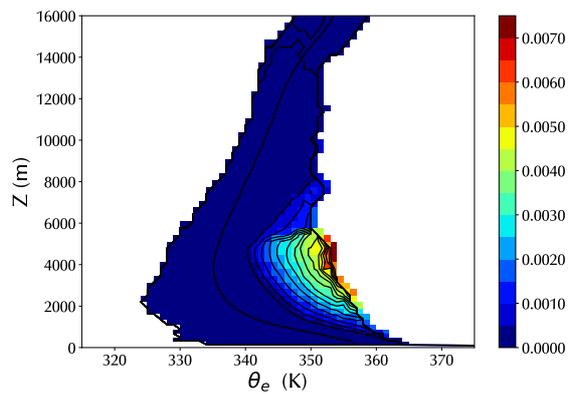
(f) Conditional average of liquid mixing ratio

(g) *Conditional average of Ice mixing ratio*

(h) *Conditional average of buoyancy (dashed line represents 0)*

(i) *Vertical mass flux**

(j) *Streamfunction**
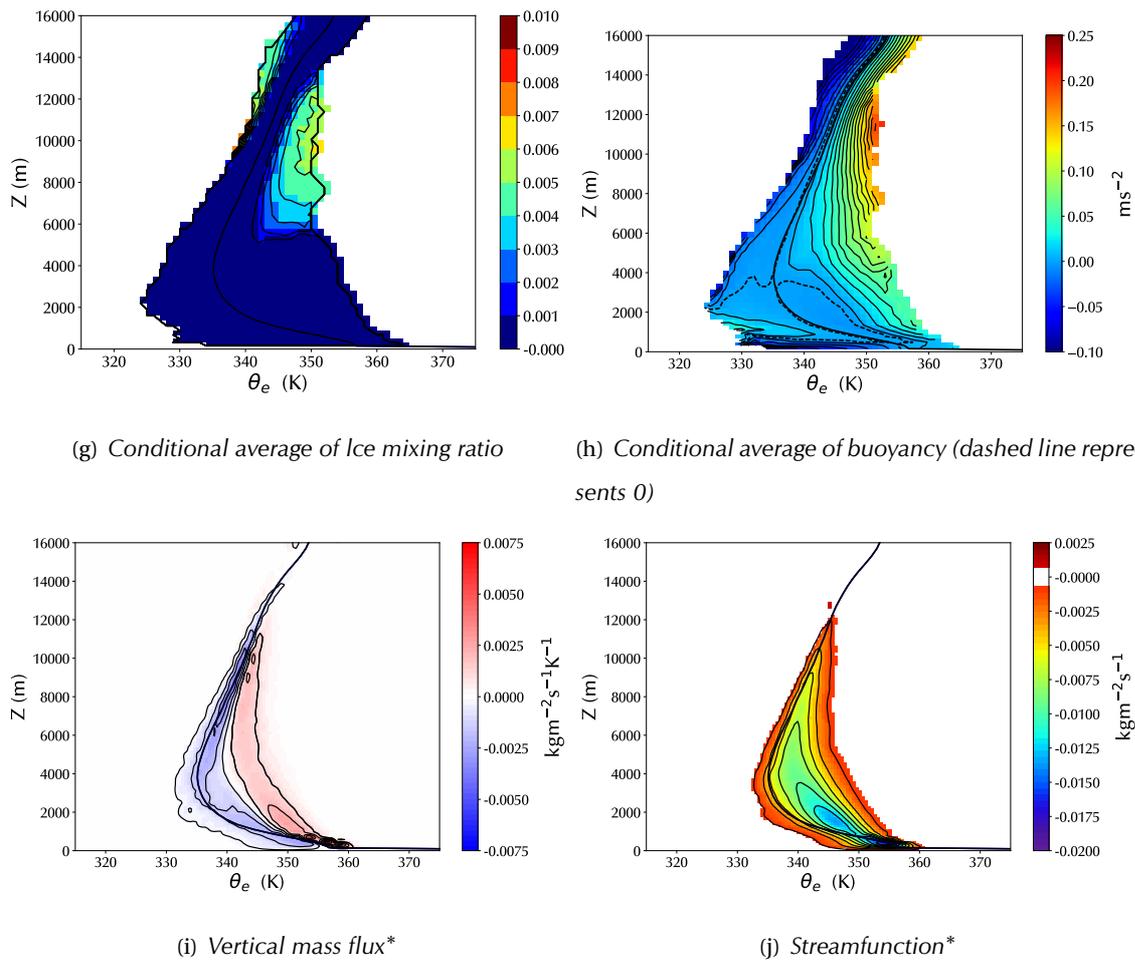
Figure 3.2: *Isentropic analyses for single column with SST 302.7 K (* indicates smoothing has been applied). Solid black line indicates mean θ_e at each height.*
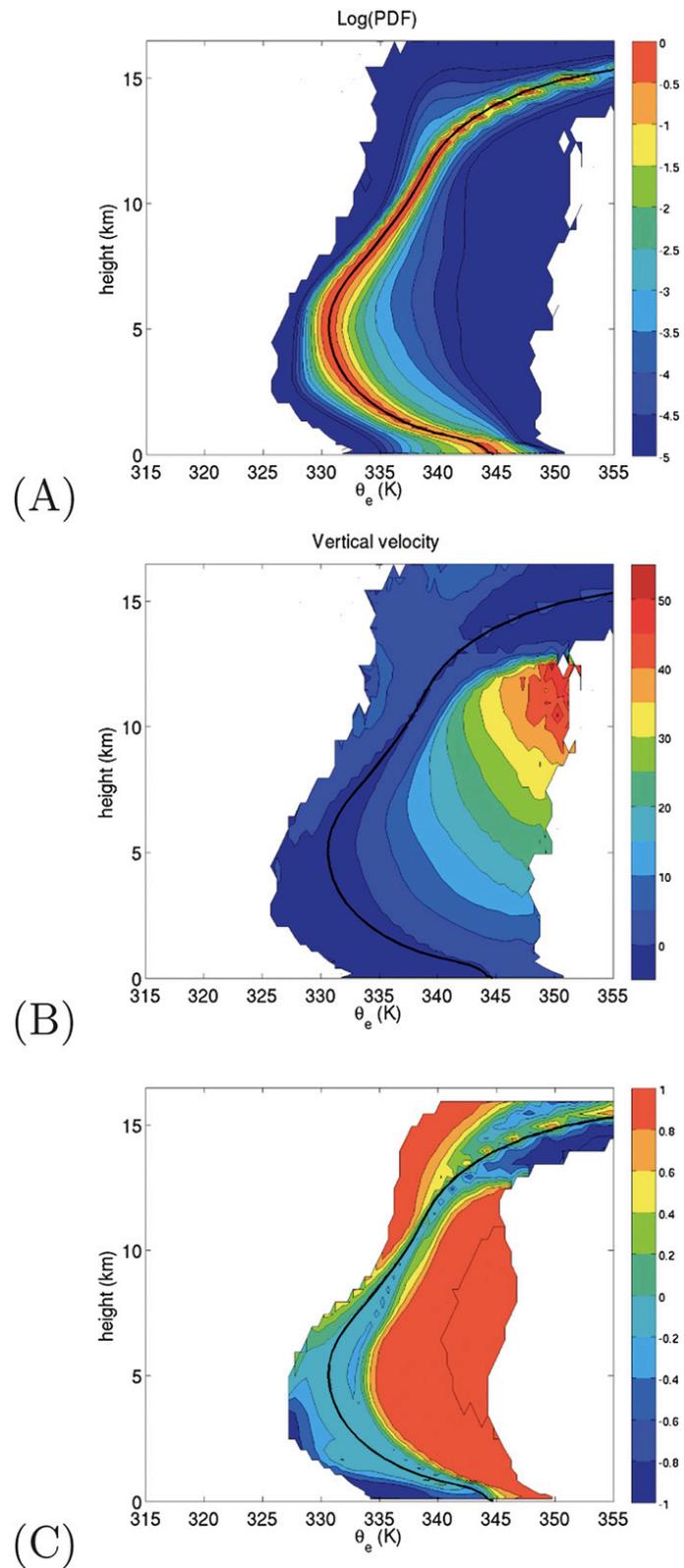
Figure 3.3: *Figure 2 from PM13 - (A) and (B) can be compared with Figures 3.2(a) and 3.2(c) respectively; (C) is a directionality index defined in PM13.(©2013 AMS)*
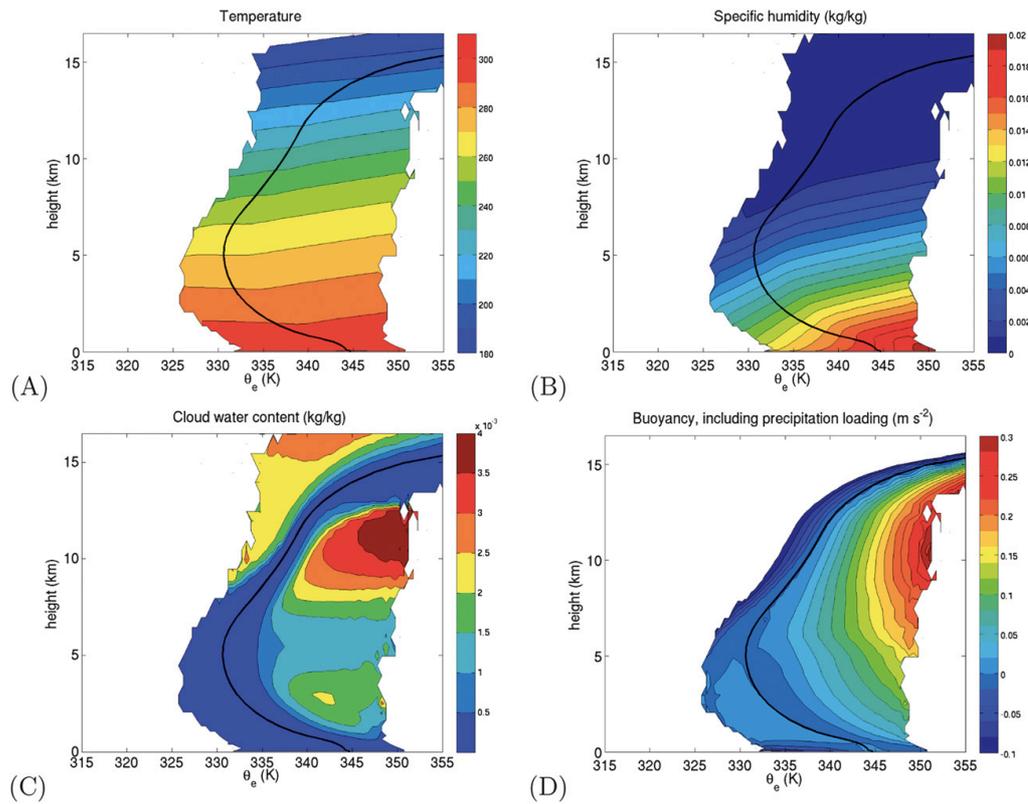
Figure 3.4: *Figure 3 from PM13 - can be compared with Figures 3.2(b), 3.2(d), 3.2(f) and 3.2(g) combined and 3.2(h) above. (©2013 AMS)*
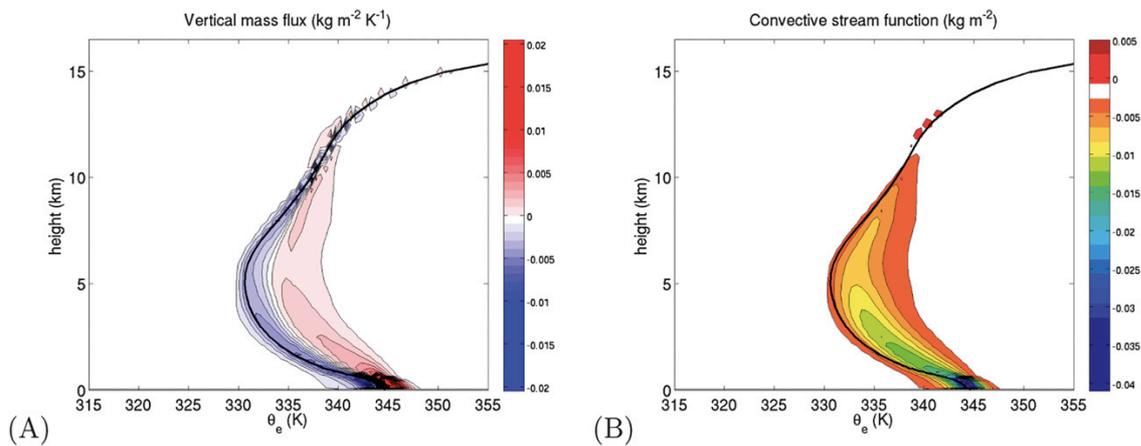
Figure 3.5: *Figure 1 from PM13 - can be compared with Figures 3.2(i) and 3.2(j) above.(©2013 AMS)*

Whilst there are strong similarities between the two sets of results, analysis reveals a number of noteworthy differences:

1. These results show fewer extreme values of θ_e than those in PM13. The LEM is run in

a two-dimensional configuration with 256 horizontal gridpoints, as compared with a 3-dimensional configuration for SAM, with 432 gridpoints in each horizontal dimension. This greater number of gridpoints could explain why the spread of results in SAM is greater, although the temporal frequency of sampling in PM13 has not been specified.

2. The values of θ_e shown here are in general higher than those in PM13. This is in part because the Sea Surface Temperature (SST) here is 302.7 K, as compared with 301 K in PM13, compounded by the resulting higher humidity here as seen in Figure 3.2 d). Another factor will be the definition of θ_e used here, as discussed in Section 1.3, whereas PM13 uses the Emanuel definition including the $(c_p + r_T c_l)$ factor.

3. PM13 exhibits a small number of much more powerful bursts of convection, as evidenced by both the vertical velocity and ice mixing ratio at high entropy, which exceeds that shown here. This again may be a consequence of the more extensive horizontal grid giving rise to more observations, some of which will be more extreme.

On the other hand, the vertical mass flux and streamfunction plots, which are central to the methodology developed in this chapter, appear very similar for the two sets of output.

3.5 MECHANICAL ENERGY BUDGET

The methodology used in this chapter is based on the Mean Air Flow as Lagrangian Dynamics Approximation (MAFALDA) approach introduced by Pauluis (2016). In that paper, convective streamfunctions Ψ in (θ_e, z) space are derived from the vertical mass flux as in Equation 3.13, averaged over a suitable period. The system is represented by trajectories along equally spaced contours in that space (it will later be seen that a surface integral approach is also possible). Pauluis relates changes in entropy along a trajectory to changes in other system variables, allowing for changes of composition through the Gibbs free energy of the various states of water, thus:

$$T\mathrm{d}s = \mathrm{d}h - \alpha_d \mathrm{d}p - \sum_{w=v,l,i} \mathcal{G}_w \mathrm{d}r_w \qquad (3.14)$$

where α_d is the specific volume per unit mass of dry air. For an entire cycle, the change in enthalpy $\oint dh$ vanishes and one is left with:

$$\oint T ds = -\oint \alpha_d dp - \sum_{w=v,l,i} \oint \mathcal{G}_w dr_w \tag{3.15}$$

The integrand in the first term on the right hand side can then be expanded thus:

$$\alpha_d = \frac{R_d T + r_v R_v T}{p} \tag{3.16}$$

$$\approx \frac{R_d T_{\text{ref}}}{p} \left(1 + \frac{T' + r_v(\frac{R_v}{R_d}) T_{\text{ref}} - r_T T_{\text{ref}}}{T_{\text{ref}}} + r_T \right) \tag{3.17}$$

$$= \frac{R_d T_{\text{ref}}}{p} \left(1 + \frac{B}{g} + r_T \right) \quad , \tag{3.18}$$

using the definition of B in Equation 3.6 and ignoring expressions that are second order in the mixing ratio or buoyancy. The pressure p can be expressed as the sum of three components $p = p_{\text{ref}} + p' + e$, where e is vapour pressure. If the second two terms in this expression for p are neglected (the impact of including e will be revisited later), the first term on the right hand side of Equation 3.18 will integrate to zero over a closed trajectory. This step uses the hydrostatic approximation in the form $dp_{\text{ref}} = -g\rho_{\text{ref}} dz$, where ρ_{ref} is the pressure of dry air in the reference state and the ideal gas law:

$$-\oint \frac{R_d T_{\text{ref}}}{p} dp \approx \oint \frac{g \rho_{\text{ref}}}{\rho_{\text{ref}}} dz \quad = 0 \quad . \tag{3.19}$$

Likewise, one can then approximate the contour integrals of the second and third terms on the right hand side of Equation 3.18:

$$-\oint \frac{R_d T_{\text{ref}} B}{g p} dp \approx -\oint \frac{R_d T_{\text{ref}} B}{g p_{\text{ref}}} dp_{\text{ref}} = \oint B dz \tag{3.20}$$

$$-\oint \frac{R_d T_{\text{ref}} r_T}{p} dp \approx \oint g r_T dz \quad . \tag{3.21}$$

Pauluis summarises these relationships as follows:

$$W_{\mathrm{max}} = W_b + W_p + \Delta\mathcal{G} \quad , \text{ where} \tag{3.22}$$

$$W_{\mathrm{max}} = \oint T \mathrm{d}s \tag{3.23}$$

$$W_b = \oint B \mathrm{d}z \tag{3.24}$$

$$W_p = \oint g r_T \mathrm{d}z \tag{3.25}$$

$$\Delta\mathcal{G} = \sum_{w=v,l,i} \oint -\mathcal{G}_w \mathrm{d}r_w \tag{3.26}$$

The interpretation of these relationships is that the maximum work that the system can generate (W_{max}) is equal to the sum of what Pauluis refers to as the "Gibbs penalty " ($\Delta\mathcal{G}$, which represents the energetic implications of evaporating water at lower relative humidity than that at which it condenses over a cycle - see Pauluis (2011) for a fuller discussion), the buoyancy work done (W_b) and the work done in lifting water vapour (W_p). W_b corresponds to the work done analysed in Chapter 2 of this thesis, and W_p will in turn be converted into the kinetic energy of precipitation, some of which will be dissipated as the hydrometeors descend through the atmosphere (Pauluis and Dias, 2012; Igel and Igel, 2018) and some at the surface.

Although Pauluis is clear that it is $W_{\mathrm{in}} = W_{\mathrm{max}} - \Delta\mathcal{G}$ that is the heat input into the system, the form of the equation above encourages readers to believe that W_{max} represents some limit on the work done. To avoid such confusion an alternative notation W_{Tds} is used instead of W_{max} and the equation is written as:

$$W_{\mathrm{in}} = W_{Tds} - \Delta\mathcal{G} \tag{3.27}$$

$$= W_b + W_p \tag{3.28}$$

When applied to results from the LEM this equation generates numerical results which do not balance (indeed similar features are observed in Pauluis (2016)). The original derivation of Equation 3.22 involves the use of the hydrostatic approximation $\mathrm{d}p = -\rho_{\mathrm{ref}} g \mathrm{d}z$ in evaluating $-\alpha_d \mathrm{d}p$, where ρ_{ref} is the density of dry air in the reference profile and α_d is the specific volume of dry air. In an anelastic model such as the LEM, this need not hold in general, but it

does hold for the reference profile, where it relates the partial pressure of dry air p_{ref} to height: $dp_{\text{ref}} = -\rho_{\text{ref}} g dz$. The contour integral of the first term on the right hand side of Equation 3.18 is zero for an anelastic model if the full hydrostatic approximation is used as in Pauluis (2016). Applying instead the hydrostatic approximation for dry air, it can be simplified with the assumption that the reference profile is close to the equilibrium state and that variations in the pressure of dry air at a given height are insignificant when compared with variations in water vapour pressure, (ie $p \approx p_{\text{ref}} + e$) and ignoring higher orders of $\frac{e}{p_{\text{ref}}}$ to obtain an additional term:

$$-\oint \frac{R_d T_{\text{ref}}}{p} dp = -\oint \frac{R_d T_{\text{ref}}}{p_{\text{ref}} + e} d(p_{\text{ref}} + e) \tag{3.29}$$

$$\approx -\oint \frac{R_d T_{\text{ref}}}{p_{\text{ref}}} dp_{\text{ref}} + \oint \frac{e R_d T_{\text{ref}}}{p_{\text{ref}}^2} dp_{\text{ref}} - \oint \frac{R_d T_{\text{ref}}}{p_{\text{ref}}} de \quad . \tag{3.30}$$

Making use of the gas law:

$$-\oint \frac{R_d T_{\text{ref}}}{p} dp \approx -\oint \frac{1}{\rho_{\text{ref}}} dp_{\text{ref}} + \oint \frac{e R_d T_{\text{ref}}}{p_{\text{ref}}^2} dp_{\text{ref}} - \oint \frac{R_d T_{\text{ref}}}{p_{\text{ref}}} de \quad . \tag{3.31}$$

Using the hydrostatic approximation, and remembering that to first order $e = r_v \frac{R_v}{R_d} p_{\text{ref}}$:

$$-\oint \frac{R_d T_{\text{ref}}}{p} dp \approx \oint g dz + \oint \frac{r_v R_v T_{\text{ref}}}{p_{\text{ref}}} dp_{\text{ref}} - \oint \frac{r_v R_v T_{\text{ref}}}{p_{\text{ref}}} dp_{\text{ref}} - \oint R_v T_{\text{ref}} \frac{dr_v}{dp_{\text{ref}}} dp_{\text{ref}} \quad . \tag{3.32}$$

The first of the terms on the right hand side is zero, and the second and third cancel, leaving the final term, which can be expressed as an integral in r_v:

$$-\oint \frac{R_d T_{\text{ref}}}{p} dp \approx -\oint R_v T_{\text{ref}} dr_v \quad . \tag{3.33}$$

This expression can be integrated by parts and then expressed in terms of an integral in z:

$$-\oint \frac{R_d T_{\text{ref}}}{p} dp \approx +\oint R_v r_v dT_{\text{ref}} = -\oint R_v r_v \Gamma dz \quad , \tag{3.34}$$

where Γ is the lapse rate of the reference profile. Equation 3.33 is the form of the equation that is used to calculate this term numerically in the contour integrals, whereas Equation 3.34 provides a more useful form in developing scaling arguments below.

The new term in the form shown in Equation 3.33 bears a similarity to a term in the water vapour component of the Gibbs penalty $\oint(-\mathcal{G}_v)\mathrm{d}r_v$, depending as it does on the same state variables since:

$$\mathcal{G}_v = c_l\left(T - T_0 - T\ln\frac{T}{T_0}\right) + R_v T\ln\mathcal{H} \tag{3.35}$$

where c_l is the specific heat capacity of liquid water at constant pressure, T_0 the temperature at its triple point and $\mathcal{H}$ the relative humidity. One can therefore introduce a modified specific Gibbs free energy for the vapour state:

$$\mathcal{G}^*_v = c_l\left(T - T_0 - T\ln\frac{T}{T_0}\right) + R_v T(1 + \ln\mathcal{H}) \tag{3.36}$$

and (neglecting a term in $T_{\mathrm{ref}} - T$) instead of Equation 3.22 one can write:

$$\oint T\mathrm{d}s \approx \oint B\mathrm{d}z + \oint r_T g\mathrm{d}z + \sum_{w=v,l,i}\oint(-\mathcal{G}^*_w)\mathrm{d}r_w \tag{3.37}$$

where $\mathcal{G}^*_w = \mathcal{G}_w$ for $w = l, i$. It could be argued that from a physical perspective this term is a correction to the mechanical work generated and should therefore instead be combined with W_b. In this thesis we decided to keep the definition of W_b as in Pauluis (2016) and modify the Gibbs penalty term as above.

As one might expect the total atmosphere to be close to hydrostatic equilibrium in reality, this would suggest that variations in p' would largely balance variations in e, and that consequently an analagous term in p' could be calculated, which will largely compensate the new term in e derived above. If this were to be included, Equation 3.37 would continue to have a slight discrepancy as before. It is possible that the CRM does not achieve this overall hydrostatic equilibrium, or that some other feature is responsible for this continuing discrepancy; this has not been investigated further. In any case, the discrepancy is relatively minor and the narrative presented by the results shown in the remaining sections of this chapter is unaffected by it.

The impact of these adjustments are shown in Table 3.1 for a control case that consists of one

single column, uncoupled, and run to radiative-convective equilibrium. The SST is 302.7 K and the results are sampled every 30 minutes over the last 100 days of a 120 day run, referred to as the uncoupled control case. The values of various fields for this control case have already been presented in section 3.4. The stream function, the fitted contours and thermodynamic diagrams representing the most significant components of Equation 3.37 are shown in Figure 3.6.

Figure 3.6 c) shows the averaged paths in $S - T$ coordinates which is used to calculate the value of the Carnot maximum term. Following Pauluis (2016) this can be interpreted as follows. Parcels of air at high temperatures at the surface increase in entropy as moisture evaporates into them. They then rise and due to mixing in the boundary layer lose entropy through entrainment. Further ascent is approximately adiabatic, until a maximum height is reached. This is then followed by slow descent, where radiative cooling decreases entropy, until mixing occurs and the parcels gain entropy again and the cycle recommences.

Figure 3.6 d) shows the averaged paths in $B - z$ coordinates used to calculate the buoyancy term. Lighter air rises, and the moister parcels become more buoyant as they rise and latent heating occurs. There are some irregularities at the top of their path for the outermost contours, which arise from sparse field sampling and the negative contribution of ice content to entropy, but these do not have a major impact on the numerical values. The parcels descend at close to zero buoyancy, Near the surface, however, there are a number of cycles where lighter air subsides and heavier air rises which can be interpreted as mechanically forced overturning in the boundary layer.

Figure 3.6 e) shows the averaged paths in $r_T - z$ coordinates used to calculate the elevator term W_p. Moister air rises, dying out as it does so due to a mixture of entrainment at the lower levels and then precipitation. As air parcels descend they moisten due to evaporation of precipitation and mixing. The same irregularities as discussed above for the outermost cycles as they begin their descent is evident. Further evaporation occurs at the surface.

Figure 3.6 f) shows the averaged paths in $r_v - \mathcal{G}_v$ coordinates used to calculate the Gibbs penalty term for water vapour (the remaining terms are less significant). $\mathcal{G}_v$ is to first order a multiple of the log of the relative humidity. Thus as air at the surface moistens the values of $\mathcal{G}_v$ become zero and as air rises this continues to be the case. As the air starts to freeze the relative humidity decreases, and then increases again as it descends due to evaporation of precipitation and mixing.
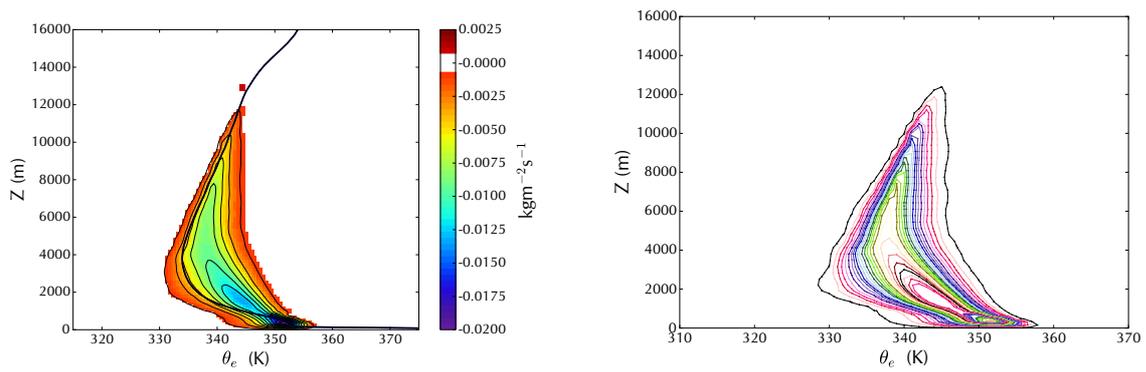
(a) *Convective Mass-flux streamfunction* Ψ

(b) *Contours of* Ψ *used to define trajectories for contour integrals*
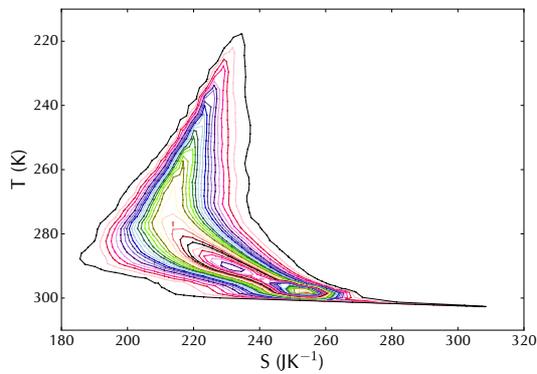
(c) *Paths in* $S - T$ *space - used to calculate* W_{Tds}
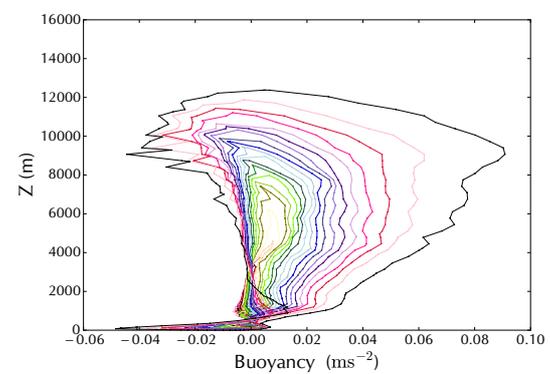
(d) *Paths in* $B - z$ *space - used to calculate* W_b
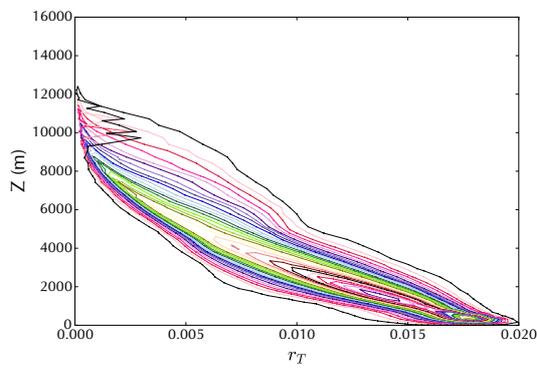
(e) *Paths in* $R_T - z$ *space - used to calculate* W_p
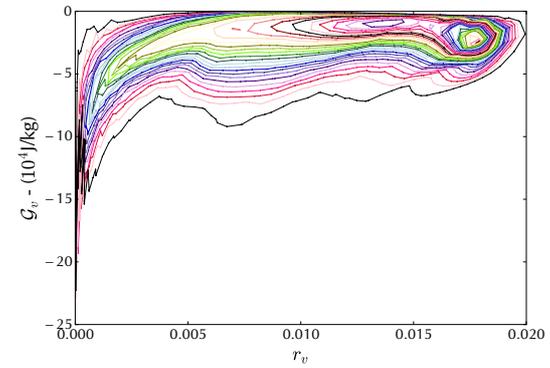
(f) *Paths in* $r_v - \mathcal{G}_v$ *space - used to calculate* $\Delta\mathcal{G}_v$

Figure 3.6: *Contours used to calculate values in Table 3.1 and thermodynamic diagrams representing main components thereof.*

(W m^{-2})	W_{Tds}	W_b	W_p	$\Delta\mathcal{G}$	Δ	$\Delta\mathcal{G}^*$	Δ^*
Control case	11.17	2.18	3.14	6.32	-0.47	5.81	0.04
Pauluis (2016)	8.3	1.5	2.5	4.6	-0.3	-	-

Table 3.1: *Numerical values for components of Equation 3.37 for control case*

Numerical results are shown in Table 3.1 for 60 contours - comparable values from Pauluis (2016) are also shown. It will be seen that the effect of the correction term is to reduce the absolute magnitude of the imbalance from -0.47 W m^{-2} to -0.04 W m^{-2} in this case. Overall, whilst the values calculated are larger than those obtained in Pauluis (2016), doubtless due in part to the higher surface temperature and different model configuration (as discussed in Section 3.4), the ratios of the various components are broadly consistent between the two sets of results. These relative values will be discussed further in Section 3.12.

3.6 CONTOUR AND SURFACE INTEGRALS

Pauluis (2016) calculates the components of the mechanical energy budget using 20 equally spaced contours covering the range in which the vertical stream function Ψ is negative. The choice of the number of contours was investigated for the control case. Figure 3.7 shows the value of each of the main components of Equation 3.37 for increasing numbers of contours. Using 60 contours produces values within a few percent of the value for 100 contours (except for W_b where the variation is slightly greater) - this variation can be compared with the standard error that is estimated in the next section. The values shown in this thesis are therefore calculated using 60 contours unless otherwise stated.

The use of a method based on surface integrals rather than contours was also investigated. The weighted value for W_{Tds} for all trajectories bounded above by the contour $\Psi = \Psi_0$ can be
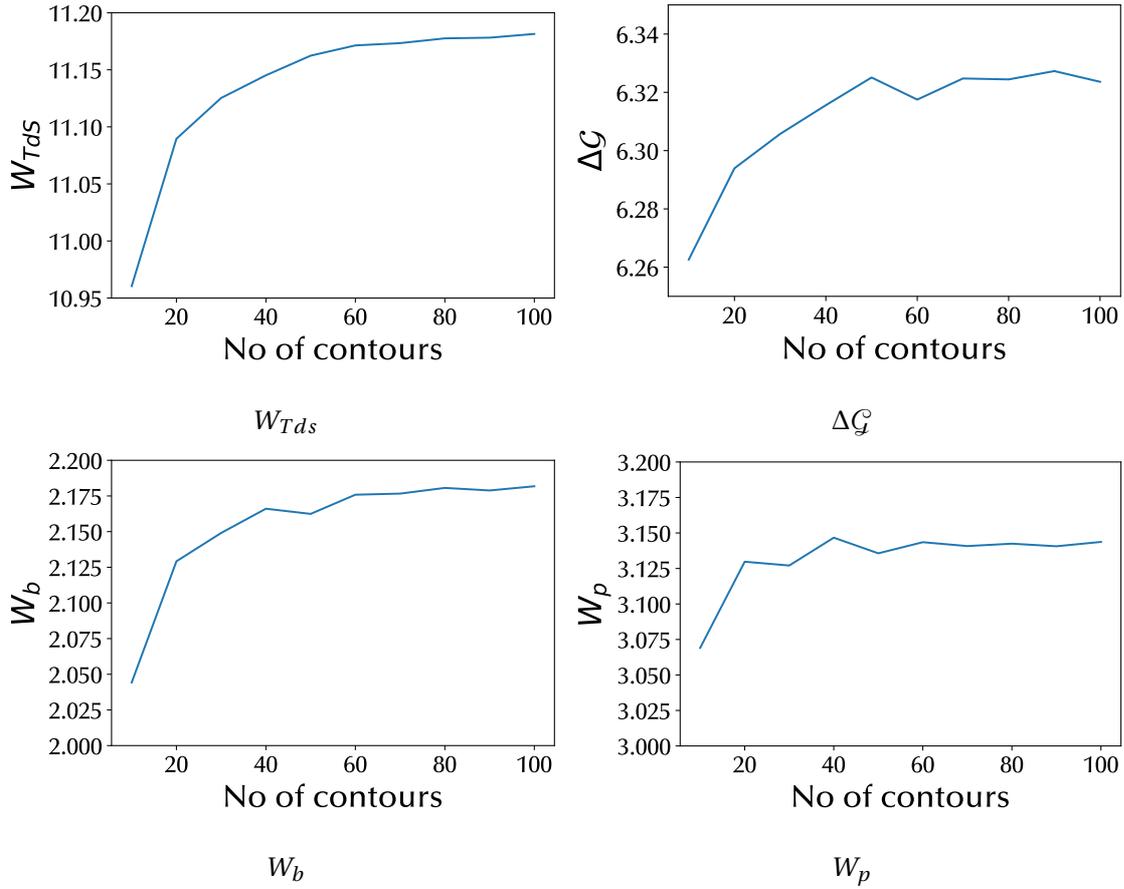
Figure 3.7: *Calculated values of main components of work done as a function of the number of contours*

expressed as:

$$W_{Tds} = \int\limits_{\Psi < \Psi_0} \oint T ds \, d\Psi \tag{3.38}$$

$$= - \int\limits_{\Psi < \Psi_0} \iint \left(\frac{\partial T}{\partial T} \right) ds \, dT \, d\Psi \tag{3.39}$$

$$= \iint (\Psi_0 - \Psi(s, T)) \mathfrak{H}(\Psi_0 - \Psi(s, T)) ds \, dT \tag{3.40}$$

$$= \iint (\Psi_0 - \Psi(s, T)) \mathfrak{H}(\Psi_0 - \Psi(s, T)) \left| \frac{\partial(s, T)}{\partial(\theta_e, z)} \right| d\theta_e dz \quad , \tag{3.41}$$

having made use of Green's theorem, where $\mathfrak{H}$ represents the Heaviside function and the Jacobian determinant is given by :

$$\left| \frac{\partial(s, T)}{\partial(\theta_e, z)} \right| = \frac{\partial s}{\partial \theta_e} \frac{\partial T}{\partial z} - \frac{\partial T}{\partial \theta_e} \frac{\partial s}{\partial z} \quad . \tag{3.42}$$

Hence:

$$W_{Tds} = - \iint_{\Psi<0} \Psi(\theta_e, z) \left(\left(\frac{\partial s}{\partial \theta_e} \right)_z \left(\frac{\partial T}{\partial z} \right)_{\theta_e} - \left(\frac{\partial s}{\partial z} \right)_{\theta_e} \left(\frac{\partial T}{\partial \theta_e} \right)_z \right) \mathrm{d}\theta_e \mathrm{d}z \qquad (3.43)$$

$$= - \iint_{\Psi<0} \Psi(\theta_e, z) \frac{c_p}{\theta_e} \left(\frac{\partial T}{\partial z} \right)_{\theta_e} \mathrm{d}\theta_e \mathrm{d}z \qquad (3.44)$$

since $s = c_p \log \frac{\theta_e}{T_0}$. $- \left(\frac{\partial T}{\partial z} \right)_{\theta_e}$ is the lapse rate Γ and can be treated as a smooth function of height. This gives:

$$W_{Tds} = \iint_{\Psi<0} \Psi(\theta_e, z) \frac{c_p}{\theta_e} \Gamma d\theta_e \mathrm{d}z \qquad (3.45)$$

Expressions for the other components of Equation 3.37 are more complex, but these quantities can be calculated using values of the Jacobian obtained numerically. The main results in this work were obtained from contour integrals, but the values for main components of Equation 3.37 were also calculated using surface integrals as a check which has proved broadly satisfactory (see Table 3.2), and both methods were also used to estimate the standard error in the estimates of that equation (see Section 3.7). The fact that these quantities can be calculated using surface integrals also underpins the application of this diagnostic framework to two coupled columns as discussed in Section 3.8.

(W m^{-2})	W_{Tds}	$\Delta \mathcal{G}$	W_b	W_p
-Contour integrals	11.17	6.32	2.18	3.14
-Surface integrals	11.13	6.32	2.27	3.34

Table 3.2: *Numerical values for components of Equation 3.37 for control case*

3.7   STATISTICAL EQUILIBRIUM AND STATISTICAL SIGNIFICANCE

In this chapter we analyse the various components of the mechanical energy budget (according to Equation 3.37) for sets of results produced by the LEM model with different parameters and configurations. Since the results are all averaged over many periods, (generally samples every 30 minutes over the last 100 days of a 120 day run) one can obtain some measures of the

variability of the results, in order to confirm that the model has been run for a sufficiently long period for the results to be stable and to appreciate the significance of any differences between run results. Analysis confirms that the values of the key fields, such as temperature and specific humidity, in (θ_e, z) space are relatively constant for all time periods (as might be expected from the sorting by values of θ_e). On the other hand, the values of the streamfunctions do vary quite significantly, as can be seen in Figure 3.9, and for many individual time periods the contours may not be closed and the calculation may simply not be possible. Consequently the calculation of statistical errors in the values of the components of Equation 3.37 by estimating the variability of values calculated by contours for individual time periods has proved unsatisfactory - instead such errors can be assessed using contours based on subsamples.

The control case of a single column with SST of 302.7K was again studied for this purpose. In addition to calculating central values based on the entire run, these quantities were also calculated for a number of random sub-samples (of N_s=100, 500 and 1000 samples) out of the $N_{tot} = 4799$ time periods available. The means and standard deviations of the means of the sub-sample sets of the values of the components of Equation 3.37 for these sets of sub-samples were calculated. The standard deviations of the means of the sub-sample sets decrease as N_s increases and the $N_s = 1000$ values can be regarded as an upper bound on the values for the full run for N_{tot} time periods.

Values of each of W_b, W_p and $\mathcal{G}$ are plotted against W_{Tds} for the random sub-samples for $N_s = 100$ as well as is the entire set of results (red dot) in Figure 3.8. It will be noted that there

(a) $\Delta\mathcal{G}$ (b) W_b (c) W_p
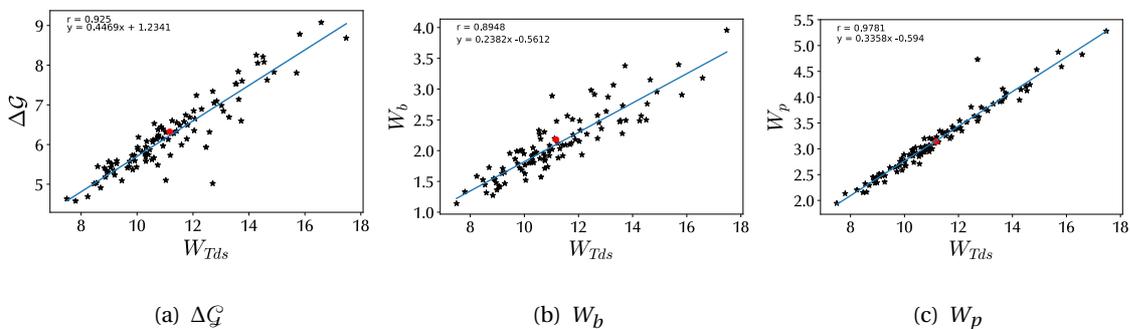
Figure 3.8: *Scatter plots of components of work done against W_{TdS} for sub-samples. The red dots indicate the mean values for the total samples.*

(W m^{-2})	W_{Tds}	$\Delta\mathcal{G}$	W_b	W_p
Values based on N_{tot} samples	11.17	6.32	2.18	3.14
N_s=100, 100 sub-samples				
Mean of sub-sample	11.23	6.25	2.11	3.18
σ of mean of sub-sample sets	1.98	0.96	0.53	0.68
N_s=500, 20 sub-samples				
Mean of sub-sample	11.58	6.41	2.21	3.29
σ of mean of sub-sample sets	0.94	0.45	0.26	0.31
N_s=1000, 10 sub-samples				
Mean of sub-sample	11.05	6.16	2.10	3.11
σ of mean of sub-sample sets	0.66	0.39	0.13	0.20

Table 3.3: *Variability of components for work done estimated by subsamples (base case, contour integrals)*

is a strong correlation between the magnitude of W_{Tds} and of each of its components.

The surface integral methodology introduced in section 3.6 provides an alternative method of calculating the standard error of the estimators. Stream functions were calculated for each of the time-periods in N_{tot} using values of the fields averaged over N_t samples, and the surface integrals were calculated over the space bounded by $\Psi = 0$ for the average stream-function based on all N_{tot} time-periods - this represents the contribution of each sample to the total average, but use of this domain may produce quite anomalous results for a particular time period. The values obtained are shown in Table 3.4.

(W m^{-2})	W_{Tds}	$\Delta\mathcal{G}$	W_b	W_p
Mean of sample	11.55	4.57	3.37	3.91
σ of sample	23.54	8.27	8.05	9.60
Implied σ of mean	0.34	0.14	0.12	0.12

Table 3.4: *Variability of components for work done estimated by surface integral contribution (base case)*

The results of this calculation are in many ways unsatisfactory, with significant differences between the mean values shown here and those presented in Table 3.2. This may well be to do with the manner in which negative and positive contributions to the total are offset at an individual time-period level. However the standard errors derived by this method are broadly consistent with the values and trends observed in Table 3.3 and can be used as an estimator of the standard deviation of the mean of the entire sample .

Both sets of results imply a considerable degree of variability from one time period to the next - this can be seen by inspecting Figure 3.9 which shows the streamfunctions (or rather the integrals of vertical mass flux) for five example time-periods, chosen as they represent the 10th, 30th, 50th, 70th, and 90th percentiles of the contributions to $W_{T\mathrm{d}s}$ using the surface integral approach, compared with the stream function averaged over the period of the projection. In particular, whereas for the sample as a whole upward and downward motion will approximately compensate, this is far from the case for any individual time period.

The degree of variability becomes apparent from the (truncated) histogram plot of the distribution of the value of the contribution to $W_{T\mathrm{d}s}$ of each time sample (again calculated using surface integrals) which is shown in Figure 3.10. This shows not only that some samples provide a negative contribution (such as the streamfunction in Figure 3.9(a), where there is vigorous upward motion at low values of θ_e), but that some samples provide very strong contributions. The mean value calculated is very clearly greater than the median value (which is around 4 W m^{-2}), and thus the long tail means that even with N_{tot}=4799 the values estimated are subject to significant variability. Figure 3.11 shows how these contributions to $W_{T\mathrm{d}s}$ vary over the period selected for the sample - this confirms the assessment in section 3.3 that there is no perceptible drift in this sample.

(a) *10th percentile*

(b) *30th percentile*

(c) *50th percentile*

(d) *70th percentile*

(e) *90th percentile*
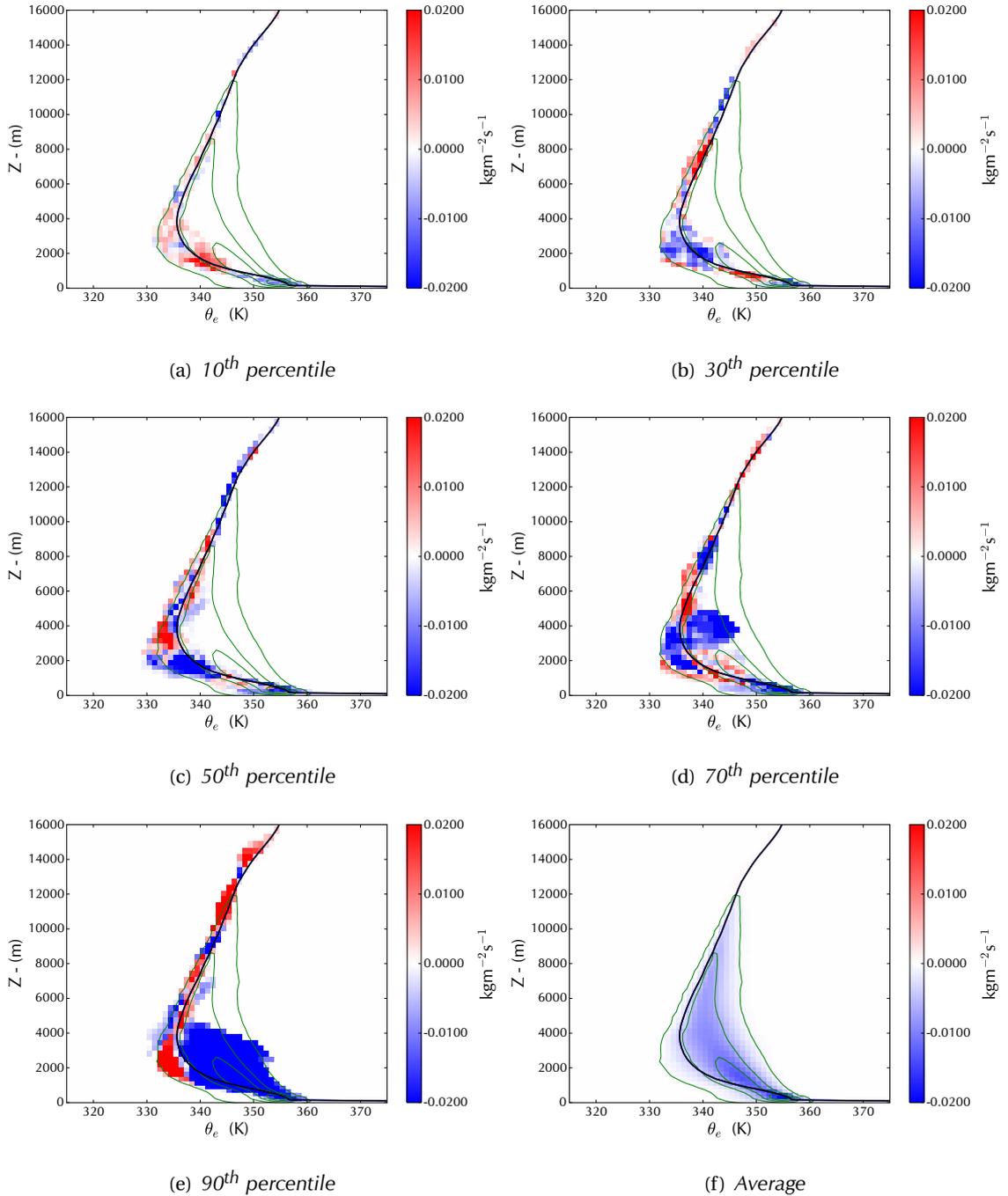
(f) *Average*

Figure 3.9: *Streamfunctions for selected percentile contributors to W_{Tds} compared with the average streamfunction (panel f, also shown in green on percentile plots). Values in excess of the colour bar scales are shown as blue or red as appropriate.*

(a) *Normal scale*   (b) *Log scale*
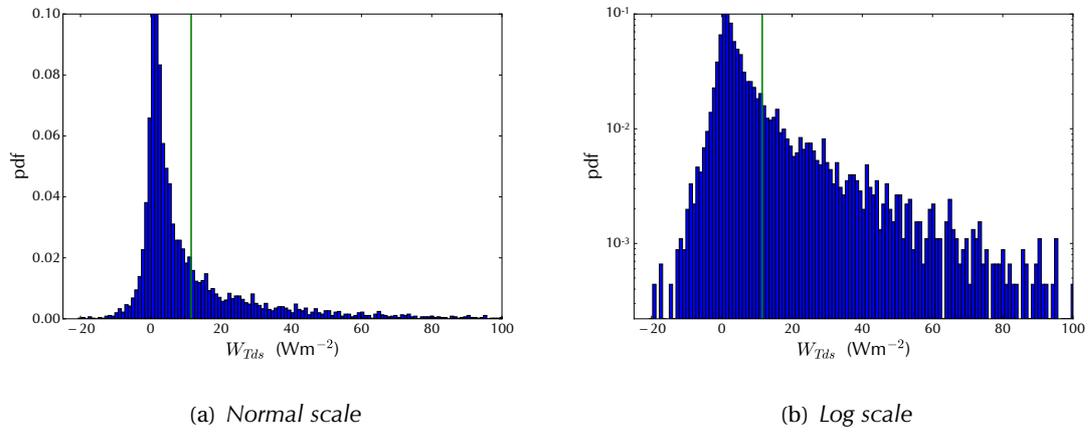
Figure 3.10: *Distribution of contributions to W_{Tds} - the green line represents the sample mean value.*
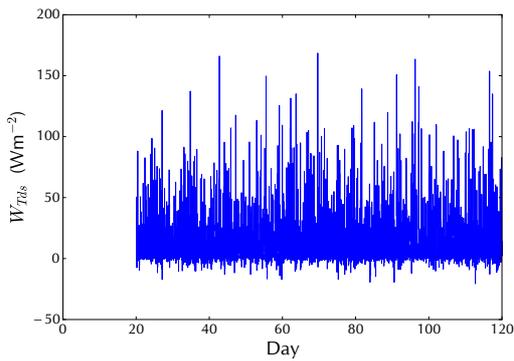
Figure 3.11: *Contributions to W_{Tds} over the sample period.*
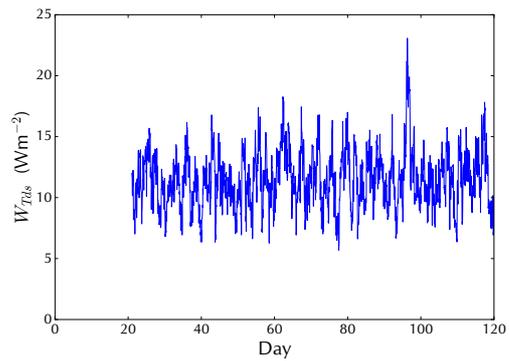
Figure 3.12: *Contributions to W_{Tds} over the sample period - rolling 24 hour average.*

3.8   Extension to coupled system

The model was then run for two regions coupled using the WTG approximation. Each region is modelled in a separate LEM run, and a large-scale vertical velocity, calculated using the WTG and the difference between the mean potential temperatures at each height level between the two regions, is superimposed on the motions within each region. It is assumed that horizontal advection between the regions is determined by the divergence of vertical advection through the anelastic equation, and that both potential temperature and water vapour are advected. Fuller details of how the LEM was modified to represent this coupling can be found in Daleu et al. (2012).

Initially, runs were performed for two equal regions ($\epsilon = 0.5$), where the SST below the warm region was 2 K higher (ΔT_s) than for the cool region and the coupling timescale parameter (τ is used instead of τ_{WTG} in this Chapter) was 2 hours. This configuration is referred to as the coupled control case. It is instructive to compare some of the conditional average plots for the two coupled regions with those for the uncoupled run discussed in section 3.4. Figure 3.13 shows these for the $\log_{10}$ of the normalised mass density function and the average relative humidity. It will be seen that the warm region does not differ markedly in overall shape from the control case, but that the cool region dries out markedly. The warm region is largely constrained by the moist adiabat, whereas in the cool region the large-scale descent of dry air can influence the profile markedly.

The large-scale velocities produced by the coupling methodology, and the impact of the coupling on the potential temperatures and r_v in each of the regions for WTG coupling with $\tau = 2$ hours and $\tau = 24$ hours is shown in Figure 3.14. It will be seen that as in Figures 2.4 and 2.20, the effect of the coupling is to reduce the temperature difference between the regions and that stronger coupling increases the large-scale velocity. Coupling dries out the cool region without having a marked effect on the warm region - there is relatively little difference between the two coupled runs in terms of humidity, particularly in the warm region.

(a) *Uncoupled* (b) *Cool region* (c) *Warm region*

(d) *Uncoupled* (e) *Cool region* (f) *Warm region*
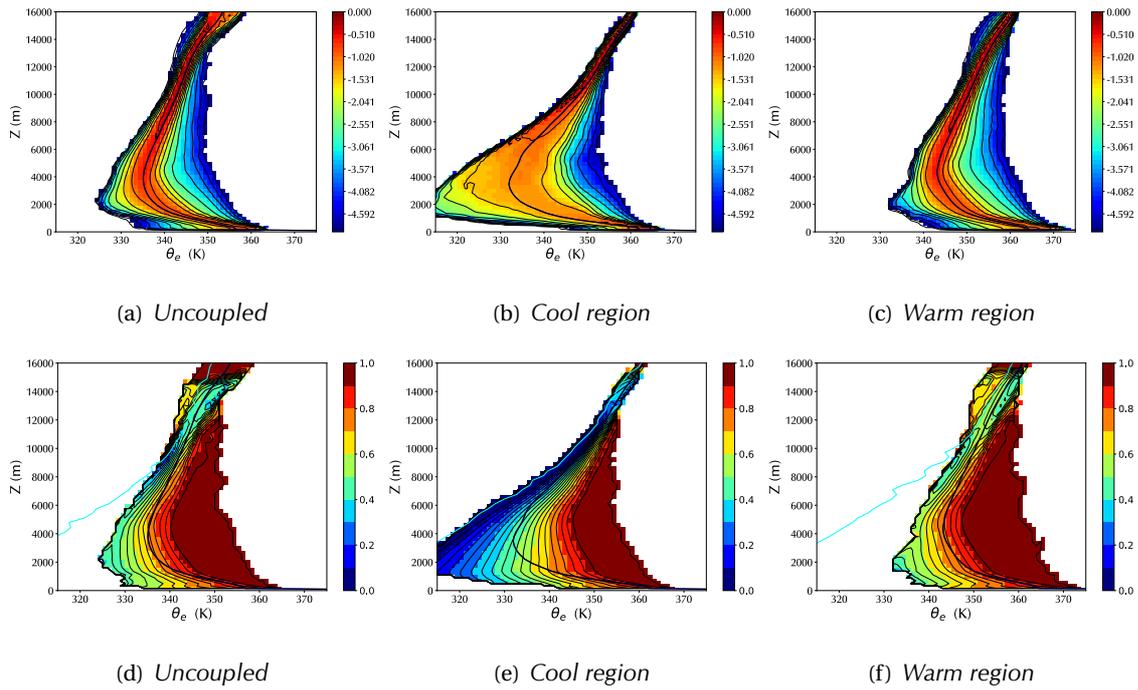
Figure 3.13: *Comparison of* $\log_{10}$ *of the normalised mass distribution function (a, b, c) and relative humidity (d, e, f) for the uncoupled and coupled regions for* τ *= 2 hours. Black solid line indicates mean* θ_e *at each height level, and cyan line in bottom panels indicates zero relative humidity. The two regions are of equal size (*$\epsilon = 0.5$ *and the SST temperature difference is 2 K.)*

The decomposition of work done discussed in section 3.5 is more complex for a two-region system, where the regions are coupled by a large-scale circulation driven by vertical winds specified by the WTG approximation. When a temperature difference between the surfaces underlying the two regions gives rise to a large-scale circulation, there will be mass transfers between the two regions and the contours of the integral of the vertical mass flux (as in Equation 3.13) in each region will not be closed, making it impossible to estimate the components of Equation 3.37 within each region using either contour or surface integrals (the latter requiring a domain bounded by a constant value of the streamfunction) (see Figure 3.15 a) and c)).

One could, of course, merge the two regions prior to performing any analysis (see Figure 3.15 e)), but this introduces significant error as the dynamics are generally influenced by local rather than merged values of fields (e.g. buoyancy for $W_b = \oint B \mathrm{d}z$), and such a method will not permit a partitioning of the components of work done to localised features in each region

(a) *Potential temperature*

(b) *Potential temperature difference*

(c) *Large-scale velocity*

(d) *Vapour mixing ratio*
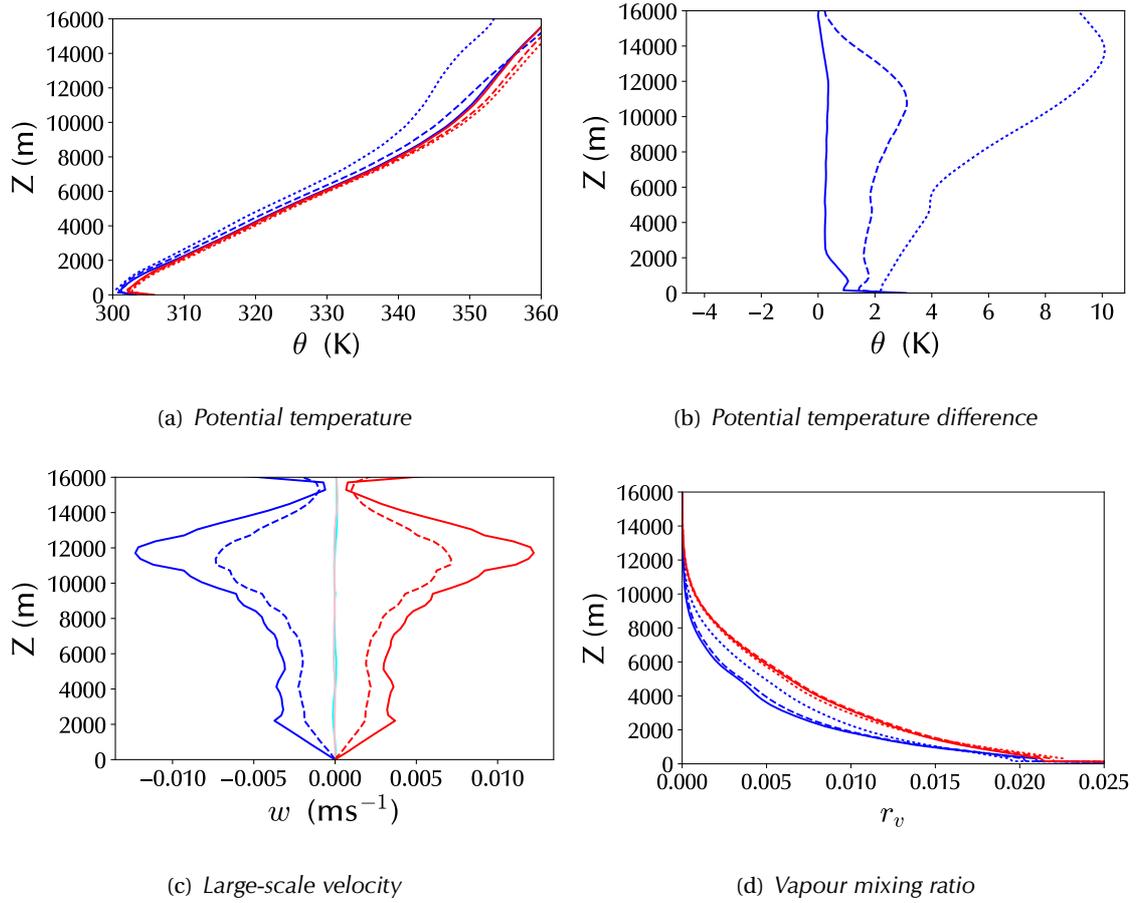
Figure 3.14: *Effect of coupling on a) potential temperature, b) potential temperature difference between regions, c) large-scale velocity and d) specific humidity in cool (blue) and warm (red) regions for uncoupled (dotted) and coupled regions for τ = 2 hours (solid) and τ = 24 hours (dashed). The two regions are of equal size ($\epsilon = 0.5$.)*

and to the large scale circulation.

Instead, one can identify and separate out the vertical large-scale velocities $w_{LS,1}(z)$, $w_{LS,2}(z)$ (obtained from the values of $\Psi(z, \theta_e)$ as $\theta_e \to \infty$ and the dry air mass distribution in each region, the cooler region is identified by a subscript 1 and represents a fraction $1 - \epsilon$ of the total area, and the warmer region (subscript 2) a fraction ϵ), for an example see Figure 3.14 c). The circulations calculated using Equation 3.13 for residual local velocities $w_i^* = w_i - w_{LS,i}$ ($i = 1, 2$) in each region will now be closed, as will that in a notional third "region" which consists of the total of the large-scale circulation within the two regions, weighted by their relative areas, since

$(1-\epsilon)\,w_{LS,1} + \epsilon\,w_{LS,2} = 0$. These streamfunctions are additive by construction:

$$\Psi_1 + \Psi_2 = \Psi_1^* + \Psi_2^* + \Psi_{LS} \quad , \tag{3.46}$$

where $\Psi_{1,2}$ are the streamfunctions, or rather integrated mass fluxes, of the observed circulations in each region, $\Psi_{1,2}^*$ represent the streamfunctions for the adjusted local circulations based on $w_{1,2}^*$ and Ψ_{LS} is the streamfunction for the large-scale circulation based on $w_{LS,i}$ in each of the two regions. The respective surface integrals will also be additive, providing that a domain is selected that is bounded by the $\Psi = 0$ contour and that $\Psi \leqslant 0$ throughout that domain (which should generally be possible for a sufficiently smooth system). This additivity is important because it means that the partitioning of work in Equation 3.37 can also be extended to the components of the coupled two-region system. For example:

$$W_{TdS} = \iint \Psi_1^* \mathrm{d}S\mathrm{d}T + \iint \Psi_2^* \mathrm{d}S\mathrm{d}T + \iint \Psi_{LS}\mathrm{d}S\mathrm{d}T \tag{3.47}$$

Since the surface integrals are additive, a calculation of these quantities using contour integrals will also be additive. An example of this partitioning can be seen in Figure 3.15 b), d), and f).

As has been mentioned, these integrals are calculated for the entire system using weighted trajectories along contours of the streamfunction in (θ_e, z) space, and with averaged values for the other quantities required for the calculation. The values are calculated separately for each region while for the large-scale circulation a mean value is taken, weighted by the contribution of each region to that point in the combined thermodynamic space. As a result of this, the calculation of the large-scale terms is more approximate. Values obtained using this approach are shown in Table 3.5, together with values for both regions merged prior to any analysis.

(a) *Cool region* (Ψ_1)

(b) *Cool region excluding Large Scale circulation* (Ψ_1^*)

(c) *Warm region* (Ψ_2)

(d) *Warm region excluding Large Scale circulation* (Ψ_2^*)

(e) *Both regions combined* ($\Psi_1 + \Psi_2$)

(f) *Large Scale circulation only both regions combined* (Ψ_{LS})
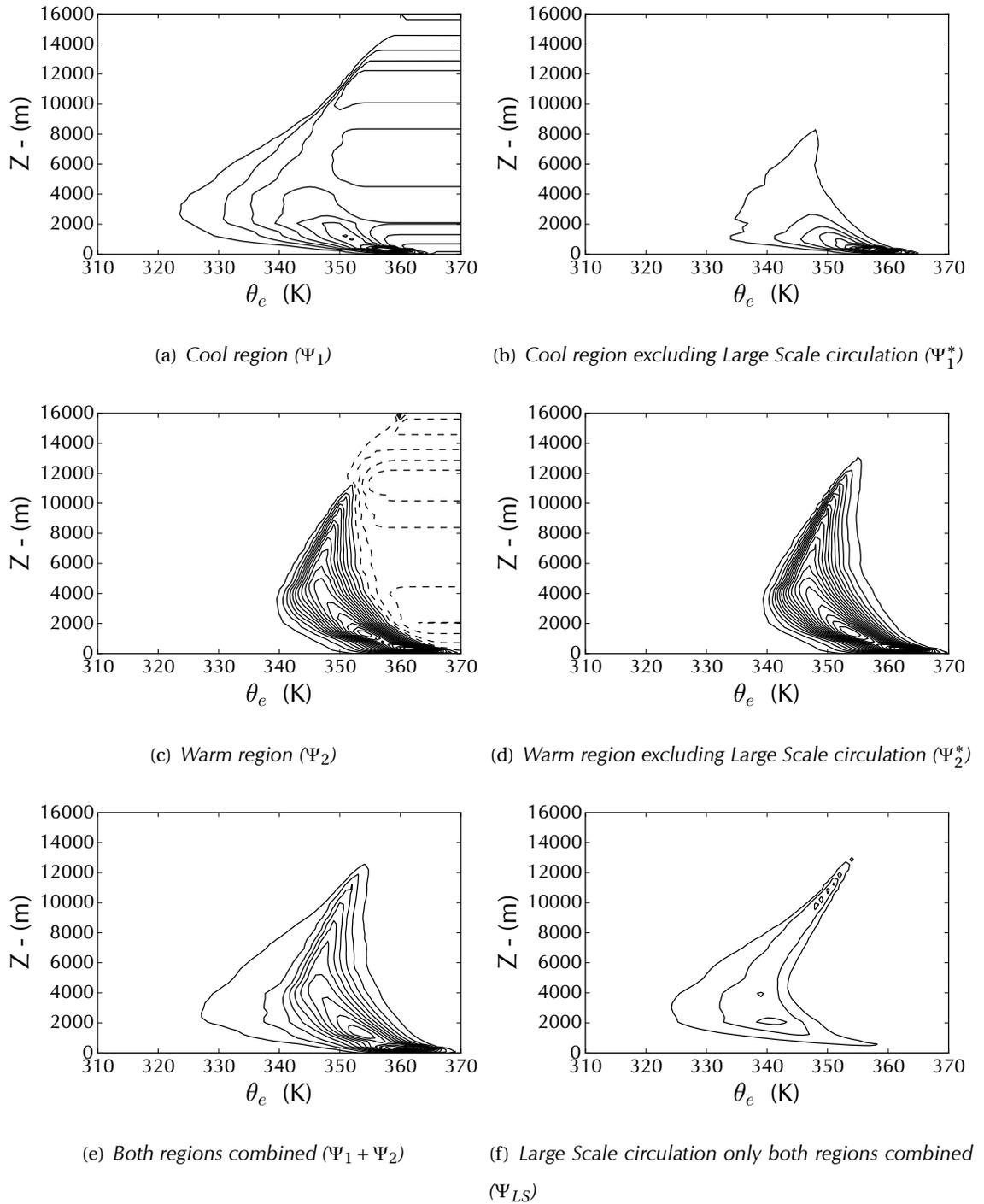
Figure 3.15: *Stream function contours for two coupled columns with $\tau = 2$ hours showing effect of treating the Large Scale circulation separately. The two regions are of equal area ($\epsilon = 0.5$).*

(W m^{-2})	W_{Tds}	W_b	W_p	$\Delta\mathcal{G}$	Correction	Imbalance
Cool region	2.91	0.24	0.69	2.14	-0.15	-0.01
Warm region	16.39	3.40	4.93	8.67	-0.78	0.17
Large-Scale	1.72	0.30	0.30	1.12	-	0.00
Total	11.37	2.13	3.11	6.53	-0.46	0.07
Merged	11.00	2.47	3.06	5.91	-0.53	0.04

Table 3.5: *Components of work done for τ = 2 hours; the correction refers to the anelastic adjustment in Equation 3.33, the imbalance is positive when W_{Tds} is greater than the sum of the remaining columns. The two regions are of equal area ($\epsilon = 0.5$).*

It will be seen that the values obtained by this methodology are similar in magnitude to those obtained by merging the regions, but that the differences between the two sets of values exceed the standard errors discussed in section 3.7. As expected, there are significant differences for the buoyancy term, and also for the Gibbs function term, which are reflected in the total. There remains an imbalance in the warm region, even after the anelastic correction term is included, but overall the balance of the equation is acceptable and permits further analysis.

3.9 IMPACT OF STRENGTH OF COUPLING

Next we investigated the sensitivity of the results obtained following the method described in section 3.8 to changes in the WTG timescale parameter τ. Results, together with error bars showing the standard errors obtained following the method in section 3.7 are plotted in Figure 3.16.

It will be seen that values of the components of work done for the total system remain broadly constant (Figure 3.16a, although the introduction of coupling produces a marginal increase in W_b and W_{Tds} which then reduces as the coupling increases. This implies that coupling does not significantly influence the energetic balance of the system in aggregate.

(a) *Total system*

(b) *Large-scale circulation*

(c) *Cool region*
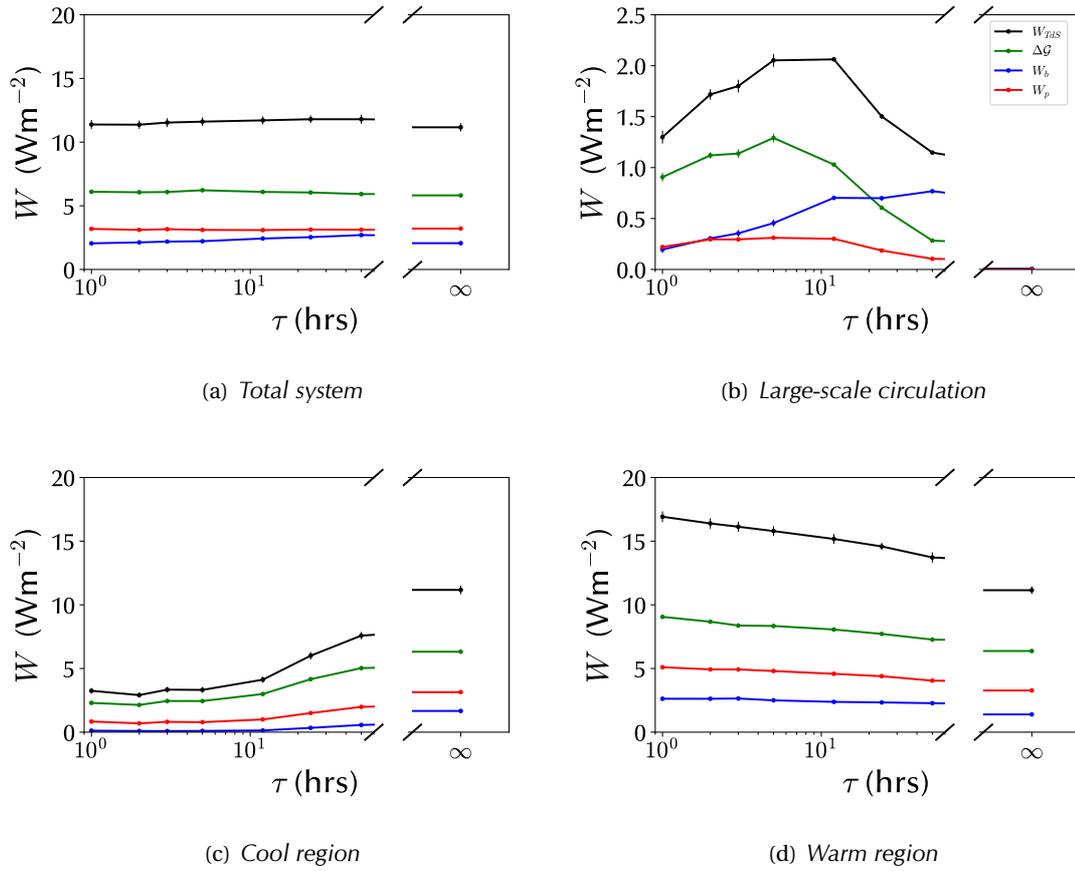
(d) *Warm region*

Figure 3.16: *Components of Equation 3.37 for (a) the total system, (b) the large-scale circulation and (c) (d) the residual circulations in the cooler and warmer regions for varying coupling strengths. A high value of the coupling timescale parameter τ indicates weak coupling. The blue line indicates W_b, the red W_p, the green ΔG^* and the black line W_{Tds}. Error bars represent the standard error in the estimate of the parameter, obtained by subsampling. Note panel b) has a different y-axis range to the remaining plots.*

Values for the local circulations in each of the regions (Figures 3.16c and 3.16d) on the other hand exhibit a significant difference from the overall mean. This difference is already marked at very weak coupling and increases as the value of τ reduces, although the values for the cooler region remain almost constant for $\tau < 10$ hours, possibly reflecting the fact that the region approaches a humidity minimum. Column integrated water vapour in that region reduces significantly between $\tau = 50$ hours and $\tau = 10$ hours and then shows less variation, indeed a slight increase for $\tau < 5$ hours (Figure 3.18). The vertical mass flux for the two regions for $\tau = 50$ hours (Figure 3.17) confirms that convection in the cooler region is markedly suppressed even for such weak coupling.

The large-scale circulation (Figure 3.16b) shows a different pattern; this includes both regions, which maintain a temperature difference, and hence W_b makes a greater relative contribution, reducing as the coupling increases and the temperature difference reduces. This reduction is partly compensated by a slight increase in W_p as a stronger circulation lifts more moisture. The Gibbs penalty increases with the coupling up to a maximum at around $\tau = 5$–10 hours before reducing; this can be attributed to increasing coupling first leading to drying of the cooler region and hence to a decrease in the relative humidity at which energy enters the system (see the scaling arguments below for how this impacts $\Delta \mathcal{G}$ non-linearly). As discussed above, as τ decreases below 5 hours the cooler region marginally moistens which contributes to the decrease in $\Delta \mathcal{G}$. The mechanical work terms for components of the large-scale circulation for strong coupling are similar in magnitude to those for the localised circulation in the cooler region; both are substantially smaller than those for the warmer region.

(a) *Cool region*
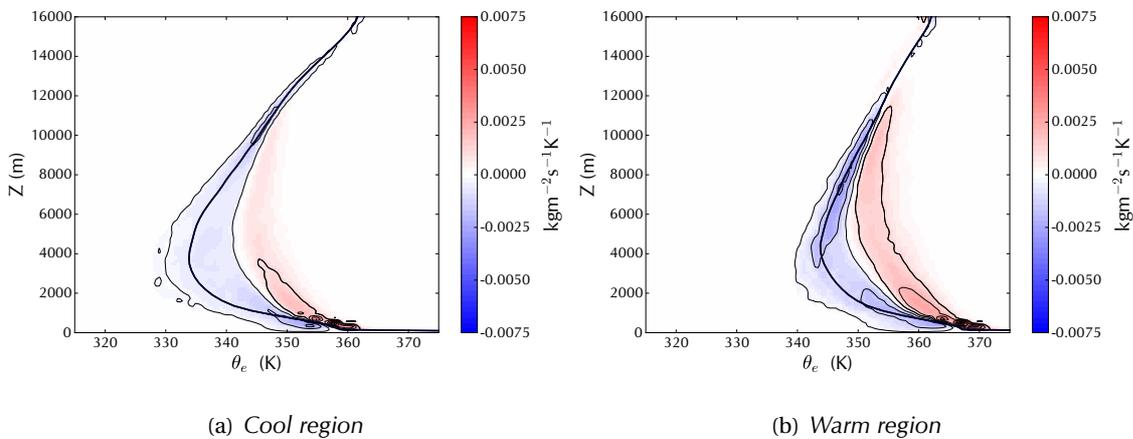
(b) *Warm region*

Figure 3.17: *Vertical mass flux for a) cool region and b) warm region for $\tau = 50$ hours.*

An expression for the rate of conversion of potential energy into kinetic energy under the WTG was obtained in the previous chapter (Equation 2.38). In view of the fact that the WTG is here expressed in terms of potential temperature anomalies and lapse rates, and the conversion term derivation of Equation 2.38 makes no allowance for moisture either (providing that $\bar{A}$ is calculated using θ rather than θ_v), the conversion term should be compared with W_b. The effect of the boundary layer interpolation is to weaken the coupling in the lowest layers, which
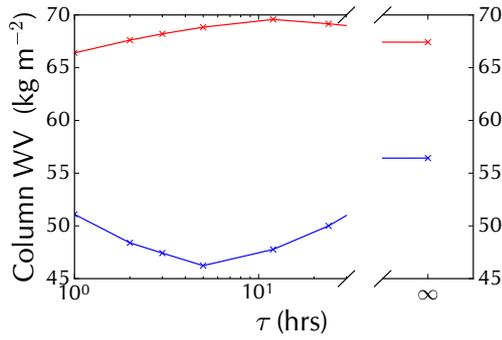
Figure 3.18: *Column integrated water vapour for the warm region (red) and cool region (blue)*
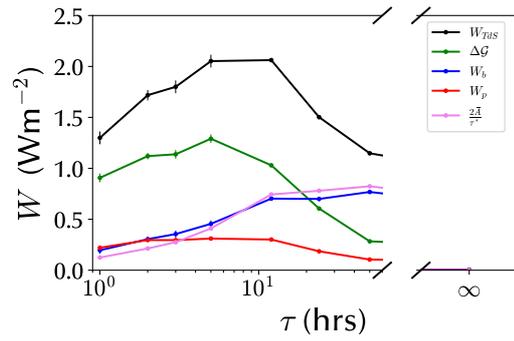
Figure 3.19: *As Figure 3.16b. In addition the conversion rate from potential to kinetic energy based on Equation 2.38 is shown in violet.*

can be represented by increasing the value of τ for those layers - the impact of this adjustment is minor. As will be seen in Figure 3.19, the comparison between the conversion term in Equation 2.38 and W_b is satisfactory.

3.10   Impact of temperature difference between regions

In a further experiment, the we varied the difference in SST between the two regions in a range between 0K (both regions at 303.7K) and 2K (as in the previous section) for two equally-sized regions for a timescale coupling parameter $\tau = 2$ hours. The values of the various components of work done are shown in Figure 3.20.

(a) *Total system*

(b) *Large-scale circulation*

(c) *Cool region*
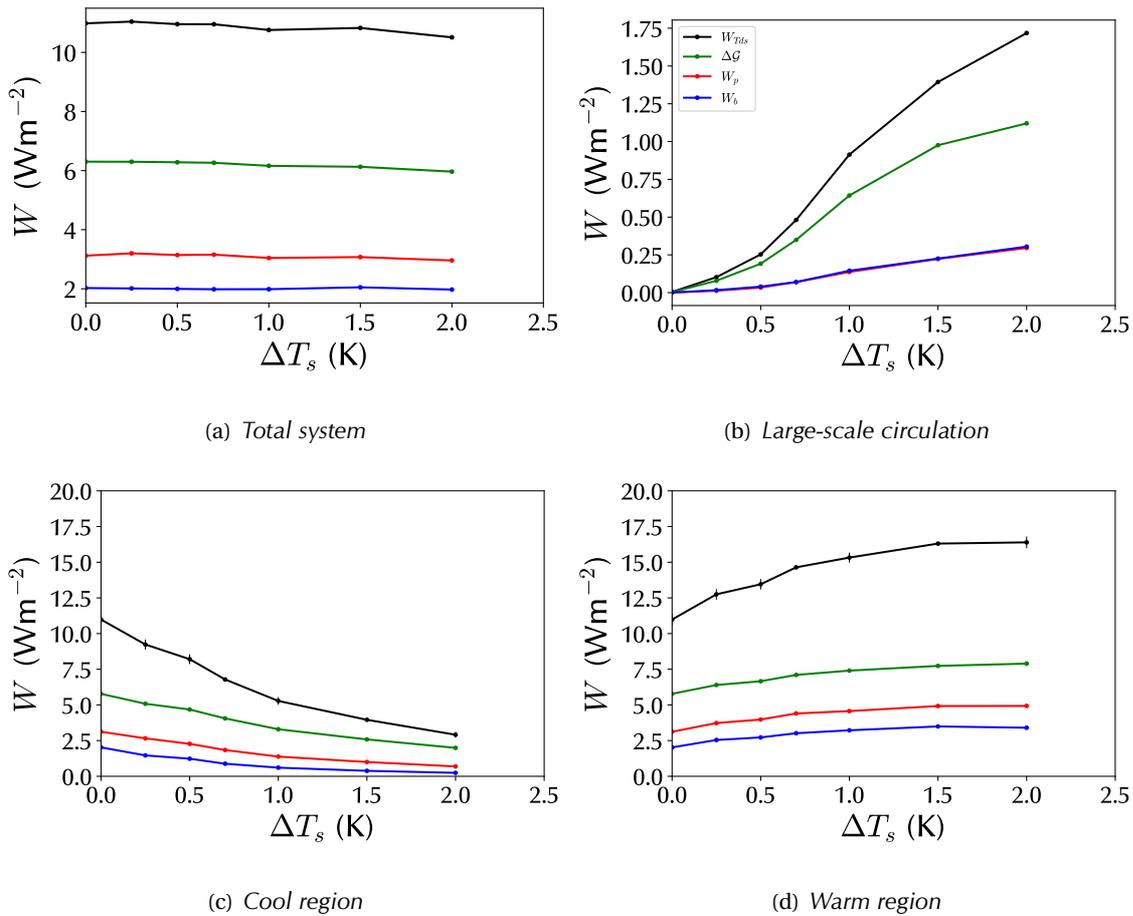
(d) *Warm region*

Figure 3.20: *Components of Equation 3.37 for (a) the total system, (b) the large-scale circulation and (c) (d) the residual circulations in the cooler and warmer regions for varying differences in the SSTs under the two regions. The blue line indicates W_b, the red W_p, the green ΔG^* and the black line W_{Tds}. Note panels a) and b) have a different y-axis range to the remaining plots.*

It is again striking that the total values for the entire system (Figure 3.20 a)) are relatively insensitive to changes in ΔT_s. The two regions (Figure 3.20 c) and d)) each start from the same values for $\Delta T_s = 0$, which are similar to those for the single column at RCE (discrepancies are of the order of the standard errors) and then diverge. The components of the large-scale circu-

lation (Figure 3.20 b)) show a quadratic dependency on ΔT_s, up to a temperature difference of 1 K, consistent with Equation 2.125. For greater temperature contrasts this quadratic relationship breaks down as the cool region approaches a humidity minimum (see moisture transport in Figure 3.23b)). These results do not exhibit the self-sustaining convection solution found in Figure 2.21 for the moist SCM run. The $\Delta T_S = 0$ run was initialised with slightly different temperature profiles in the the two regions but even this set-up did not generate self-sustaining convection.

3.11 IMPACT OF RELATIVE SIZE OF REGIONS

In a further numerical experiment, the relative size of the two regions was varied. The model set-up is as in previous sections, with $\tau = 2$ hours, the SSTs are all 1 K greater than in section 3.9 and the SST difference between the regions remains 2 K. The results for work done are shown in Figure 3.21.

As in previous experiments, the total values (Figure 3.21) are insensitive to changes in the parameters. As the relative size of the warm region decreases ($\epsilon \to 0$), the work done in each of the regions increases. The large-scale circulation components can be compared with the dependency of work done on $\epsilon(1-\epsilon)$ derived in Equation 2.125. There are a number of additional process that will contribute to the difference between these results, in particular the drying out of the cool region (Figure 3.22) between $\epsilon = 0$ and $\epsilon = 0.3$. The relationship between the large-scale Gibbs penalty and the moisture transport between the two regions is discussed in section 3.12.

(a) *Total system*

(b) *Large-scale circulation*

(c) *Cool region*
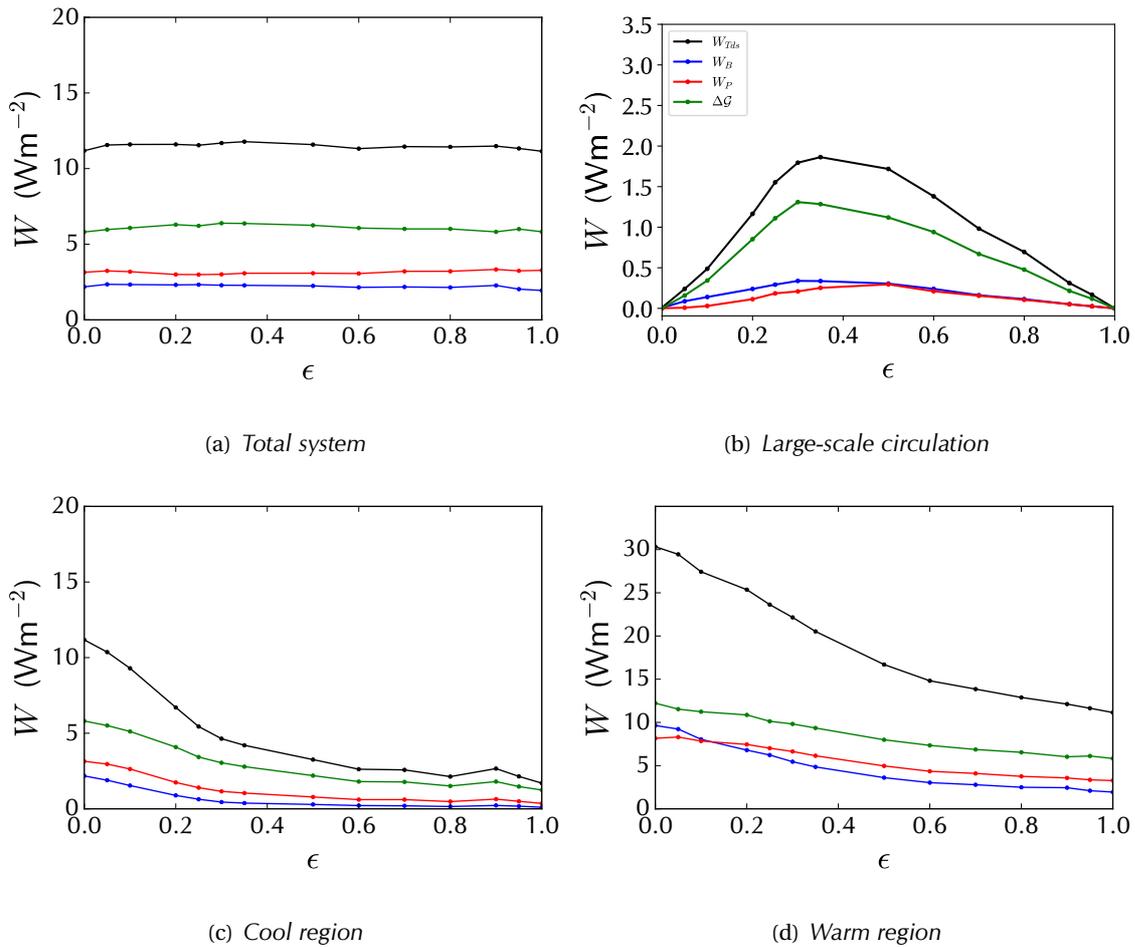
(d) *Warm region*

Figure 3.21: *Components of Equation 3.37 for (a) the total system, (b) the large-scale circulation and (c) (d) the residual circulations in the cooler and warmer regions for varying relative sizes of the two regions. The blue line indicates W_b, the red W_p, the green ΔG^* and the black line W_{Tds}. Note panels have different y-axis ranges.*

3.12 SCALINGS FOR COMPONENTS OF MECHANICAL ENERGY BUDGET

In an anelastic model such as the LEM, the buoyancy (see Gray et al. (2004, Equations 11 - 13)) is calculated as:

$$B = g\left(\frac{\theta'}{\theta_{\text{ref}}} + \left(\frac{R_v}{R_d} - 1 \right) r_v - \sum_{w \neq v} r_w \right) \quad , \tag{3.48}$$

where R_v and R_d are the specific gas constants for water vapour and dry air and θ_{ref} is the reference-state potential temperature. Hence, if one assumes that variations in specific hu-
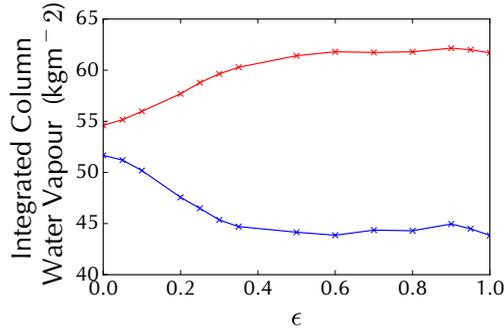
Figure 3.22: *Integrated column water vapour for the warm region (red) and cool region (blue)*

midity dominate the buoyancy rather than any temperature differences as is suggested by model results, and also that $\delta r_T \approx \delta r_v$, the buoyancy lifting term, W_b, will scale as $(\frac{R_v}{R_d} - 1) W_p \sim 0.6 \times W_p$, with W_p being the moisture lifting term. The approximate scaling between W_b and W_p can be readily verified from the numerical values shown in Table 3.1 for the uncoupled single region and also holds in most cases for both the warm and cool regions for the two-region system (Figures 3.16, 3.20 and 3.21) which also dominate the aggregate system. In circumstances where the temperature differences are significant (and correlated with moisture anomalies), such as for the large-scale circulation at high coupling strength (low values of τ), one could expect $\frac{W_b}{W_p}$ to have a value greater than 0.6, as is also observed in Figure 3.16 b). .

Pauluis (2011, Equation 25) gives an expression for the efficiency of a mixed Carnot steam cycle η_{mix} including the Gibbs penalty.

$$\eta_{\mathrm{mix}} = \frac{T_{\mathrm{in}} - T_{\mathrm{out}}}{T_{\mathrm{in}}} - \frac{1}{1 + B} \frac{R_v T_{\mathrm{out}}}{L_v} \ln \frac{\mathcal{H}_{\mathrm{in}}}{\mathcal{H}_{\mathrm{out}}} \quad , \tag{3.49}$$

where B is the Bowen ratio, $\mathcal{H}$ is relative humidity and the subscripts $_{\mathrm{in}}$, $_{\mathrm{out}}$ indicate conditional harmonic means over the zones where heat enters and leaves the system. For example, if one writes $\mathcal{F}_{\mathrm{in}}$ for heat input and $\mathcal{A}$ as the system's boundary then following Ambaum (2010, Equation 10.50):

$$\frac{1}{T_{\mathrm{in}}} = \left(\int_{\mathcal{A}} \mathcal{F}_{\mathrm{in}} \, d\mathcal{A} \right)^{-1} \int_{\mathcal{A}} \frac{\mathcal{F}_{\mathrm{in}}}{T} \, d\mathcal{A}. \tag{3.50}$$

T_out is defined likewise using $\mathscr{F}_\text{out}$, the heat output of the system, and $\mathscr{H}_\text{in}$ is defined as in Pauluis (2011, Equation 16).

The second term in Equation 3.49 relates to the work output associated with the evaporation of moisture into subsaturated air, which Pauluis subsequently refers to as the Gibbs penalty. Assuming that condensation occurs close to saturation (i.e. $\mathscr{H}_\text{out} = 1$), that vapour anomalies dominate as before, that the sensible heat component is negligible ($B = 0$) and that the energy input F_in is thus $L_v E$, where, E is the rate of evaporation $E = \frac{\Delta r_v}{\Delta t}$, we can approximate the Gibbs penalty as:

$$\Delta \mathcal{G} \approx - R_v T_\text{out} E \ln \mathscr{H}_\text{in} \tag{3.51}$$

Likewise, W_{Tds} will be mainly driven by the latent heat input and scales with the Carnot efficiency:

$$W_{Tds} \approx \frac{T_\text{in} - T_\text{out}}{T_\text{in}} \left(L_v E + \Delta \mathcal{G} \right) \tag{3.52}$$

$$\approx \frac{T_\text{in} - T_\text{out}}{T_\text{in}} L_v E \quad , \tag{3.53}$$

where L_v is the enthalpy of vaporisation of water. The Gibbs penalty term can be neglected, given that $\frac{R_v T_\text{out}}{L_v} \approx 0.05$. Combining Equations 3.51 and 3.53:

$$\Delta \mathcal{G} \approx - \frac{R_v T_\text{out} T_\text{in}}{L_v (T_\text{in} - T_\text{out})} \ln \mathscr{H}_\text{in} W_{TdS} \tag{3.54}$$

Values of 295 K for T_in and 280 K for T_out can be obtained from the model (or even by inspection of Figure 3.6c) which shows values for the RCE case, but which will also be typical for the aggregate system). An average value for $\mathscr{H}_\text{in}$ is more problematic to define, but using 60% is consistent with model results given the weighting that the log function will give to lower values and the observed values of $\Delta \mathcal{G} \approx 0.5 W_{TdS}$.

It is possible to develop Equation 3.54 further by making use of the Clausius-Clapeyron relation

in the form $\frac{de_s}{e_s} = \frac{L_v dT}{R_v T^2}$:

$$\frac{\Delta \mathcal{G}}{W_{TdS}} \approx -\frac{R_v T_{\text{out}} T_{\text{in}}}{L_v(T_{\text{in}} - T_{\text{out}})} \ln \mathcal{H}_{\text{in}} \quad , \tag{3.55}$$

$$\approx \frac{\ln \mathcal{H}_{\text{in}}}{\ln \frac{e_{s,\text{out}}}{e_{s,\text{in}}}} \quad , \tag{3.56}$$

where $e_{s,\text{in}}$ and $e_{s,\text{out}}$ are the saturated vapour pressures of water at temperatures T_{in} and T_{out}. Defining $r_{v,\text{in}}$ as the vapour mixing ratio corresponding to $\mathcal{H}_{\text{in}}$ at temperature T_{in} and dry pressure $p_{d,\text{in}}$:

$$\frac{\Delta \mathcal{G}}{W_{TdS}} = \frac{\ln \frac{R_v r_{v,\text{in}} p_{d,\text{in}}}{R_d e_{s,\text{out}}} + \ln \frac{e_{s,\text{out}}}{e_{s,\text{in}}}}{\ln \frac{e_{s,\text{out}}}{e_{s,\text{in}}}} \quad , \tag{3.57}$$

Now introduce $r_{vs,\text{out}}$ via $e_{s,\text{out}} = R_v/R_d p_{d,\text{out}} r_{vs,\text{out}}$ where $p_{d,\text{out}}$ is the partial pressure of dry air at temperature T_{out}. Substituting for $e_{s,\text{out}}$ in the first logarithm in the numerator of Equation 3.57 leads to:

$$\frac{\Delta \mathcal{G}}{W_{TdS}} = 1 - \frac{\ln p_{d,\text{out}}/p_{d,\text{in}}}{\ln e_{s,\text{out}}/e_{s,\text{in}}} - \frac{\ln r_{vs,\text{out}}/r_{v,\text{in}}}{\ln e_{s,\text{out}}/e_{s,\text{in}}} \quad . \tag{3.58}$$

Assuming that $r_{vs,\text{out}} \lesssim r_{v,\text{in}}$ (see Figure 3.6d) to confirm that this is reasonable for all but the shallowest circulations):

$$\frac{\Delta \mathcal{G}}{W_{TdS}} \lesssim 1 - \frac{\ln \frac{p_{d,\text{out}}}{p_{d,\text{in}}}}{\ln \frac{e_{s,\text{out}}}{e_{s,\text{in}}}} \tag{3.59}$$

$$\tag{3.60}$$

Making a Taylor expansion in $\ln(1 + x) \approx x$:

$$\frac{\Delta \mathcal{G}}{W_{TdS}} \lesssim 1 - \frac{\frac{\Delta z}{H_{pd}^*}}{\frac{\Delta z}{H_{es}^*}} \tag{3.61}$$

$$\lesssim 1 - \frac{H_{es}^*}{H_{pd}^*} \tag{3.62}$$

$$\lesssim 1 - \frac{R_v g \bar{T}}{R_d L_v \Gamma} \quad , \tag{3.63}$$

where Δz is the height difference between the in and out states, and $H_{es}^* = \frac{-R_v \bar{T}^2}{L_v \Gamma}$, $H_{pd}^* = \frac{R_d \bar{T}}{g}$

are the scale heights for saturated vapour pressure and the partial pressure of dry air, $\bar{T}$ is an average temperature over the cycle between T_{in} and T_{out} and Γ is the atmospheric lapse rate. Using $\bar{T} = 290$ K and $\Gamma = -5 \text{ km}^{-1}$ gives $\frac{\Delta \mathcal{G}}{W_{Tds}} < 0.64$. This ratio will decrease as $\frac{r_{v,\text{out}}}{r_{v,\text{in}}}$ decreases, i.e. as the temperature difference between the "in" and "out" states increases.

The correction term discussed in section 3.5, expressed as in Equation 3.34 will scale as approximately 20% of W_p, depending on the relationship between the lapse rate of the reference state Γ and the dry adiabatic lapse rate $\frac{g}{c_p}$, where c_p is the specific heat capacity of dry air at constant pressure, or some 5% of W_{Tds}. In view of the approximate nature of these scalings it is not considered further in this section.

Combining these various elements as in Equation 3.37, one can expect the efficiency with which such a system generates mechanical work W_b to be typically 20% of the Carnot maximum W_{Tds}. The values shown for the total system in Figures 3.16, 3.20 and 3.21 are consistent with these estimates.

The Gibbs penalty component for the large-scale circulation is closely linked to the moisture transport between the two columns (here expressed as the latent heat transport), as will be seen in Figure 3.23.

(a) τ sensitivity $\qquad$ (b) ΔT_s sensitivity $\qquad$ (c) ϵ sensitivity
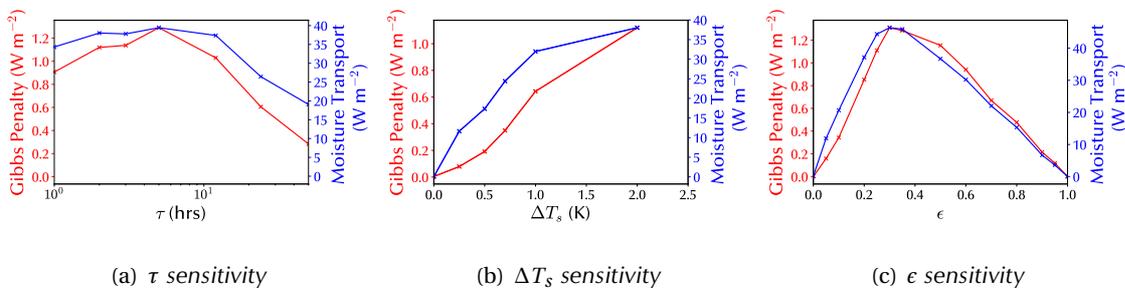
Figure 3.23: *Large-scale Gibbs penalty (red) and moisture transport between the two columns (blue) for the experiments described in sections 3.9-3.11.*

The relationship between these two quantities can be explained by Equation 3.51:

$$\Delta\mathcal{G} \approx -R_v\,T_{\text{out}}\frac{\Delta r_v}{\Delta t}\ln\mathcal{H}_{\text{in}} \quad, \tag{3.64}$$

$$\approx \frac{-R_v}{L_v}T_{\text{out}}\ln\mathcal{H}_{\text{in}} \times \text{latent heat transport} \quad. \tag{3.65}$$

This reflects the fact that the majority of the moisture input for the large-scale circulation arises through evaporation in the cool region and that this is transported into the warm region for use. Using $T_{\text{out}} = 285$ K and $\mathcal{H}_{\text{in}} = 60\%$ as before provides a good fit.

3.13   ENERGY BALANCE

As already discussed in section 3.2, the LEM does not explicitly conserve energy. It is nonetheless instructive to examine the energetic inputs and outputs into the system, for the two regions. Figure 3.24 shows these for the experiment described in section 3.9. Specifically it shows the latent heat and sensible heat inputs into the two regions, the precipitation in each region (converted into energy units) and the radiation emitted. Whilst the first three quantities are directly diagnosed by the LEM, the radiation emitted can be calculated from the mean sea level pressure in each region, given the fixed cooling profile using the expression:

$$\text{Rad} = (\text{MSLP} - 170\,\text{hPa}) \times \frac{c_p \times 1.5\,\text{K}\,\text{day}^{-1}}{g \times 24 \times 3600} \quad . \tag{3.66}$$

There is a significant imbalance between the two regions - which increases with increased coupling (Figure 3.24 e). This is largely driven by the increased effect of evaporation in the warm region (and conversely in the cool region), but a significant contribution comes from the moisture transport between the two regions. Taken as a whole, the system is very close to being in energetic balance.

This last result is surprisng - one could have hoped that the energy inputs into the entire system exceeded the radiative output by the amount of mechanical work done, since the dissipation that acts as a sink for the kinetic energy does not in turn give rise to heating in the LEM. We also note that the imbalance calculated using evaporation as an input is slightly lower than based on condensation (i.e. precipitation). These results can be explained by the fact that the energy imbalance is calculated as the difference of two relatively large numbers and can thus be greatly influenced by a relatively small error in one of them, and as already mentioned, the LEM does not explicitly conserve energy. It is also relevant to note that the model is not in equilibrium above 14 km (as seen in Figure 3.1), which will account for 'leakage' of approximately $1.5\,\text{W}\,\text{m}^{-2}$.

(a) *Latent heat input (evaporation)*

(b) *Sensible heat input*

(c) *Latent heat input (precipitation)*

(d) *Radiation output*

(e) *Energy imbalance in each region and for total system*

(f) *Energy imbalance for total system*
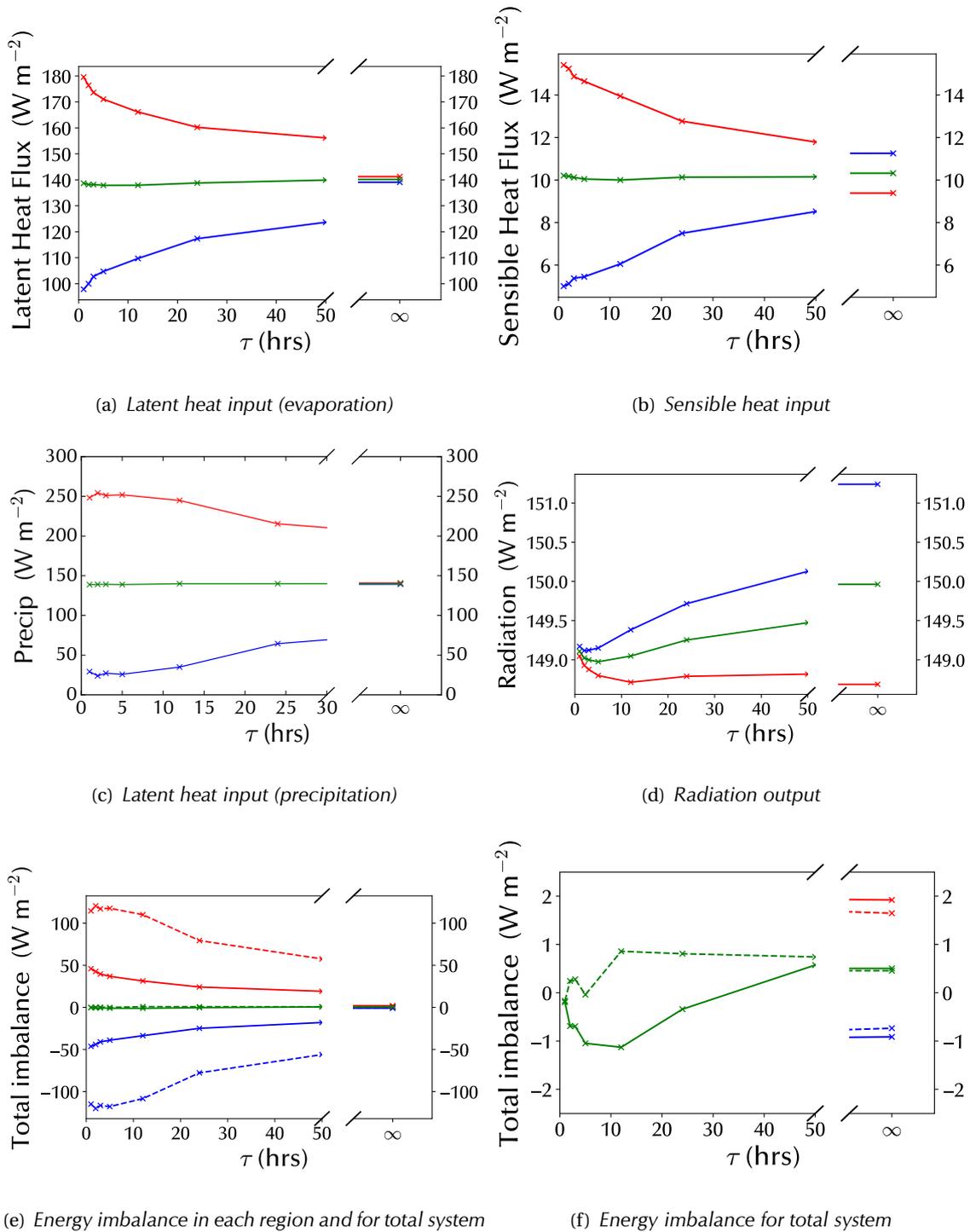
Figure 3.24: *Components of energy input and output for cool region (blue), warm region (red) and total system (green). The energy imbalance plots show both values calculated using latent heat evaporated into each region (dashed lines) and precipitated out of each region (solid lines). The SST difference between the two regions is 2K and they are of equal area ($\epsilon = 0.5$).*
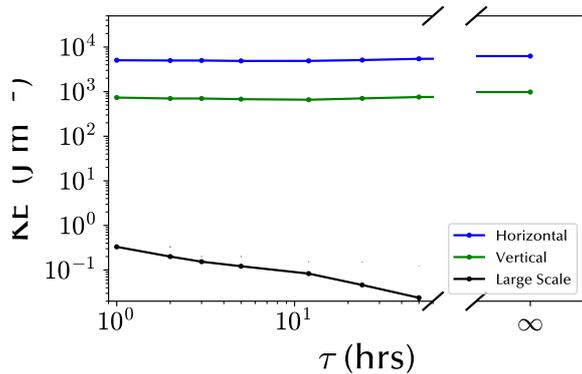
Figure 3.25: *Horizontal (blue), total vertical (green) and large-scale vertical (black) components of kinetic energy for varying values of τ ($\epsilon = 0.5$, $\Delta T_s = 2$ K).*

3.14 KINETIC ENERGY AND WORK DONE

The kinetic energy associated with the various components of motion in the system are shown in Figure 3.25. It will be seen that the large-scale component is some 3 orders of magnitude smaller than the total vertical kinetic energy, which in turn is one order of magnitude less than the horizontal component (although it should be remembered that the model is 2 dimensional).

The disparity between the large-scale and total vertical kinetic energy can be contrasted with the relative values of the components of work done associated with the large-scale and total system (Figure 3.16) which are much closer. This arises from the fact that much of the motion within the columns is of little thermodynamic consequence - as the upward and downward convective motions are at very similar values of B and r_T. Figure 3.26 shows the contributions to the vertical mass flux from the upward and downward motions in each of the columns and for the large-scale. We can see that each of the upward and downward plots are dominated by values located close to the mean θ_e at each height but that these largely cancel out to produce the upward and downward mass flux plots that have been used to obtain the convective streamfunctions. However, from a kinetic energy perspective these convective motions will not cancel out - indeed they will dominate the result.
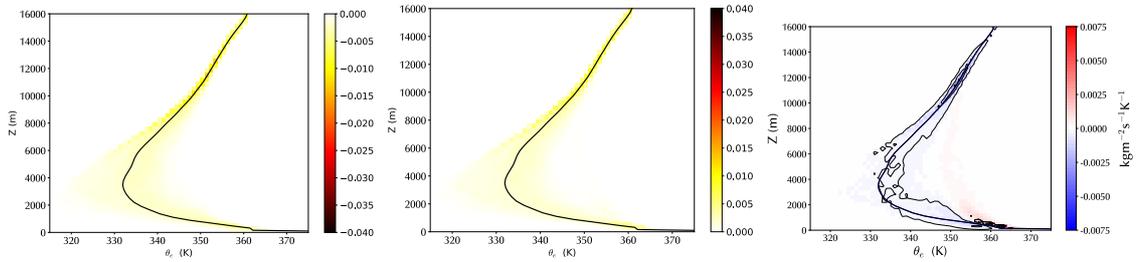
(a) *Downward vertical mass flux for cool region*

(b) *Upward vertical mass flux for cool region*

(c) *Total vertical mass flux for cool region*
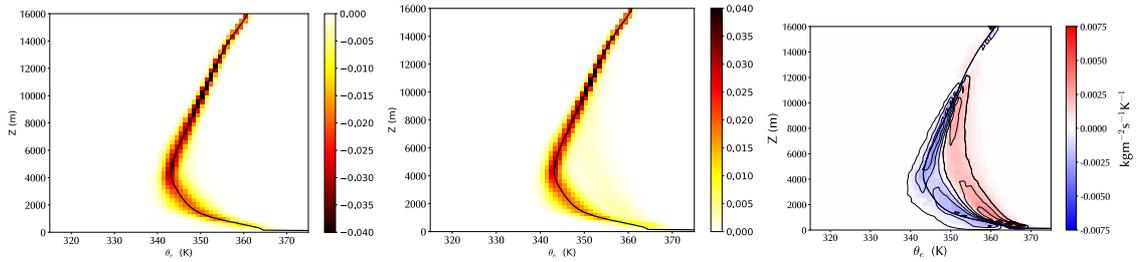
(d) *Downward vertical mass flux for warm region*

(e) *Upward vertical mass flux for warm region*

(f) *Total vertical mass flux for warm region*

(g) *Downward vertical mass flux for large-scale circulation*
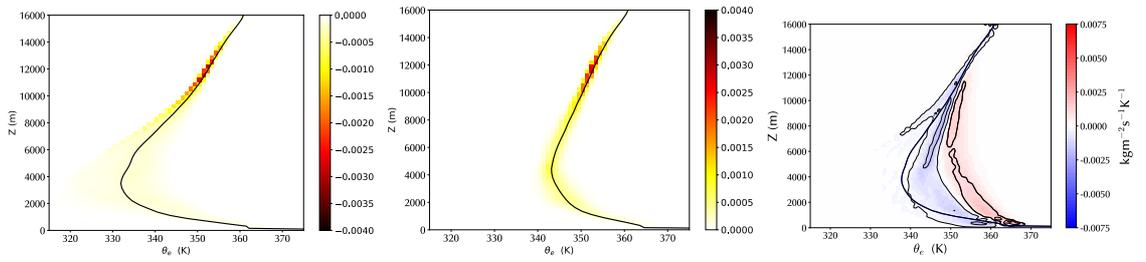
(h) *Upward vertical mass flux for large-scale circulation*

(i) *Total vertical mass flux for large-scale circulation*

Figure 3.26: *Upward, downward and total components of vertical mass flux for each of the regions and the large-scale circulation for two coupled regions ($\tau = 2$ hrs, $\epsilon = 0.5$, $\Delta T_s = 2$ K).*

3.15 WEAK PRESSURE GRADIENT APPROXIMATION COUPLING

A number of experiments were carried out with this model, but using the WPG approximation to determine the large-scale circulation. The WPG coupling was implemented as described in section 2.12, with the same parameters of $\epsilon_{\text{WPG}} = 1$ day $^{-1}$ for the damping and $k = 10^{-6}$ m^{-1} for the wavenumber, with vertical velocities recalculated every 10 minutes. Runs were performed for the standard configuration of the two models, with $\epsilon = 0.5$ and $\epsilon = 0$ (similar to coupling to a reference column). The mean potential temperature difference between the two regions and the large-scale vertical velocity in the warm region are shown for the $\epsilon = 0.5$ case in Figure 3.27, together with comparable values from a similar run where the regions are coupled with the WTG approximation with timescale parameter $\tau = 2$ hours, averaged as before over the last 100 days of a 120 day run.

(a) *Mean θ difference* (b) *Vertical velocity*
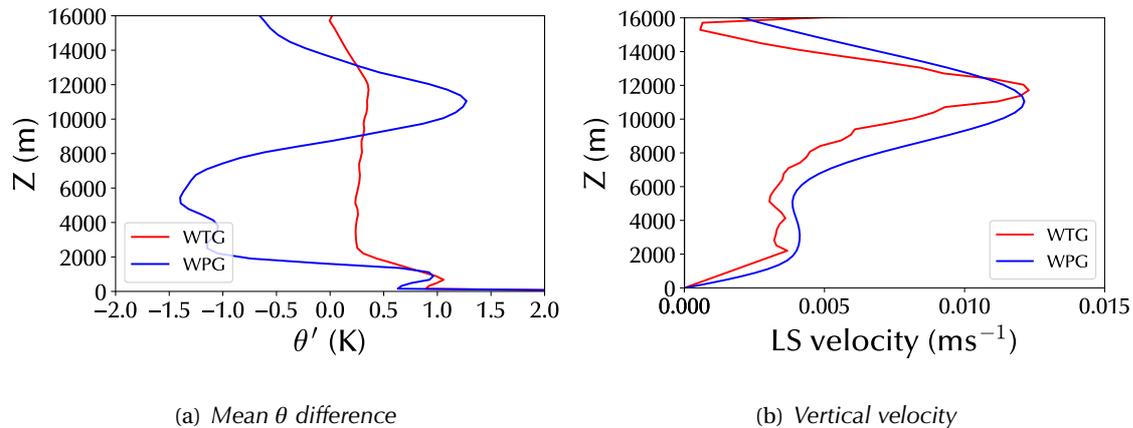
Figure 3.27: *Comparison of a) mean potential temperature difference between regions and b) large-scale vertical velocity in warm region compared for WPG coupling (blue) and WTG (red) ($\epsilon = 0.5$, $\Delta T_s = 2$ K).*

It will be observed that the WPG-coupled system produces a smoother velocity profile, as might be expected given the fact that this velocity is the solution of a second-order partial differential equation. The top-heaviness of the WTG approximation when compared with the WPG approximation that was mentioned in section 1.5 is not observed here. The mean potential temperature difference is less satisfactory, with the cool region actually warmer than the warm region for much of the troposphere (this characteristic also occurs, albeit to a lesser

degree, if virtual potential temperature is analysed). In fact, closer analysis shows that the large-scale velocity in a WPG-coupled system for $\epsilon = 0.5$ oscillates between two unstable solutions - one with wave-number 1 and one with wave-number 2, which involves changes of sign of w. Figure 3.28 illustrates this for a sequence of 100 coupling time-steps early on in a simulation (the large-scale velocity is recalculated every 10 minutes, whereas the model time-step is determined by the CFL criteria but is generally of the order of 100 s). This feature arises when $\frac{\partial w}{\partial z}$ becomes too negative at higher altitudes, and results in excess warming of the cool region, which is advected down and results in a cool region which is warmer than the 'warm' region. This can also be verified by comparing the large-scale velocity resulting from a coupled run with $\epsilon = 0.5$ with a similar run, but where the cool region is fixed to be the time-mean of the cool region in the coupled region run (Figure 3.29). Velocity profiles for the limiting case of $\epsilon = 0$ for both a coupled region and fixed cool configuration are also shown, where the difference between the two is not significant. It may well be that this feature is related to the oscillatory behaviour described in Edman and Romps (2014) and that the modification to the WPG approximation that they propose to reflect how perturbations in a column affect its immediate environment would eliminate it.
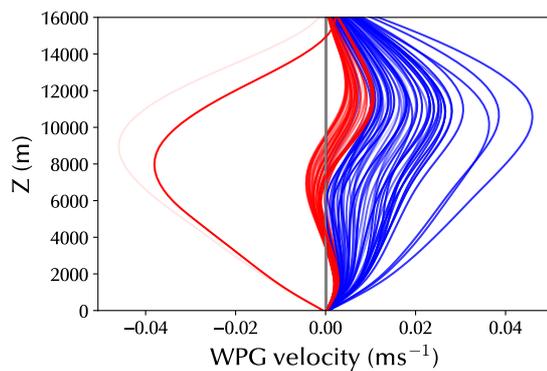
Figure 3.28: *Profiles of large-scale vertical velocity for a series of 100 time periods for run with WPG coupling. Blue lines represent solutions where w_{WPG} in the warm region remains positive at all levels. The earliest time periods are shown by faint lines which become bolder over the 100 periods.*
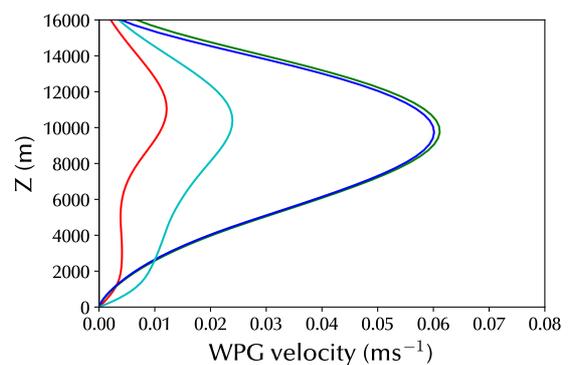
Figure 3.29: *Profiles of large-scale vertical velocity in the warm column for two regions coupled using the WPG - with $\epsilon = 0.5$ (red) and $\epsilon = 0.0$ (green). Profiles where the cool region is fixed as the mean cool region in a coupled run are also shown for $\epsilon = 0.5$ (cyan) and $\epsilon = 0.0$ (blue).*

Values for the components of work done were calculated for these two sets of runs, and are shown in Figure 3.30. This shows that whilst the totals are largely unchanged, WPG coupling has the effect of reducing the work done in the cool region and increasing the work done by the large-scale circulation for the moisture-related components when compared with WTG coupling. This suggests a greater degree of drying out of the cool region which is confirmed by a comparison of column integrated water vapour content in Figure 3.31. This was not investigated further.

(a) *Total*

(b) *Large-scale*

(c) *Cool region*
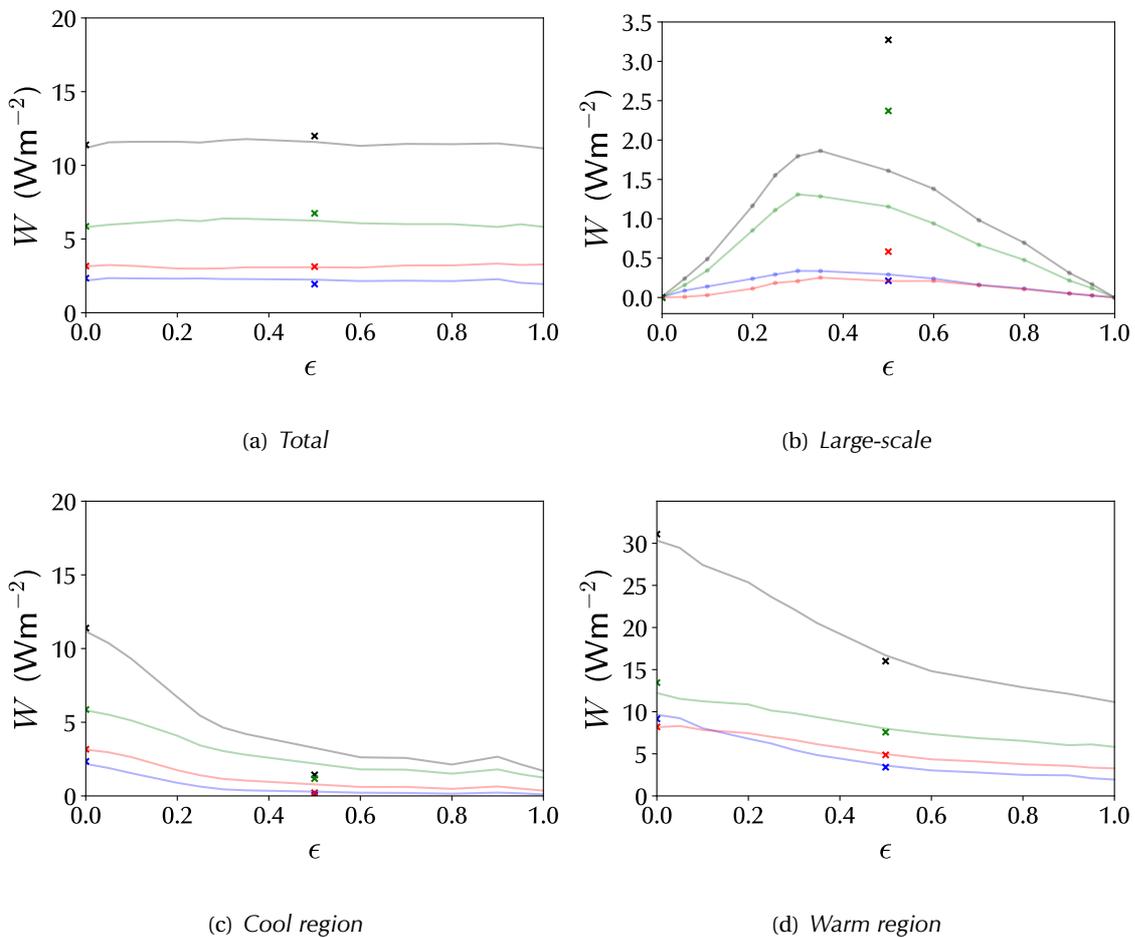
(d) *Warm region*

**Figure 3.30:** *Components of Equation 3.37 for two regions coupled using the WPG (shown as crosses) for (a) the total system, (b) the large-scale circulation and (c) (d) the residual circulations in the cooler and warmer regions for varying relative sizes of the two regions. Blue indicates W_b, red W_p, green ΔG^* and black W_{Tds}. Comparable values for a WTG coupled system with $\tau = 2hrs$ are shown as faint lines.*
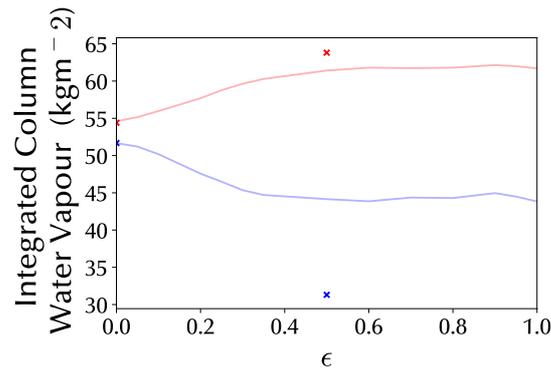
Figure 3.31: *Integrated column water vapour content in warm region (red) and cool region (blue) for WPG coupled regions. Comparable values for a WTG coupled system with $\tau = 2hrs$ are shown as faint lines.*

3.16 MISCELLANEOUS SENSITIVITIES

A common choice for the Smagorinsky basic mixing length for three-dimensional turbulence in the inertial sub-range is 0.23 of the grid separation. This would correspond to 115 m here, as opposed to the 250 m preferred by Daleu et al. (2012) and as used in the runs hitherto discussed. Components of work done for a run for a single uncoupled column for each of these mixing lengths are shown in Table 3.6, and those for a coupled run with $\tau = 2$ hours, $\epsilon = 0.5$ are shown in Tables 3.7 and 3.8. Although the change in mixing length does have an effect on the thermodynamic budget, it is not so large as to cast doubt on any of the conclusions of this study, particularly as the choice of mixing length for an LEM run in two-dimensional CRM mode is to some extent debatable.

$(\mathrm{W\,m^{-2}})$	W_{Tds}	W_b	W_p	$\Delta\mathcal{G}$	Correction	Δ^*
Mixing length 250 m	11.17	2.18	3.14	6.32	-0.51	0.04
Mixing length 115 m	11.44	2.20	3.27	6.45	-0.52	0.04

Table 3.6: *Components of work done for a single region in RCE for different values of the Smagorinsky mixing length.*

(W m^{-2})	W_{Tds}	W_b	W_p	$\Delta\mathcal{G}$	Correction	Δ^*
Cool region	2.91	0.18	0.66	2.22	-0.15	-0.01
Warm region	17.30	3.70	5.20	9.04	-0.79	0.15
Large Scale	1.85	0.33	0.24	1.29	-	-0.01
Total	11.95	2.27	3.17	6.92	-0.47	0.06

Table 3.7: *Components of work done for two coupled regions in the control configuration for a Smagorinsky mixing length of 115 m.*

(W m^{-2})	W_{Tds}	W_b	W_p	$\Delta\mathcal{G}$	Correction	Δ^*
Cool region	2.91	0.24	0.69	2.13	-0.14	-0.01
Warm region	16.39	3.40	4.93	8.67	-0.78	0.17
Large Scale	1.72	0.39	0.39	1.12	-	0.00
Total	11.37	2.13	3.11	6.53	-0.46	0.07

Table 3.8: *Components of work done for two coupled regions in the control configuration for a Smagorinsky mixing length of 250 m.*

A number of studies use a variant of the WTG where θ is replaced in the expression for w_{LS} by θ_v thus:

$$w_{LS}\frac{\partial \theta_v}{\partial z} = \frac{\theta_v'}{\tau} \quad . \tag{3.67}$$

A sensitivity experiment was run with this form of coupling, which can be referred to as the Weak virtual Temperature Gradient (WvTG) approximation. It was found that using τ =2 hours introduced stability issues, so a run with τ = 6hrs was used instead - the components of work done for this case are shown in Table 3.9. For comparison, values for the standard WTG for values of τ = 2 hours and τ = 5 hours are shown in Tables 3.10 and 3.11.

(W m^{-2})	W_{Tds}	W_b	W_p	$\Delta\mathcal{G}$	Correction	Δ^*
Cool region	2.29	0.14	0.49	1.78	-0.11	-0.01
Warm region	16.04	3.32	4.80	8.55	-0.75	0.12
Large Scale	2.60	0.44	0.39	1.74	-	0.03
Total	11.77	2.17	3.03	6.91	-0.43	0.08

Table 3.9: *Components of work done for two coupled regions run with Weak virtual Temperature Gradient coupling, $\tau = 6$ hours.*

(W m^{-2})	W_{Tds}	W_b	W_p	$\Delta\mathcal{G}$	Correction	Δ^*
Cool region	2.91	0.24	0.69	2.14	-0.15	-.01
Warm region	16.39	3.40	4.93	8.67	-0.78	0.17
Large-Scale	1.72	0.30	0.30	1.12	-	0
Total	11.37	2.13	3.11	6.53	-0.46	0.07

Table 3.10: *Components of work done for two coupled regions run with WTG coupling with $\tau = 2$ hours.*

(W m^{-2})	W_{Tds}	W_b	W_p	$\Delta\mathcal{G}$	Correction	Δ^*
Cool region	3.32	0.27	0.79	2.45	-0.17	-0.01
Warm region	15.79	3.26	4.80	8.34	-0.76	0.15
Large Scale	4.10	0.91	0.62	2.58	-	-0.01
Total	11.61	2.22	3.10	6.68	-0.46	0.06

Table 3.11: *Components of work done for two coupled regions run with WTG coupling with $\tau = 5$ hours.*

Comparison of the results summarised in these tables suggests that the Weak virtual Temperature Gradient approximation has a stronger effect on the components of work done in each of the two regions relative to the uncoupled state than the Weak Temperature Gradient approximation for the same values of τ. This can be explained by the fact that the vertical velocity will be determined to first order by the sum of the temperature difference between the two regions and the difference in water vapour mixing ratio (multiplied by temperature). As vertical velocities increase, they eliminate the temperature contrast between the regions, but stronger circulation also increases the drying-out of the cool region. Figure 3.32 shows a plot of the re-

lationship between θ' and θ'_v for the control case at various heights. It will be seen that within the boundary layer θ'_v is significantly greater than θ', by up to a multiple of 3 - justifying the use of $\tau = 5$ hours for the WvTG-coupled run. Above the boundary layer θ'_v decreases significantly as moisture contrasts reduce, even though θ' increases with height, due to warming of the warm region due to condensation. Above a certain level the moisture contrast is no longer significant and the two quantities are equal.
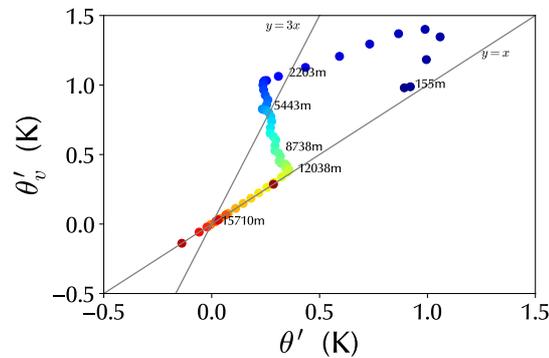

Figure 3.32: *Virtual potential temperature and temperature difference between the two regions for the control case - warmer colours indicate increasing heights, selected heights are labelled.*

For completeness, the regions were also coupled using a Weak Pressure Gradient approach with T substituted for T_v in Equation 2.137, which is of questionable physical significance. The components of work done as shown in Table 3.12, which can be compared with the standard WPG approximation results in Table 3.13. As the results from the WTG and WvTG experiments would suggest, basing the WPG approximation on temperature whilst leaving other parameters unchanged has a weaker effect on the components of work done in each of the two regions relative to the uncoupled state.

(W m^{-2})	W_{Tds}	W_b	W_p	$\Delta\mathcal{G}$	Correction	Δ^*
Cool region	2.30	0.13	0.47	1.84	-0.11	-0.02
Warm region	15.65	3.28	4.74	8.22	-0.73	0.14
Large Scale	2.58	0.46	0.41	1.64	-	0.07
Total	11.55	2.16	3.01	6.67	-0.42	0.13

Table 3.12: *Components of work done for two coupled regions run with the WPG approximation based on temperature differences.*

(W m^{-2})	W_{Tds}	W_b	W_p	$\Delta\mathcal{G}$	Correction	Δ^*
Cool region	1.43	0.04	0.47	0.22	-0.06	0.00
Warm region	16.01	3.41	4.87	8.32	-0.75	0.15
Large Scale	3.27	0.21	0.58	2.37	-	0.11
Total	11.99	1.94	3.13	7.15	-0.40	0.18

Table 3.13: *Components of work done for two coupled regions run with the WPG approximation based on virtual temperature differences.*

3.17 UNPARAMETRISED COUPLING

Although the main aim of this thesis is the study of parametrised large-scale circulations, a numerical experiment was also performed in which such a circulation is allowed to develop within a CRM without parametrisation. Instead of the standard configuration of two 2-D models with 256 horizontal grid points, with an SST difference between the two, the CRM was run with 512 horizontal grid points, but with an increase in SST from 302.7 K to 304.7 K at the half-way point. This can be regarded as representing a meso-scale system, rather than the large-scale circulations that are discussed elsewhere in this thesis.

The $\log_{10}$ of the mass density distribution in (θ_e, z) space and the convective vertical mass flux for the two regions are shown in Figure 3.33. It will be noted that the cool region is now very dry indeed, and that net vertical motion appears to be quite weak in the warm region (relative to the single region model), and limited to slow subsidence in the cool region. This is confirmed by the values of the components of the mechanical energy budget (Table 3.14).

(a) *Log₁₀ mass density distribution - cool region*

(b) *Log₁₀ mass density distribution - warm region*

(c) *Vertical mass flux - cool region*

(d) *Vertical mass flux - warm region*
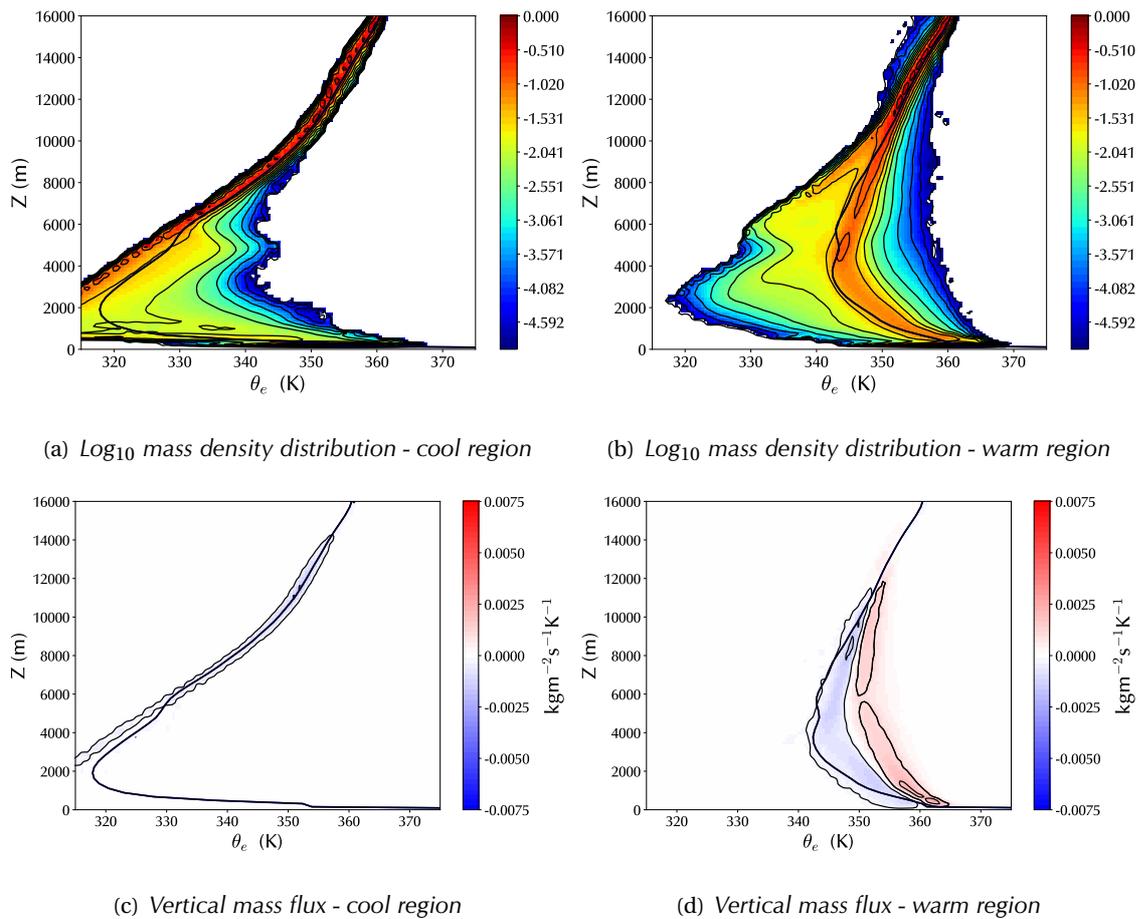
Figure 3.33: *Results for cool and warm regions for unparametrised coupling.*

Further insight can be obtained from some of the diagnostics plotted in Figure 3.34. It will be seen that the effect of the relatively strong circulation generated is indeed to dry out the cool region, which as a result of the subsiding air becomes warmer than the warm region. However, the virtual temperature in the warm region remains higher than in the cool region, consistent with the upward motion shown. The large SST change over a relatively small distance would represent much stronger coupling than discussed elsewhere in this thesis and further quantitative comparisons are not meaningful.

(W m^{-2})	W_{Tds}	W_b	W_p	$\Delta\mathcal{G}$	Correction	Δ^*
Cool region	0.21	0.01	0.03	0.17	-	-
Warm region	7.47	1.21	2.23	4.01	-0.37	0.39
Meso-scale	2.32	0.16	0.43	1.79	-0.11	0.05
Total	6.16	0.77	1.56	3.88	-0.29	0.25

Table 3.14: *Components of work done for explicit representation of a meso-scale circulation.*

3.18 CONCLUSION

In this chapter we have extended and applied the Pauluis thermodynamic diagnostic frameork to the case of two regions, coupled by a parametrised large-scale circulation. In order for the methodology to be applicable, it has been necessary to separate the two region system into three closed circulations - one representing large-scale motions and the other two residual circulations in each of the regions (section 3.8). In addition a minor improvement to Pauluis' equations reflecting the anelastic nature of the LEM was introduced (section 3.5) and standard errors estimated.

This methodology was used to investigate the work done by the total system and each of its components for regions coupled with the WTG approximation. We found that the thermodynamic features of the total system were insensitive to changes in coupling strength (section 3.9), to the temperature difference between the two regions (section 3.10) and also to the relative sizes of the two regions (section 3.11). This suggests that a WTG coupling does not introduce any thermodynamic distortions into the total system (at least in the absence of interactive radiation) although the impact on any of the individual components can be significant.

Some further scalings were developed for the components of work done for a convecting system (section 3.12) - in particular it was shown that in cases where the buoyancy effects are dominated by water vapour content contrasts one can expect the generation of mechanical work by the system to be some 20% of the Carnot maximum, and a relationship between the large-scale Gibbs penalty to the moisture transport between the two regions was identified.

(a) *Temperature difference between regions*

(b) *Water vapour content*

(c) *Virtual temperature difference between regions*

(d) *Large-scale velocity*
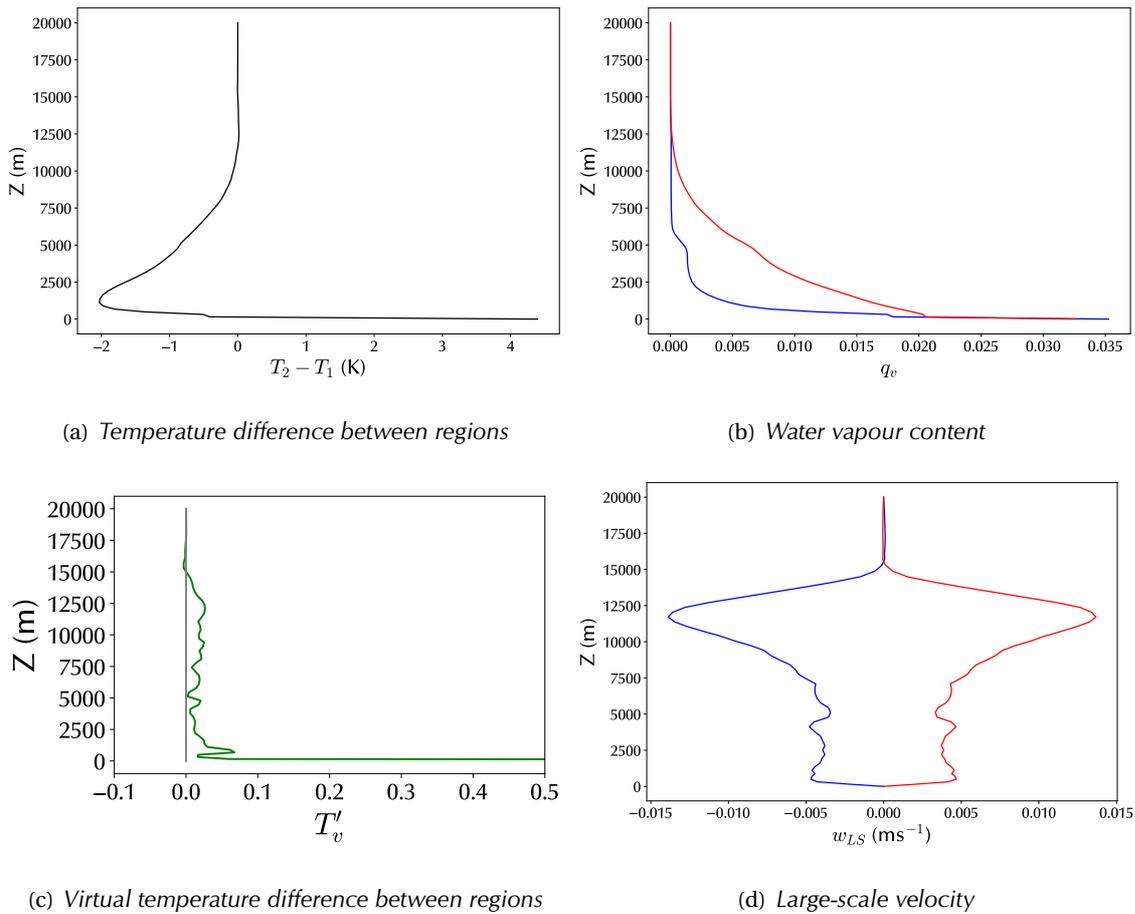
Figure 3.34: *Selected diagnostics for cool (blue) and warm (red) regions for un-parametrised coupling*

In section 3.14 we showed that the large-scale circulation generates a disproportionate amount of work relative to its kinetic energy when compared with the system as a whole and that much of the convective motion within each of the regions has relatively weak thermodynamic consequences.

In section 3.15 we applied the approach to two regions coupled by a damped gravity wave circulation, and showed how oscillatory behaviour can arise which makes the DGW approach less suitable for coupled-region studies. Results of a number of other sensitivity runs are shown in section 3.16, including one which suggests that the use of a variant of the WTG based on virtual temperature can produce much stronger coupling than a WTG with the same parameters.

Finally, an attempt was made to explicitly represent a coupling between two regions without the use of parametrisations; this produces a very strong meso-scale circulation which leaves a very dry cool region, and suppresses convection in both regions.

CHAPTER 4

APPLICATION TO RE-ANALYSIS FOR TROPICAL PACIFIC DURING YEAR OF TROPICAL CONVECTION

4.1 INTRODUCTION

In the two previous chapters we have used two models, one that is relatively simple and analytically tractable and the other more sophisticated, in order to better understand the drivers of the generation of mechanical work by idealised tropical circulations. However, the ultimate value of that work will lie in its relevance to real-world phenomena. With that aim in mind, we now apply the diagnostic framework that we developed in those chapters to re-analysed data, in particular to estimate the mechanical work generated by overturning circulations in the tropical Pacific during the Year of Tropical Convection (YoTC) field campaign.

This topic has attracted recent attention from other researchers. Huang and McElroy (2014) have estimated the conversion from APE to kinetic energy for the Hadley circulation, and Veiga et al. (2013) have performed a similar analysis for the Walker cell during various phases of the El Nino Southern Oscillation, but neither of these studies have analysed the components of the Pauluis mechanical energy budget.

Waliser et al. (2012) provides an overview of the climatic conditions during the 24 month period referred to as the YoTC. Figure 1 from that paper (two panels reproduced below as Figure 4.1) shows SST anomalies in the tropical Pacific Ocean during the period of the project, and
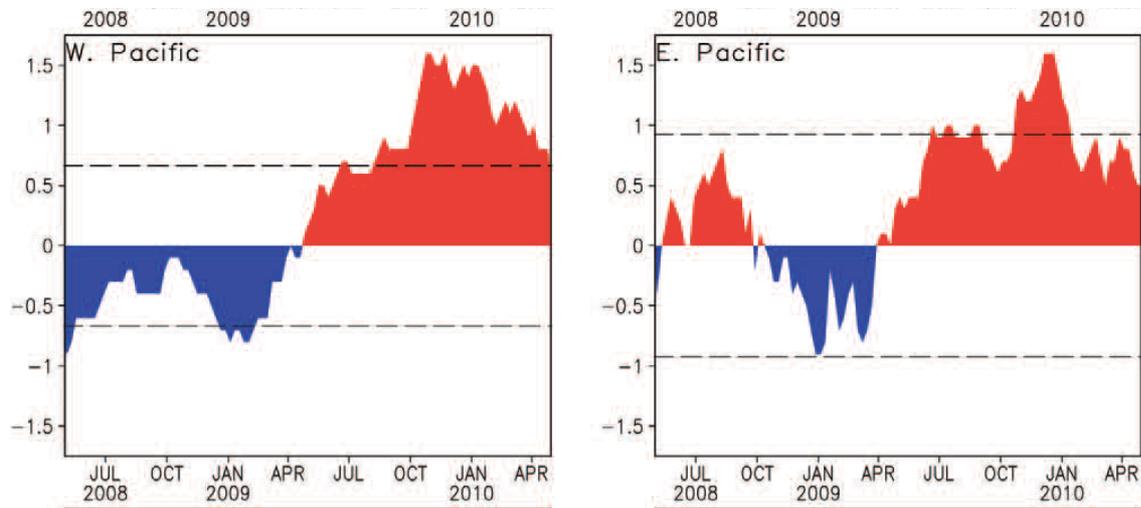
Figure 4.1: *SST anomalies (°C) during the YoTC period for the west Pacific Ocean (5°S-5°N,160°E-150°W) and east Pacific Ocean (5°S-5°N,150°W-90°W), reproduced from Figure 1 in Waliser et al. (2012).*

indicates modest La Niña conditions for the first 12 months of the period and modest El Niǹo conditions for the remaining 12 months. The analyses that follow split the period into a La Niña year and an El Niño year accordingly. Waliser et al. (2012) also identified 6 MJO events during the period, three in each year, although those in the El Niño year are somewhat stronger – they remark that this MJO activity overall is relatively weak when compared with the previous 12 years.

We first apply the methodology of Chapter 3 to the circulation within the tropical Pacific zone, using a number of separation criteria for defining zones which are treated as 'cool' and 'warm' regions. We evaluate the mechanical energy budget for convective circulations within these regions and for a large-scale (Walker) circulation between these two regions. There is inflow into and outflow from this tropical Pacific region, and we next evaluate the mechanical energy budget for this external circulation using a number of estimates of the profile of the external

region.

4.2 REANALYSIS DATA SELECTED

The dataset used in this chapter is ERA[1]-Interim, a long-term dataset obtained from observations by data-assimilation techniques that is produced by the European Centre for Medium-range Weather Forecasting (ECMWF) (Berrisford et al., 2009). The main region of interest is the tropical Pacific, here defined as the region bounded by 10° S, 10° N, 100° E and 100° W. This is the definition of the "Tropical Pacific" used by ECMWF, but it will not capture the entirety of the ascending branch of the Walker circulation, particularly in La Niña years. Data was downloaded for this domain at the maximum resolution available, namely at 0.25° horizontally, and at 6 hourly intervals. The period of the study was that covered by the YoTC, i.e. 1st May 2008 - 30th April 2010.

Pressure levels were used as the vertical coordinate and the full number of levels available were downloaded (37, decreasing from 1000 hPa to 100 hPa in 25 hPa steps, except for the range 750 hPa – 250 hPa where the steps become 50 hPa, with a further 10 levels above 100 hPa). The fields downloaded included temperature, water vapour mixing ratio, liquid water mixing ratio, ice mixing ratio and vertical velocity (in ω coordinates). To illustrate the features of the zone being studied, plots of selected fields in (θ_e, z) coordinates for the entire region over the two-year period are shown in Figure 4.2. When compared with Figure 3.2, it will be seen that there is a greater spread of temperatures at a given height, with some cooler air present than in the LEM results. The water vapour mixing ratios are comparable, but those for the other phases of water are very much lower (due at least in part to the sparser grid - note the different scales compared with Figure 3.2 for the liquid and ice mixing ratios). Consequently values of θ_e are somewhat lower than in Figure 3.2 and also exhibit a greater spread. These fields were sufficient to estimate streamfunctions and conditional averages in (θ_e, z) coordinates for the variables required to calculate the components of the mechanical energy budget. In addition, SSTs were downloaded at the same resolution and were used to allocate gridpoints to two regions to define a notional large-scale circulation (see section 4.3).

---

[1] ERA stands for ECMWF Reanalysis

(a) $\log_{10}$ of normalised mass density distribution

(b) Vertical mass flux (mean mass flux at each height removed)

(c) Temperature

(d) Vapour mixing ratio

(e) Liquid mixing ratio

(f) Ice mixing ratio
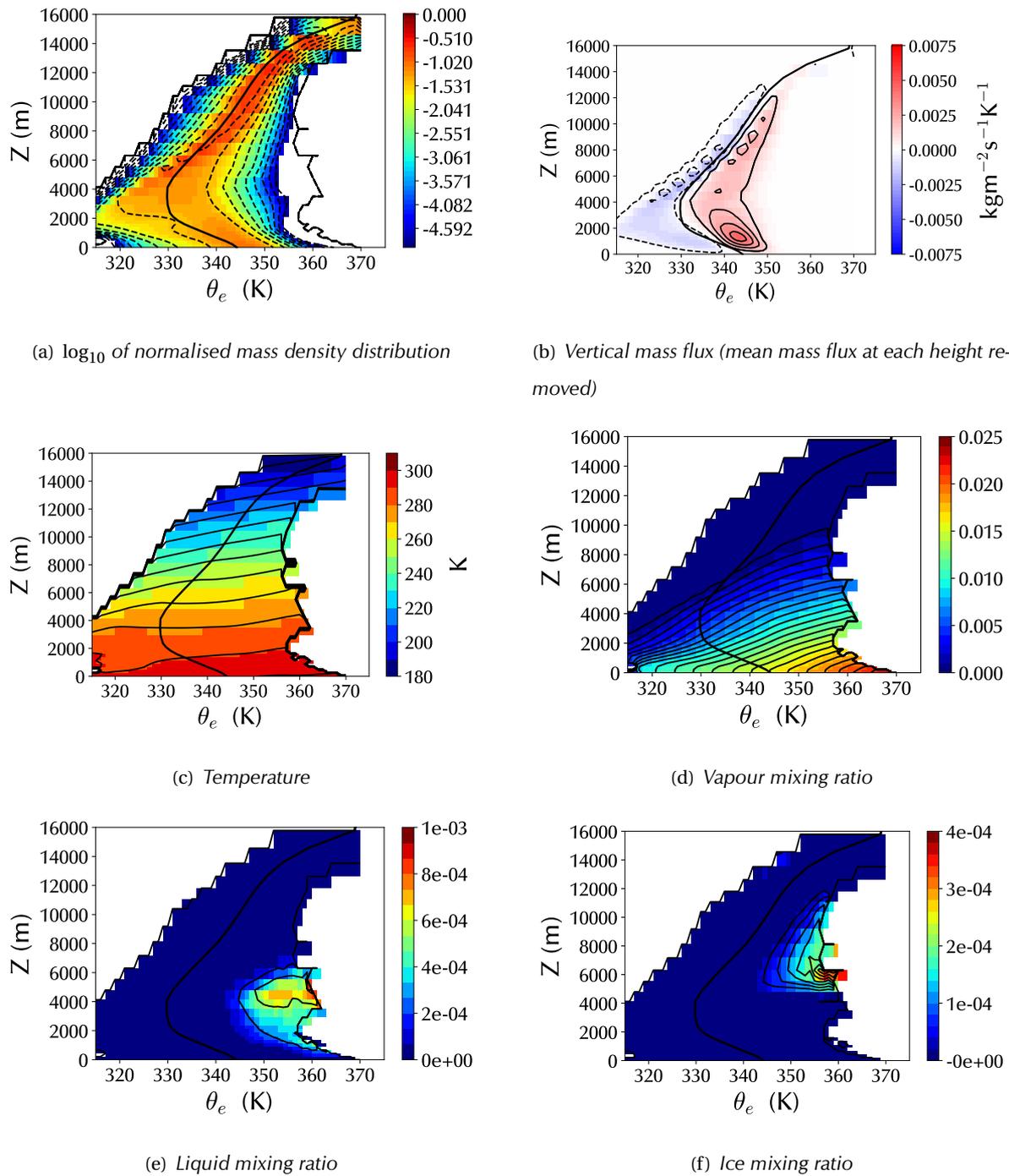
Figure 4.2: Selected fields plotted in isentropic/height coordinates for the tropical Pacific during the 24 month "Year of Tropical Convection".

In addition to the data described above, pressure level data for the entire globe was also extracted in order to develop profiles for areas outside the tropical Pacific. In order to limit the

volumes of data transferred, horizontal resolution was reduced to $1°$ and 12 hourly time intervals. Vertical levels above 100hPa were not downloaded.

4.3 CIRCULATIONS INTERNAL TO ZONE ANALYSED

This section applies the methods developed in chapter 3 to the circulation within the "Tropical Pacific" zone described above. This region is linked to neighbouring regions by in-flow and out-flow at various heights, and in order to develop closed streamfunctions the net average vertical velocity over the entire region is subtracted before the vertical mass fluxes are calculated. This "external" large-scale circulation, which is identified below, is analysed separately in section 4.4.

A number of approaches to identifying the warm and cold regions were applied, namely:

a) based on the **average SST** over each 12 month period for each gridpoint, with **27°C** serving as the cut-off between the two regions;

b) based on the SST at each time period (referred to as **dynamic SST**), with a cut-off of **27°C**; and

c) **dynamic SST** with a cut-off of **28°C.**

For approach a) the average SST was calculated at each grid-point for each of the two years, and this is shown in Figure 4.3 a) and b). For approach b), the proportion of time-periods for which the temperature at each grid-point exceeds the 27°C for each of the years is shown in Figures 4.3 c) and d), and likewise for approach c) the proportion of time-periods for which the temperature at each grid-point exceeds the 28°C for each of the years is shown in Figures 4.3 e) and f) . The relative area (ϵ) taken up by the warm region, the average SST in each region and the SST difference are shown in Table 4.1. Soundings of temperature differences between the regions and specific humidity for method a) are shown in Figure 4.4.

The vertical velocity profiles in each of the two regions for the two years and three different approaches are shown by dashed lines in Figure 4.5. It will be observed that the overall net

vertical velocity in each case is non-zero, implying an exchange of air with external regions at various heights. In order to perform an analysis of the components of the mechanical energy budget this net velocity must be subtracted, and the resulting velocities are shown by solid lines. The work done by the circulation associated with this net velocity, which does not depend on the method used to separate warm and cool regions within the tropical Pacific, is discussed in section 4.4.
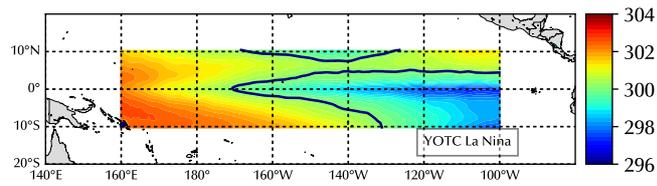
(a) *La Niña, average SSTs, 27°C is marked with the blue contour*
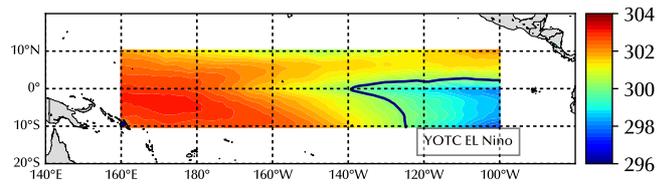
(b) *El Niño, average SSTs, 27°C is marked with the blue contour*
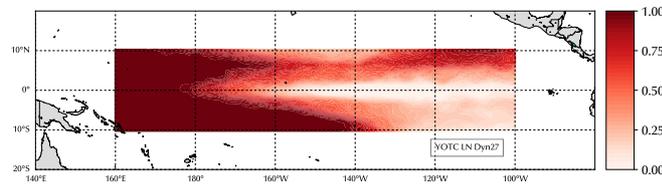

(c) *La Niña, proportion of SSTs that exceed 27°C*
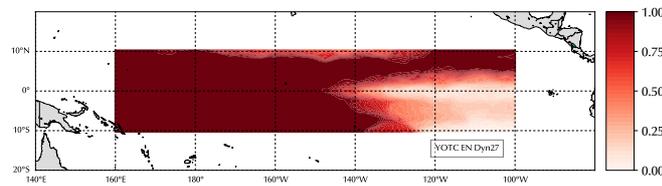
(d) *El Niño, proportion of SSTs that exceed 27°C*
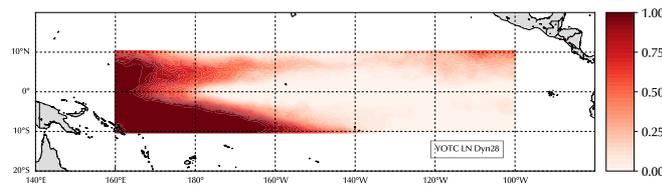
(e) *La Niña, proportion of SSTs that exceed 28°C*
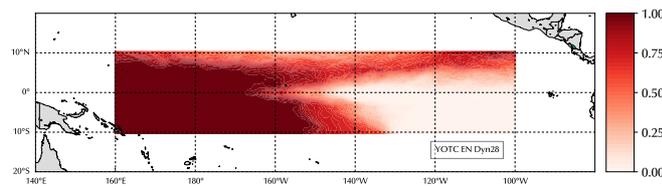
(f) *El Niño, proportion of SSTs that exceed 28°C*

Figure 4.3: *Maps showing average SSTs for a) La Niña and b) El Niño and c) d) e) f) proportion of time that SST exceeds stated temperature in stated year.*

Approach	Year	ϵ	$T_{s,1}$(K)	$T_{s,2}$(K)	ΔT_s(K)
xine Average SST 27°C	La Niña	0.422	299.17	301.18	2.10
Average SST 27°C	El Niño	0.744	299.16	301.79	2.63
Dynamic SST 27°C	La Niña	0.627	298.87	301.30	2.44
Dynamic SST 27°C	El Niño	0.817	298.88	301.88	3.00
Dynamic SST 28°C	La Niña	0.327	299.67	301.88	2.21
Dynamic SST 28°C	El Niño	0.610	299.85	302.27	2.42

Table 4.1: *Relative sizes of warm region (ε), SSTs in warm and cold region and SST difference for different approaches used in this section*

(a) *La Niña, Temperature difference between regions* (b) *La Niña, Specific humidity in cool (blue) and warm (red) regions*

(c) *El Niño, Temperature difference between regions* (d) *El Niño, Specific humidity in cool (blue) and warm (red) regions*
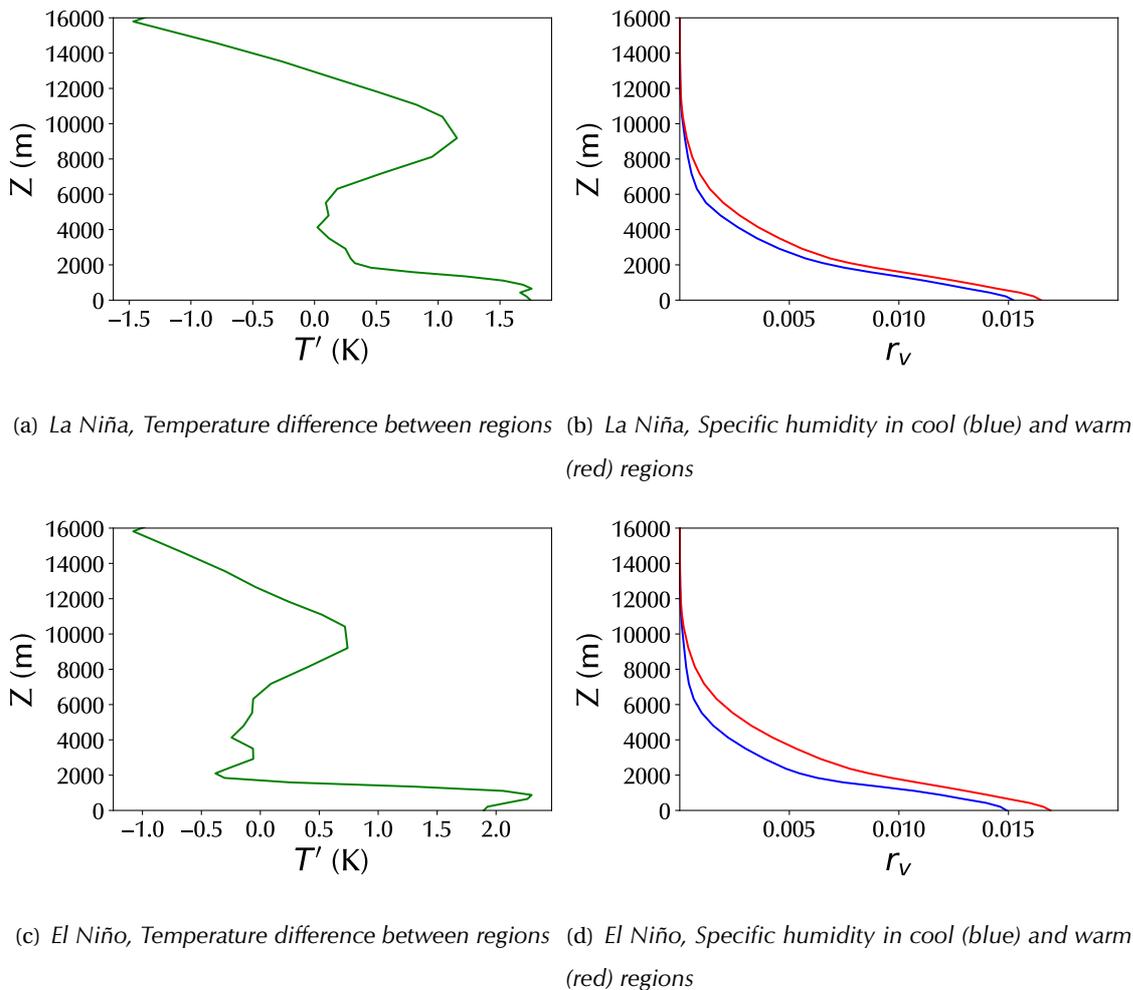
Figure 4.4: *Temperature differences between the regions and specific humidity in each region for method a) Average SSTs compared to 27°C.*

(a) *La Niña, average SSTs (K), 27˚C*

(b) *El Niño, average SSTs (K), 27˚C*

(c) *La Niña, dynamic SSTs 27˚C*

(d) *El Niño, dynamic SSTs 27˚C*

(e) *La Niña, dynamic SSTs 28˚C*

(f) *El Niño, dynamic SSTs 28˚C*
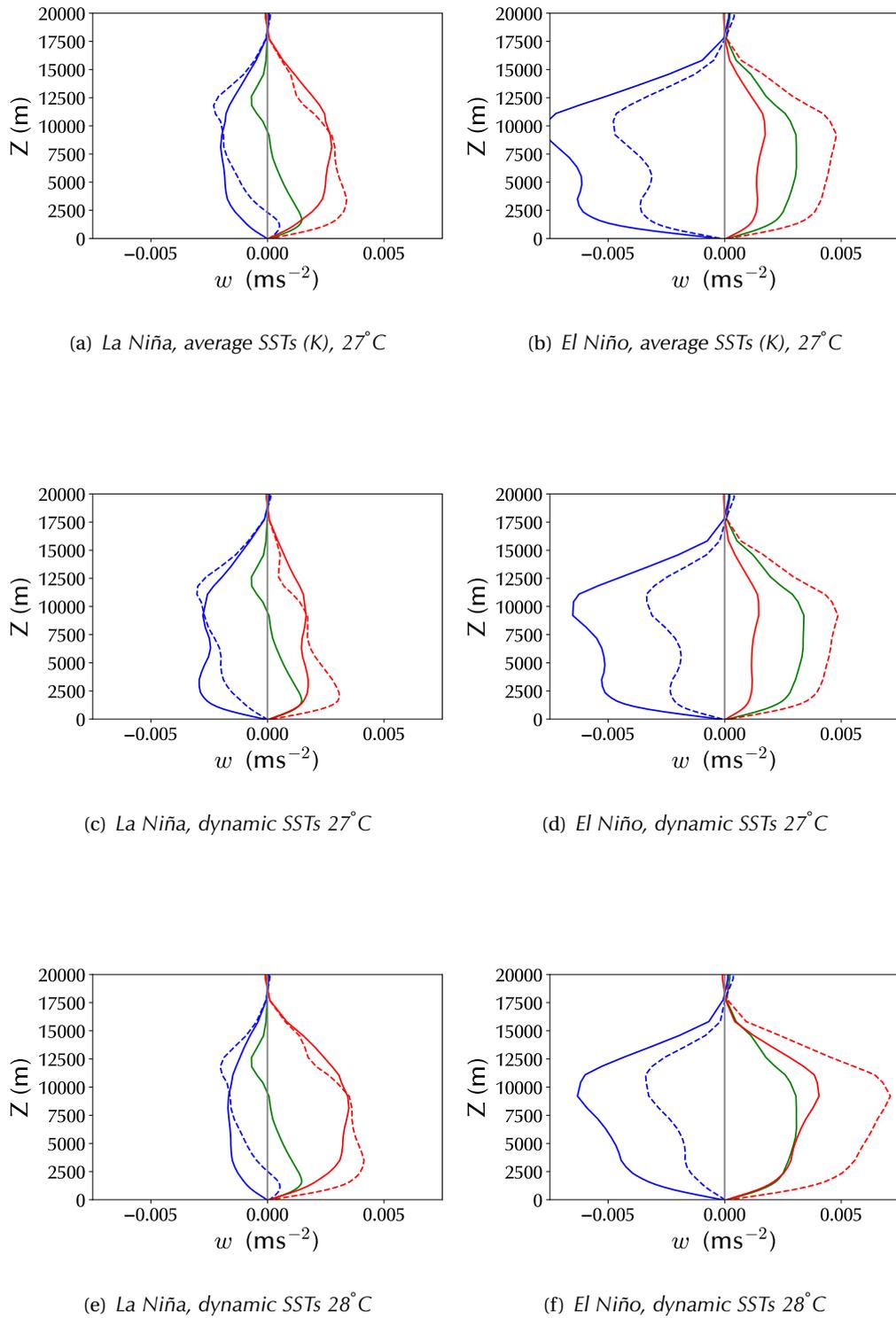
Figure 4.5: *Dashed red and blue lines represent average vertical velocity in warm and cool regions respectively for stated years, split into regions according to stated approaches. The average velocity for the entire region (green line) is subtracted to produce velocities in each region consistent with a closed circulation (solid lines).*

(W m^{-2})	W_{TdS}	W_b	W_p	$\Delta\mathcal{G}$	Discrepancy
a) La Niña, average SSTs 27°C					
Cool Region	1.64	0.31	0.37	0.93	0.03
Warm Region	3.02	0.96	0.44	1.53	0.09
LS	0.39	0.21	0.05	0.14	-0.01
Total	**2.65**	**0.79**	**0.45**	**1.32**	**0.05**
b) El Niño, average SSTs 27°C					
Cool Region	1.12	0.25	0.28	0.58	0.01
Warm Region	4.77	1.54	0.71	2.39	0.13
LS	0.96	0.39	0.15	0.43	-0.01
Total	**4.80**	**1.60**	**0.75**	**2.36**	**0.09**
c) La Niña, dynamic SSTs 27°C					
Cool Region	1.02	0.19	0.25	0.56	-0.02
Warm Region	2.84	0.81	0.45	1.49	0.09
LS	0.49	0.23	0.07	0.19	0.00
Total	**2.65**	**0.81**	**0.45**	**1.33**	**0.06**
d) El Niño, dynamic SSTs 27°C					
Cool Region	1.73	0.45	0.39	0.89	-0.00
Warm Region	4.72	1.49	0.71	2.39	0.13
LS	0.53	0.21	0.09	0.24	-0.01
Total	**4.70**	**1.51**	**0.74**	**2.36**	**0.10**
e) La Niña, dynamic SSTs 28°C					
Cool Region	1.68	0.32	0.37	0.97	0.02
Warm Region	3.02	0.99	0.42	1.51	0.10
LS	0.47	0.23	0.06	0.18	0.00
Total	**2.59**	**0.77**	**0.45**	**1.33**	**0.05**
f) El Niño, dynamic SSTs 28°C					
Cool Region	1.90	0.37	0.45	1.07	-0.01
Warm Region	4.91	1.66	0.69	2.42	0.14
LS	1.05	0.43	0.16	0.48	-0.02
Total	**4.79**	**1.59**	**0.76**	**2.37**	**0.07**

Table 4.2: *Components of mechanical energy budget for stated years, split into regions according to stated approaches.*

The components of the mechanical energy budget for the large-scale circulation defined by the interaction between the two regions and the residual circulations in each region can be calculated following the approach developed in Chapter 3, and numerical values are shown in Table 4.2. In view of the less smooth nature of the data, relative to the previous chapter, only 20 contours were used for the integrals. We note that the work done in each of the two regions is lower than for results produced by the LEM shown in Chapter 3 whereas the large-scale circulation values are more comparable. This could perhaps be explained by the difference in resolution between the reanalysis data and the LEM results, which will mean that much of the convective activity has now become sub-grid and is no longer captured in our analysis (see the discussion of Steinheimer et al. (2008) in section 1.2). To test this, the calculations were re-run with a degraded data set (with 2.5° spacing), but broadly the same numerical values were obtained, suggesting that there is little kinetic energy at length scales between the grid spacing and 2.5°. Another relevant factor is that the CRM was run in a two dimensional configuration, and has been suggested by Zeng et al. (2007) and Petch et al. (2008) that such studies may produce excessive convection when compared with fully 3D simulations.

The total values for each of the years do not depend to a great extent on the approach selected. The values calculated for the El Niño year are in general almost twice as large as those for the La Niña year. This is not consistent with the observational evidence, which suggests a stronger Walker circulation in La Niña periods (see e.g. Oort and Yienger, 1996)– this is probably related to the domain being analysed not including the Maritime Continent where much of the La Niña ascent will occur. The relatively minor discrepancies due to the approach selected between the total values for each of the years are mostly attributable to the W_b component. The scaling relationships developed in section 3.12 do a less effective job than for the LEM - in particular W_b is now generally larger than W_p, except for the cool region, implying that significant temperature differences within the warm region and between the two regions persist and make a significant contribution to the buoyancy term.

A comparison between the dynamic approaches with the two different cut-offs confirms that as ϵ decreases the values associated with the two convective circulations within each region

increase, as seen in section 3.11; this effect appears to be more important than the increase in the temperature difference between the two regions. As for the large-scale circulation, the same comparison shows an increase in all the components of the mechanical energy budget for the El Niño year as ϵ increases, but little change for the La Niña year - broadly consistent with the pattern seen in Figure 3.21b) where there is little difference between the values shown for $\epsilon = 0.3$ and $\epsilon = 0.6$, but values for $\epsilon = 0.8$ are approximately half those for $\epsilon = 0.6$.

Veiga et al. (2013) have published estimates for the Lorenz cycle for a slightly different domain in the tropical Pacific (bounded by 10° S, 5° N, 120° E and 80° W) in "the summer season" for El Niño and La Niña periods between 1979 and 2011. They make no distinction between convective and large-scale circulations, instead calculating the mean and eddy terms as in the classical Lorenz cycle. Their values indicate a total conversion from APE to kinetic energy of 0.29 W m^{-2} in a la Niña year and 0.79 W m^{-2} for El Niño, which are approximately half those seen in Table 4.2 for W_b. The reasons for these differences are not apparent, but it may be that their averaging approach eliminates many of the convective processes included in the two regions for example.

We can conclude that the techniques described in Chapter 3 can be applied to re-analysis data to calculate a mechanical energy budget for a large-scale circulation. The approaches to determining the cool and warm regions which drive such a circulation inevitably affect the values obtained for the various components, and further work is needed to determine an approach which reflects the physical realities of the ENSO system in its various phases.

It is also possible to use this re-analysis data, in particular the notional large-scale circulation analysed above, to examine how accurately the various parametrisations of the large-scale circulation tested in Chapter 3 represent the phenomena observed here. This analysis has its limits, not least since both the circulations and the underlying fields represent averages over a 12 month period, but some tentative conclusions can be drawn. The average temperature difference between the averages for the two regions at each height was used to subjectively identify the values of τ that provide a most realistic large-scale vertical velocity under the WTG

and WvTG approximations. A similar method was used to estimate the coefficient needed for the WPG approximations. Figure 4.6 shows the resulting estimates of w for the two years, using the average SST >27°C definition for the warm column. In both cases the WTG velocity was calculated using τ = 3 hours and that for the WvTG with τ = 5 hours. The WPG constant $k^2/\epsilon_{\mathrm{WPG}}$ was multiplied by a coefficient of 0.09 in the case of the La Niña year, and 0.3 for the El Niño year in order to obtain this fit, in other words the circulation is weaker than suggested by the standard WPG parameters.


(a) *La Niña*   (b) *El Niño*
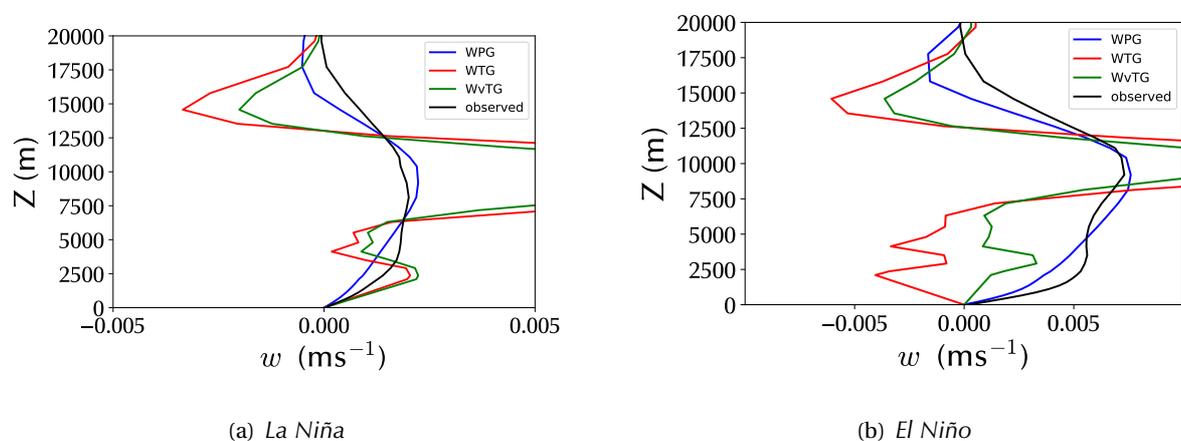
Figure 4.6: *Estimated parametrised velocities for notional Walker circulation: warm region defined by SST >27°C*

It will be seen that neither of the variants of the weak temperature gradient approximations provide a satisfactory approximation to the vertical wind profile. This is largely because the temperature difference (and indeed virtual temperature difference) between the two regions is reversed in both cases at around the 10 km level, a phenomenon that these parametrisations do not permit. The WPG approximation on the other hand is more accommodating in this regard and provides a reasonable fit, albeit with parameter values implying a circulation weaker than one resulting from those values usually used in idealised modelling studies. The effect of multiplying the standard WPG constant $k^2/\epsilon_{\mathrm{WPG}}$ by a coefficient of 0.09 and 0.3 respectively can be regarded as implying that the effective horizontal wave-number k becomes approximately $1/(3 \times 10^6)$ m^{-1} in the El Niño case and $1/(2 \times 10^6)$ m^{-1} for La Niña if the damping parameter ϵ_{WPG} is kept constant. These length scales are somewhat greater than generally

used for the WPG, but are of a similar order of magnitude to the longitudinal extent of the domain (7000 km).

4.4 Interaction with External Environment

The approach in the preceding section required the elimination of the residual net circulation across the entire region - this circulation does not depend on the definition adopted for the warm and cool regions, but will be different for each of the two years. The vertical velocity profiles can be seen plotted in green in Figure 4.5 above. This section complements the analysis of the mechanical work generated by the circulations in the tropical Pacific by seeking to assess the contribution of this external circulation.

In order to do so, it is important to identify the size of the region which closes the circulation emerging from the tropical Pacific zone, and the values of the various fields needed for the contour integrals. The circulations in question will be a mixture of a Hadley and Walker circulations, but cannot be reliably identified objectively. Instead a number of different profiles are assumed. The first approach consists of using the global dataset downloaded to establish profiles for a surrounding hollow rectangle and to approximately match the vertical velocity in the tropical Pacific zone with a scaled-up version of this external rectangle. The second consists of deriving fixed temperature and humidity profiles for a number of latitude bands around the central zone and making an assumption as to relative size. These approaches are presented in turn below.

As a first approach, an extended zone comprising a rectangular border of 20° surrounding the tropical Pacific region discussed above was selected (see Figure 4.7) which covers an area 3.2 times the size of the tropical Pacific zone. This can be interpreted as viewing this external circulation as mostly a Hadley circulation, with descent in the subtropics, and with some additional descent in the tropics. Conditional averages in (θ_e, z) coordinates for this zone (excluding the tropical Pacific region) were calculated as in previous sections.
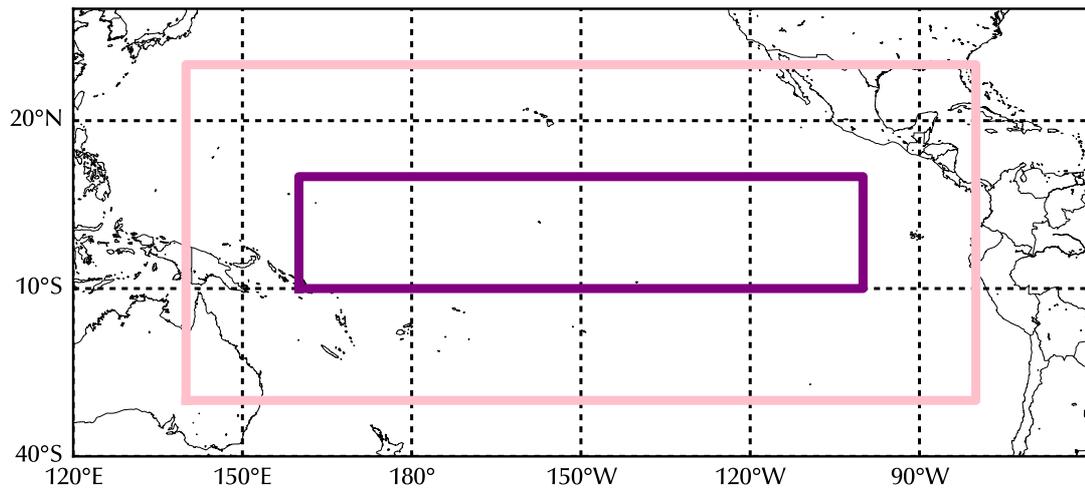
Figure 4.7: *Purple box contains tropical Pacific zone discussed in preceding section. Pink box is used to establish extended external zone.*

The vertical velocity profile in this external extended zone was compared with that in the tropical Pacific zone. A scale factor was subjectively determined that represents the relative size of a notional external zone so that vertical mass fluxes in the two zones approximately balance. In the case of the La Niña year, a scale factor of 3 was selected (Figure 4.8). This permits the calculation of a mechanical energy budget (Table 4.3). This circulation is weaker in thermodynamic terms than the large-scale circulations inside the "Tropical Pacific" domain and is predominantly driven by the temperature difference between the two regions. The sensitivity of these values to the scale factor was investigated, and it can be seen that with the partial exception of the contribution from the buoyancy term the contributions to the energy budget when multiplied by the scale factor plus one are close to constant (see Figure 4.9). This implies that although estimates of work done per unit area are dependent on this subjective scale factor, the work done by the external circulation as a whole is much less sensitive to this factor.
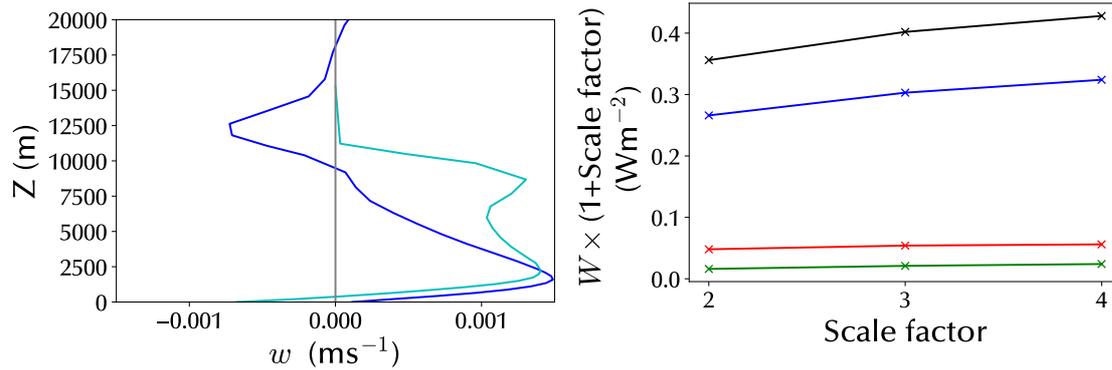
Figure 4.8: *Blue line represents vertical velocity in tropical Pacific zone. Cyan line is implied velocity based on scale factor of 3 and profile in outer zone in Figure 4.7 bounded by pink and purple lines.*

Figure 4.9: *Sensitivity of work done across assumed area (scaled) to scale factor. Black line is W_{TdS}, blue line is W_b, red line is W_p and green lines is $\Delta \mathcal{G}$.*

The same method was applied to the El Niño year. Figure 4.10 shows the match between the vertical velocities, with a scale factor of 9. The numerical values of the components of work done are shown in Table 4.3. The work done per unit area by this circulation is twice as strong as in the La Niña year, and as before once the scale factor dependency is eliminated the values are almost constant (Figure 4.11).
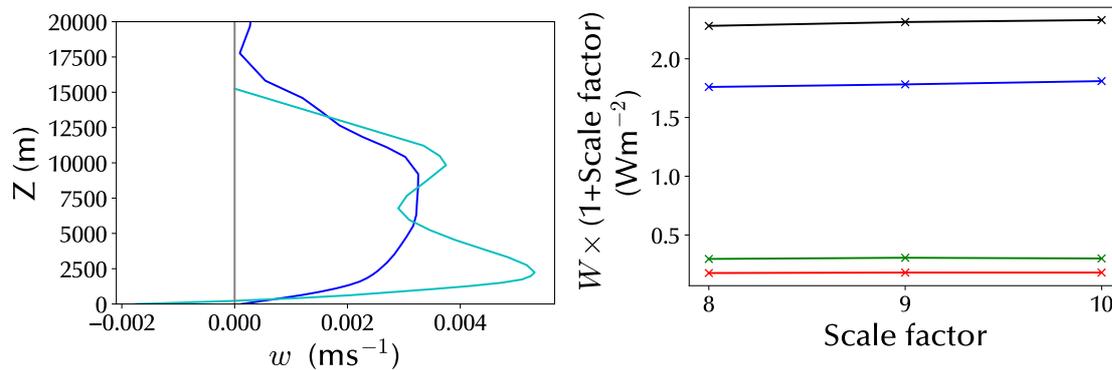

Figure 4.10: *Blue line represents vertical velocity in tropical Pacific zone. Cyan line is implied velocity based on scale factor of 9 and profile in outer zone in Figure 4.7 bounded by pink and purple lines.*

Figure 4.11: *Sensitivity of work done across assumed area (scaled) to scale factor. Black line is W_{TdS}, blue line is W_b, red line is W_p and green lines is $\Delta \mathcal{G}$.*

(W m^{-2})	W_{TdS}	W_b	W_p	$\Delta\mathcal{G}$	Discrepancy
La Niña	0.13	0.10	0.02	0.01	0.00
El Niño	0.26	0.2	0.02	0.03	0.01

Table 4.3: *Components of mechanical energy budget for external circulation linked to extended profile.*

As in the previous section, the extent to which the various parametrisations can represent this notional large-scale circulation was tested. Parameter values selected for the La Niña year were τ = 100 hours for the WTG and for the WvTG, and coefficient of 0.005 multiplied the WPG parameter $k^2/\epsilon_{\text{WPG}}$. These values are very much weaker than those for the internal circulation. Corresponding values for the El Niño year were 50 hours, 60 hours, and 0.015, a somewhat stronger circulation. None of the parametrisations provide a satisfactory fit for the La Niña year, but the WPG seems preferable in the case of the El Niño year. The coefficient used for the El Niño year is consistent with an effective value of k, the wavenumber of the damped gravity waves, of approximately $1/(8 \times 10^6)$ m^{-1} which implies a length scale significantly greater than figures for the notional Walker circulation considered in the previous section.

(a) *La Niña* (b) *El Niño*
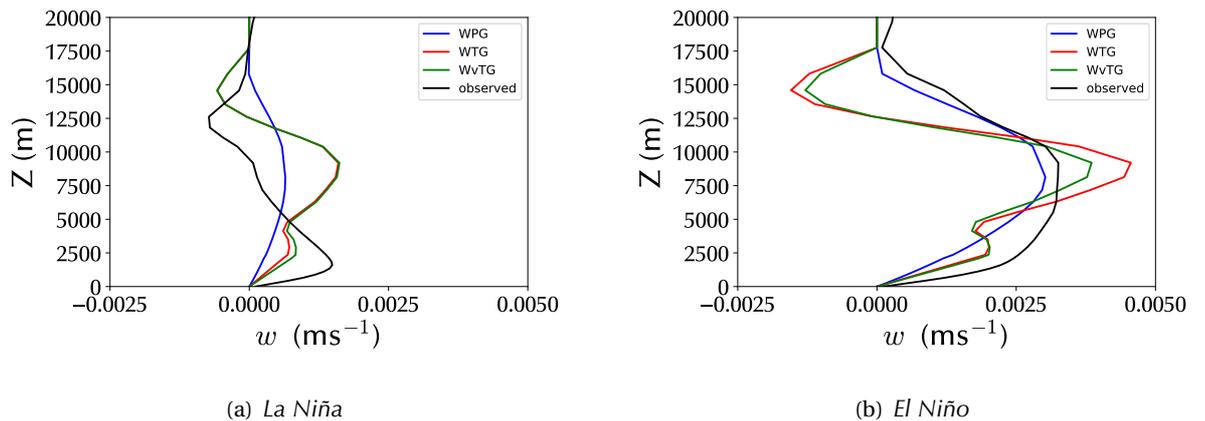
Figure 4.12: *Fitted parametrised velocities for notional Hadley circulation.*

In order to obtain an understanding of the sensitivity of these values to the fields in the external zone, a variety of fixed profiles representing the external region were also used. The profiles were derived separately for each of the two years, and are averages of regions 10, 20

and 30 degrees wide to both the North and South (combined) of the tropical Pacific zone and are shown in Figure 4.13. The components of the mechanical energy budget based on these profiles and assuming that the external region is twice the size of the inner zone are shown in Tables 4.4 and 4.5 for the two years.


(a) *Temperature*

(b) *Vapour mixing ratio*

(c) *Liquid mixing ratio*

(d) *Ice mixing ratio*
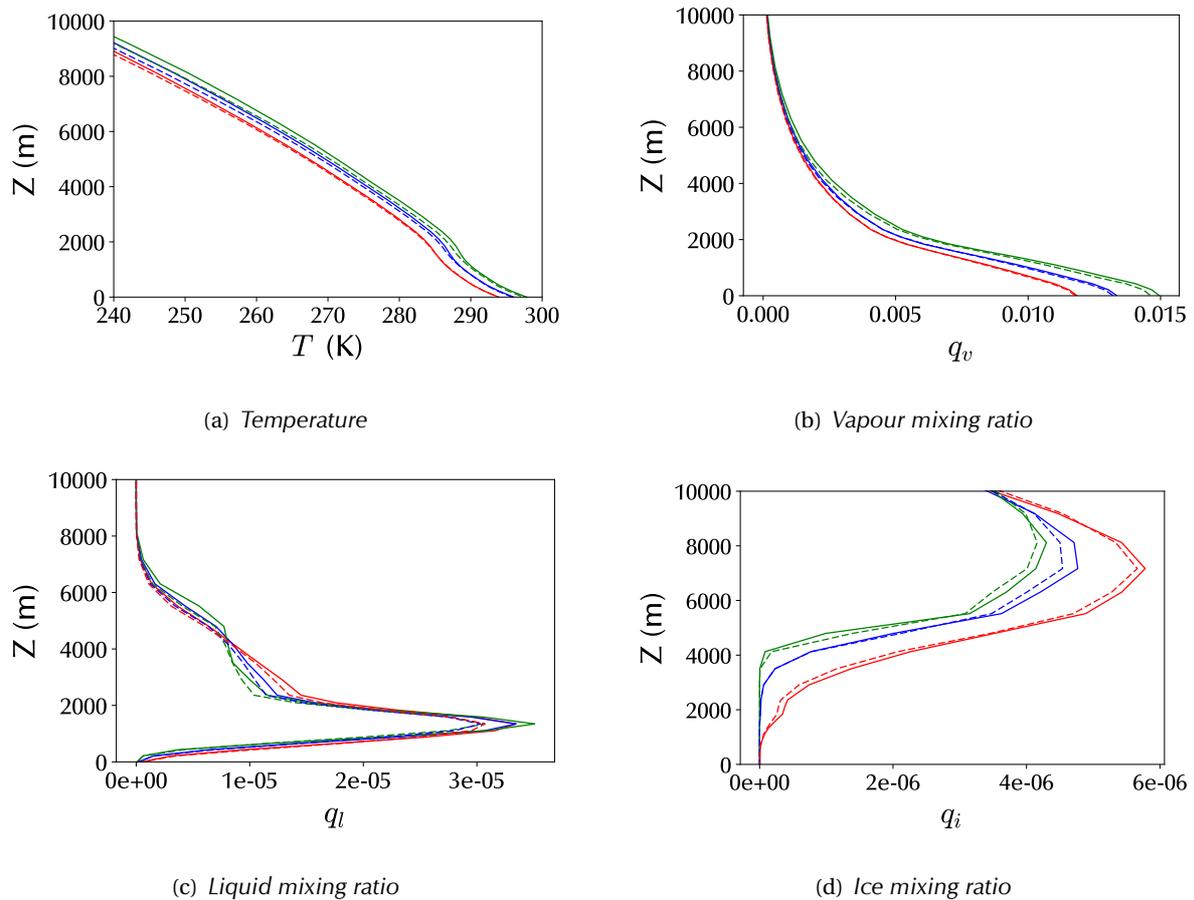
Figure 4.13: *Fixed profiles for external zone - 10° (green), 20° (blue) and 30° (red) N and S of tropical Pacific zone for El Niño (solid) and La Niña (dashed) years.*

$(\mathrm{W\,m^{-2}})$	W_{TdS}	W_b	W_p	$\Delta\mathcal{G}$	Discrepancy
10°-20°	0.13	0.03	0.03	0.08	-0.01
10°-30°	0.20	0.07	0.04	0.10	-0.01
10°-40°	0.31	0.14	0.06	0.11	0.00

Table 4.4: *Components of mechanical energy budget for external circulation linked to fixed profile for La Niña year.*

(W m^{-2})	W_{TdS}	W_b	W_p	$\Delta\mathcal{G}$	Discrepancy
10°-20°	0.53	0.21	0.08	0.28	-0.04
10°-30°	0.91	0.49	0.11	0.33	-0.02
10°-40°	1.44	0.93	0.13	0.35	0.03

Table 4.5: *Components of mechanical energy budget for external circulation linked to fixed profile for El Niño year*

In comparing these sets of results with those in Table 4.3 one must bear in mind that the surface areas covered by those circulations are 4/3 greater for the La Niña year and 10/3 greater for the El Niño year. In addition, the use of a fixed profile for the sub-tropics here reduces the variability of values in the cool region and hence the values of the components of the mechanical energy budget equation. What is clear however, is that increasing the latitude covered by the external region increases the work done elements. The buoyancy term is much more sensitive than other terms, a reflection of the greater contrast in SSTs in the region covered.

There are some striking differences between the values shown in Table 4.3 on the one hand, and Tables 4.4 and 4.5 on the other. The buoyancy term is less significant in the results based on a fixed profile - as a result of the averaging that gives rise to the profile, the impact of the coolest regions in the subtropics is muted. On the other hand the values of W_{TdS} are of a similar order of magnitude between the two sets of results - it transpires that the circulation $(\max|\Psi|)$ is very much stronger for the fixed profile cases. This is because there is less overlap between the regions in (θ_e, z) space in which upward and downward motion occurs than for the profiles used to construct Table 4.3 where much of the upward and downward motion cancels. The use of a fixed profile does not capture much of the complexity inherent in thermodynamic processes and should be treated with caution.

Huang and McElroy (2014) have quantified the work done by the Hadley Circulation using streamfunction integrals of $p\mathrm{d}V$. Their method is based on monthly zonal averages of re-analysis data and they estimate that the conversion rate between potential and kinetic en-

ergy due to the Hadley Circulation is 0.39 W m^{-2} over the period 1979-2010, which would correspond to 0.75 W m^{-2} over the region used to calculate the values in Tables 4.4 and 4.5. This value is of a similar order of magnitude to the values obtained above, perhaps somewhat higher, depending on the weighting given to El Niño and La Niña years.

4.5 CONCLUSION

This chapter has shown that it is possible to apply the methodology developed in previous chapters to re-analysis data to estimate the mechanical work done by a large-scale circulation. The estimates that such a method produces for local convective circulations appear low, and this is probably explained by the fact that sub-grid motions are neglected. The estimates produced for a notional Walker circulation depend very much on the definition of ascending and descending branches - this chapter has tested various different approaches based on SSTs and these produce results which are in total consistent but depend on the definition used in plausible and understandable ways. It may be that a more satisfactory approach would be based on using a dynamical definition of the two branches, for example based on velocity potential at 200 hPa. Likewise, the estimates for a notional Hadley circulation are dependent on the definitions used. Despite any uncertainties, the values obtained for the mechanical work generated by such a circulation are however not inconsistent with those produced in other studies.

In addition, the degree to which some of the parametrisations of large-scale circulations that were tested using a CRM in Chapter 3 provide a reasonable match between observed and parametrised vertical velocity profiles was tested. The WPG approach appears superior to either the WTG or WvTG, albeit with parameters modified from those generally used in most idealised studies to produce a much weaker circulation.

CHAPTER 5

DISCUSSION

5.1 SUMMARY AND CONTRIBUTION

In this thesis we have explored the generation of mechanical work by an overturning circula-
tion, largely one modelled by the WTG approximation. The two main aims were:

- To investigate the factors that limit the generation of mechanical energy by overturning
  circulations in cases where the rotational effects of the earth can be neglected, such as
  in the tropics or for small-scale convective systems.

- To provide insights into the thermodynamic implications of supra-domain parametrisa-
  tions such as the WTG, in particular whether they introduce any anomalies that might
  undermine their usefulness.

These aims have been largely achieved.

In Chapter 2 we approached this topic using a simplified Single Column Model (SCM) and de-
veloped analytical expressions for some of the main quantities considered. For the Weak Tem-
perature Gradient (WTG) approximation we showed how the mechanical work done in a dry
case depends on the coupling time-scale parameter, the temperature difference between the
columns and their relative size. We also demonstrated how the work production relates to the
Carnot efficiency factor and to the generation of irreversible entropy. We extended the model
to include moisture and showed why this may give rise to multiple equilibria. We also briefly
considered the Weak Pressure Gradient (WPG) approximation and showed that, although it

results in smoother vertical velocity profiles, from a thermodynamic perspective it is quite similar to the Weak Temperature Gradient approximation.

In Chapter 3 we took a more realistic and complex approach, using results from two coupled Cloud Resolving Models (CRMs). We extended and used a recently published technique to diagnose components of the mechanical energy budget to analyse the sensitivity of those components to the same parameters as considered in the previous chapter. We showed that the use of the Weak Temperature Gradient (WTG) approximation to couple the two regions did not introduce any thermodynamic anomalies, and that the sensitivities were largely consistent with the theoretical analyses that we previously developed, although the drying out of the cool region also has a significant influence. We developed scaling arguments that explain the relative values of the components of the mechanical energy budget. We also investigated differences between the Weak Temperature Gradient and Weak Pressure Gradient approximations, and saw that the latter can exhibit oscillatory behaviour when used for two coupled regions of comparable size.

In Chapter 4 we applied the diagnostic approach referred to above to re-analysis data. We show that this approach can produce internally consistent values for the mechanical energy budget for a large-scale circulation such as the Walker or Hadley circulation.

We regard the main contribution of this thesis to be the development of new, and extension, of existing methodologies. In particular we have produced:

- Approximate analytical expressions for the energy terms associated with the WTG approximation, especially the identification of the conversion from potential to kinetic energy as $2\bar{A}/\tau$.

- Approximate analytical expressions for the work generated by a dry overturning WTG-coupled circulation, as a quadratic function of the SST difference between the columns, expressed in terms of other atmospheric properties.

- An additional term in the Pauluis mechanical energy budget which improves the results for an anelastic model.

- A new approach which separates convection in two coupled regions into three circulations, i.e a local convective circulation in each of the regions and a large-scale circulation covering both regions. This permits calculation of separate mechanical energy budgets for each of the circulations.

- Scaling arguments which explain the relative values of the components of the Pauluis mechanical energy budget.

The methodologies developed have all been applied to either model results or re-analysis data. In particular, Cloud Resolving Model (CRM) results were used to show:

- That the introduction of WTG coupling does not significantly modify the total mechanical energy budget relative to uncoupled columns, implying that it is thermodynamically consistent.

- That the WPG approximation run in two coupled regions can generate marked oscillations between a number of different modes for vertical velocities and temperature differences between the two regions. This problem does not arise when the WPG is used in conjunction with a reference column approach.

The mechanical energy budget was also calculated for circulations in the tropical Pacific for two years in different ENSO phases. All the work done components in the El Niño phase were approximately twice those in the La Niña phase.

Other useful results include:

- Attempts to fit parametrised large-scale circulations to the re-analysis data generally suggest that the WPG approximation provides a more realistic representation of vertical velocity profiles than the WTG approximation. This is partly because the re-analysis data exhibits a negative temperature difference between the regions at certain heights, which under the WTG would result in a reversal of vertical velocities, but is smoothed out

by the WPG. The WPG parameters however imply rather larger length-scales than those generally used in idealised studies, but ones not inconsistent with the physical extent of the domain, at least for the notional Walker circulation.

- An illustration that the calculation of APE through sorting in a two-column model can produce an overestimation due to discrete model layers.

- A demonstration that although the MEP conjecture can explain a realistic atmospheric lapse rate in the lower atmosphere, this may not work as well at higher altitudes.

- A detailed examination of the energy implications of increasing the temperature difference between two dry columns coupled by the WTG. The work generated is balanced by a cooling of the columns, increasing the Carnot efficiency, although this is partially offset by greater irreversible entropy production.

5.2 IMPLICATIONS

The marked effect on the convective processes in two separate regions of introducing large-scale overturning is striking. Although the large-scale vertical velocity is much smaller in magnitude than the residual vertical velocities generated by the convective processes in the regions, the components of the mechanical energy budget are comparable. The introduction of even very weak coupling suppresses convection in the dryer/cooler region and enhances it in the moister/warmer region. The imposition of the WTG approximation may be interpreted as a representation of the requirement for low temperature gradients in the tropics due to weak rotational effects. In this sense, the contrast in local convective intensity can be seen as the consequence of a large-scale dynamical constraint and not as a local result of contrast in SSTs.

5.3 FUTURE WORK

The drivers of the size of self-aggregating convective systems remains an issue of active research (e.g. Wing and Cronin, 2016; Holloway, 2017; Stein et al., 2017). The analysis in section 2.7 shows how the effective timescales of the various physical processes modelled in conjunc-

tion with an overturning circulation in a simplified case combine to set plausible limits on their size. One could explore whether this approach could be extended into a more realistic analysis, taking into account the timescales of processes such as the interactive aspects of radiation that are neglected in the simplified model.

The existence of multiple equilibria in weak temperature gradient models continues to attract attention (e.g. Sentić and Sessions, 2017). The conditions that permit this to occur in a simple case were identified in section 2.11. This analysis could be extended to analyse the circumstances in which this situation can arise in more complex situations as represented in Cloud Resolving Models.

The CRM used in Chapter 3 has not been developed to be energy conserving and the results are therefore to some extent approximate. Models have been developed which conserve energy explicity (e.g Romps, 2008) and it would be interesting to repeat some of the work in that chapter with a more sophisticated model to verify that the conclusions hold, particularly since one could then ensure consistency in thermodynamic assumptions between the model and the diagnostic framework. Furthermore, the CRM has been used in a two-dimensional configuration. As section 2.7 shows, the explicit introduction of a third dimension can influence the energetic pathways profoundly and this too could be explored in a CRM context. The limited evidence that the WPG provides a better fit for observed large-scale circulations than the WTG would suggest that more extensive analysis of WPG coupled columns along the lines of Chapter 3 would also be of value. A further modelling aspect of the model which could be modified is the radiation scheme; including interactive radiation would identify the impact of physical processes not represented in our current work.

The striking differences in magnitude between the components of the mechanical energy budget derived in Chapters 3 and 4 suggest that sparser grids, be they used in re-analysis or GCMs, may significantly underestimate the mechanical work generated by atmospheric processes. Further work on identifying how sub-grid generation of kinetic energy can be represented in global models appears a promising avenue. Given the importance of this for MJO modelling

(Holloway et al., 2013), such work could lead to an improvement in the accuracy of climate models.

Chapter 4 provided a proof of concept that these techniques can be used to diagnose components of the mechanical energy budget from re-analysis data. This could be extended in a number of different directions - it could be combined with the month-by-month identification of the Hadley circulation used in Huang and McElroy (2014) to obtain more reliable values for the work done by that circulation. Additionally, an approach based on velocity potential could be used to identify the ascending and descending branches of the Walker circulation and to provide more robust estimates of the work done by that circulation in a variety of ENSO conditions. The large-scale circulations implied by these definitions of cool and warm regions could also be compared with the parametrised velocities obtained using the WTG and WPG approximations with fitted parameter values.

The need to adequately represent tropical convection in global climate models remains a major challenge for atmospheric science. It is hoped that some of the avenues suggested above will in time lead to further progress in this area.

APPENDIX - THE MAXIMUM ENTROPY PRODUCTION CONJECTURE

The Maximum Entropy Production (MEP) conjecture, as first advanced in Paltridge (1975) and discussed in Ozawa et al. (2003), postulates that many physical processes in the atmosphere, in particular vertical heat transport, operate over a long period in such a manner as to maximise the production of entropy.

This hypothesis has stimulated a number of analyses of radiative-convective equilibria such as Ozawa and Ohmura (1997) and Herbert et al. (2013). Despite this interest, the approach has not yet found a significant application in climate models.

The conjecture was explored using the simplified SCM in a single column configuration, i.e. without any coupling. This variant of the model does not include short-wave absorption, other than due to O_3 in the stratosphere. It is possible to set a maximum environmental lapse rate, in which case the model will converge to an equilibrium state with upward enthalpy fluxes from the surface (i.e. convection). Alternatively, it is possible to solve for the enthalpy fluxes which will achieve a certain equilibrium.

Initial investigations focused on variants of a model where incoming radiation is the key determining variable, and which are referred to as the "energy-consistent model". This was first explored using a simplified theoretical model. The atmosphere is represented by a single slab that is transparent to short-wave radiation but has long-wave emissivity (and absorptivity) of $\epsilon = 1 - e^{-\tau_{LW}}$. Following the approach presented in Ambaum (2010, Chap. 9.7) it is possible to

express the relationships between the temperature of the Earth's surface T_S, that of the atmosphere T_A, and the enthalpy flux from the Earth to the atmosphere H thus:

$$(1 - \alpha) S_0 / 4 = \epsilon \sigma T_A^4 + (1 - \epsilon) \sigma T_S^4 \quad , \tag{A.1}$$

$$2 \epsilon \sigma T_A^4 = \epsilon \sigma T_S^4 + H \quad . \tag{A.2}$$

In this case the entropy production $\dot{S}$ is simply $H(1/T_A - 1/T_S)$. It is possible to find an expression for the maximum of this value in terms of T_A, T_S analytically and thus obtain expressions for the entropy production and enthalpy flux in the Maximum Entropy Production (MEP) state by differentiating these equations:

$$\frac{\mathrm{d}T_A}{\mathrm{d}T_S} = -\frac{(1 - \epsilon) T_S^3}{\epsilon T_A^3} \quad \text{from Equation A.1,} \tag{A.3}$$

$$\frac{\mathrm{d}T_S}{\mathrm{d}H} = -\frac{-1}{4\sigma(2 - \epsilon) T_S^3} \quad \text{from Equation A.2 and using A.3.} \tag{A.4}$$

The maximum entropy production enthalpy flux H_{MEP} will be found when $\mathrm{d}\dot{S}/\mathrm{d}H = 0$ thus:

$$H_{\mathrm{MEP}} = \frac{\left(\frac{1}{T_A} - \frac{1}{T_S}\right) 4\sigma(2 - \epsilon)}{\frac{1 - \epsilon}{\epsilon T_A^5} + \frac{1}{T_S^5}} \quad . \tag{A.5}$$

Values for T_A, T_S for this maximum are not easily found analytically. Figure A.1 shows entropy production and surface and atmosphere temperatures as a function of enthalpy flux. $\dot{S}$ is clearly zero when there is no enthalpy flux, and also when the two bodies are at the same temperature – which corresponds to the maximum value of $H = \epsilon(1 - \alpha) S_0 / 4$. For intermediate values of H, $\dot{S}$ will be positive and hence will reach at least one maximum at an intermediate point.

The SCM was modified in order to identify the MEP enthalpy fluxes which maximised the entropy produced by a "convective" process. Initially this was done by varying the fixed maximum lapse rate, although in later analyses this constraint was modified. The values of entropy produced as a function of surface enthalpy fluxes is shown in Figure A.2.
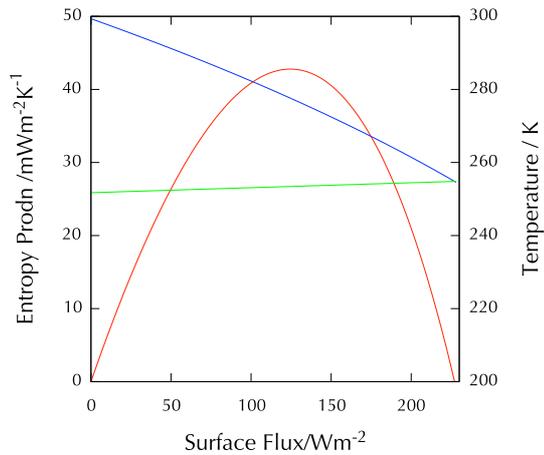
Figure A.1: *Entropy production (LH axis, red) and temperature of Earth's surface (RH axis, blue) and atmosphere (RH axis, green) from energy consistent single slab model.*
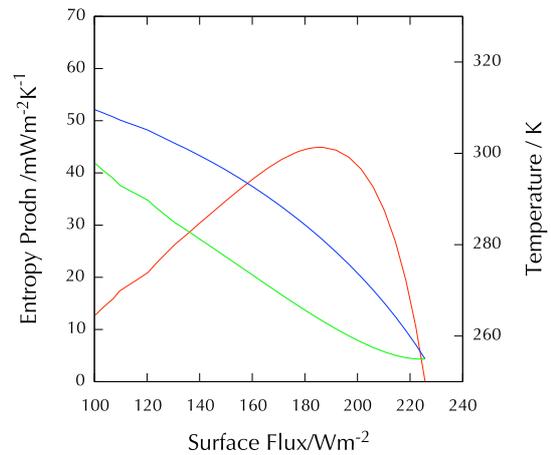
Figure A.2: *Entropy production (LH axis, red) and temperature of Earth's surface (RH axis, blue) and atmosphere (RH axis, green) from energy consistent single lapse rate model. Note different scale to Figure A.1.*

Some of the differences between Figure A.1 and Figure A.2 arise from the fact that in the multi-layer model as the enthalpy decreases the transport reaches only the lowest layers of the atmosphere in this model. Consequently the implied temperature in the atmosphere and that at the surface converge as enthalpy declines, unlike in the single slab model. Also the entropy production is less symmetrical around the maximum. The MEP state corresponds to a lapse rate in the region of 4.5 K km^{-1}.

The model was further modified to identify the enthalpy fluxes which maximise the MEP with no requirement for a single lapse rate, using a variant of the downhill simplex method due to Nelder and Mead (Press et al., 2007, pp. 502–507). In order to reconcile the results of this work with those obtained in published work (see below) it was necessary to reconsider the approach taken to SW heating. The original model had some heating in the stratosphere representing O_3 absorption, but none in the troposphere. Further assumptions were made, namely that the reflection of in-coming SW radiation occurs entirely at the top of the atmosphere, and that absorption in the atmosphere occurs with SW optical depth distributed in proportion to LW

optical depth, although alternatives were investigated. The resultant lapse rates and enthalpy profiles for different LW optical depths are shown in Figures A.3 and A.4. The lapse curve for pure radiative equilibriums is also shown, as is the enthalpy flux for an isothermal atmosphere.
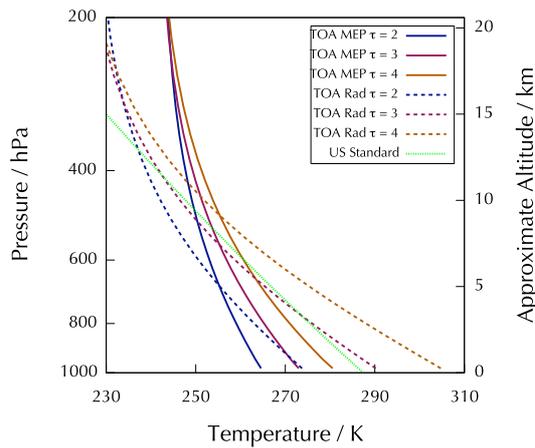

Figure A.3: *Temperature profiles for radiative equilibrium (dashed) and MEP (solid) states for different values of τ, the LW optical depth of the atmosphere (2,navy, 3, magenta, 4 olive) for energy consistent model. The US standard atmosphere is shown for comparison in green.*
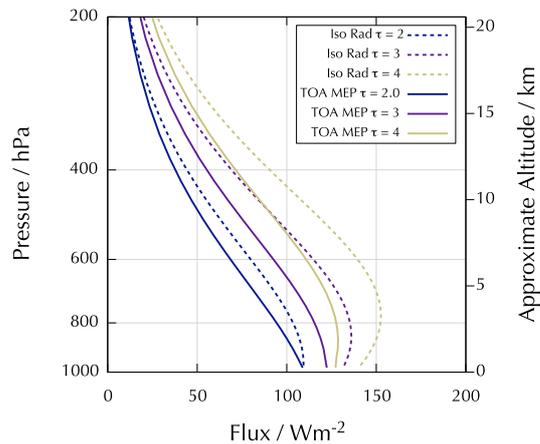
Figure A.4: *Enthalpy flux profiles for isothermal (dashed) and MEP (solid) states for different values of τ, the LW optical depth of the atmosphere (2,navy, 3, magenta, 4 olive) for energy consistent model.*

These results were compared with those obtained by Herbert et al. (2013) as shown in Figures A.5 and A.6. Results for the same variables are also shown in Ozawa and Ohmura (1997) (see Figures A.7 and A.8) with similar parameters. Unfortunately neither of these papers show results above 400 hPa. There are considerable discrepancies in the enthalpy fluxes which decline more rapidly with height in the two previously published studies. The MEP lapse rates appear broadly comparable in the lower atmosphere although the results obtained here tend towards higher temperatures in the middle troposphere when compared with the previous studies. The enthalpy fluxes will be dependent on the distribution of SW heating of the atmosphere, and to assumptions as to pressure-broadening.

The models were further adjusted to allow for a fixed Sea Surface Temperature (SST), with
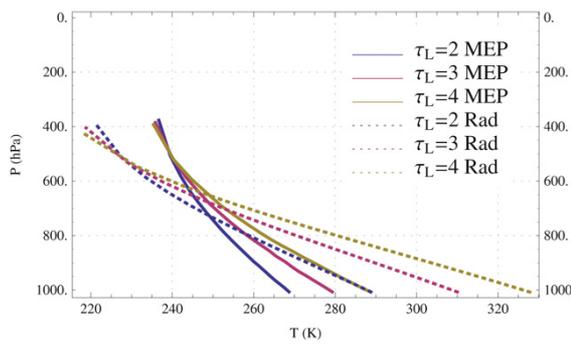
**Figure A.5:** *Temperature profiles for MEP and radiative states from Herbert et al. (2013). (©2013 AMS)*
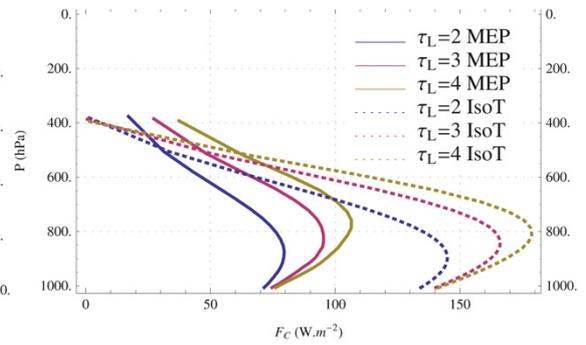
Figure A.6: *Enthalpy fluxes for MEP and isothermal states from Herbert et al. (2013). (©2013 AMS)*
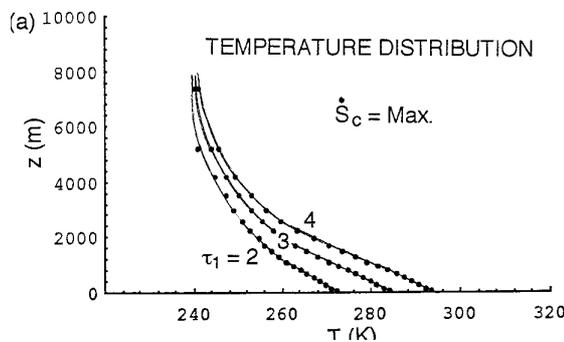

**Figure A.7:** *Temperature profiles for MEP states from Ozawa and Ohmura (1997).(©1997 AMS)*
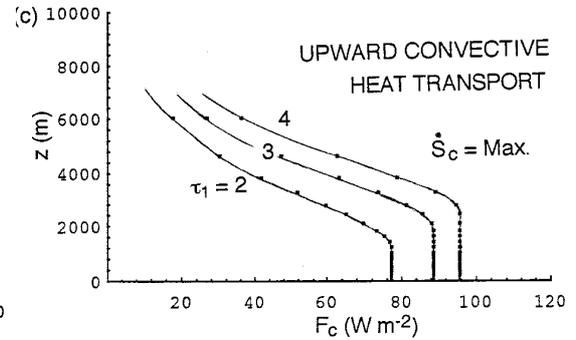
Figure A.8: *Enthalpy fluxes for MEP states from Ozawa and Ohmura (1997).(©1997 AMS)*

no energy constraints on the incoming SW radiation (thus all these models were run on the basis of no SW absorption by the atmosphere). Such models are frequently used since this decoupling captures the fact that the ocean's high heat capacity results in slow SST response to changes in atmospheric temperatures. In view of the fact that incoming SW radiation is effectively determined in these models by the SST and the entropy constraint, SW absorption in the atmosphere was set to zero.

Theoretical expressions for enthalpy flux and entropy produced were derived as before. In this case it was possible to obtain analytic expressions relating the temperature of the atmosphere T_A to the surface temperature T_S in the MEP state as follows. We start with the expression for

energy balance in the atmosphere:

$$H + \epsilon \sigma T_S^4 = 2\epsilon \sigma T_A^4 \quad \text{(for atmosphere).} \tag{A.6}$$

$$\implies 1 = 8\epsilon \sigma T_A^3 \frac{\mathrm{d}T_A}{\mathrm{d}H} \quad, \tag{A.7}$$

as T_s is constant. To find the MEP state we find the value of H for which $\dot{S}$ is at a maximum.

$$\dot{S} = H\left(\frac{1}{T_A} - \frac{1}{T_S}\right) \quad, \tag{A.8}$$

$$\implies \frac{\mathrm{d}\dot{S}}{\mathrm{d}H} = \left(\frac{1}{T_A} - \frac{1}{T_S}\right) - \frac{H}{8\epsilon \sigma T_A^5} = 0 \quad. \tag{A.9}$$

$$\implies H = 8\epsilon \sigma T_A^4\left(1 - \frac{T_A}{T_S}\right) = \epsilon \sigma(2T_A^4 - T_S^4) \quad, \text{using Equation A.6} \quad, \tag{A.10}$$

$$\implies 8\left(1 - \frac{1}{x}\right) = (2 - x^4) \quad, \text{putting } x = \frac{T_S}{T_A}, \text{providing } \epsilon \neq 0 \quad. \tag{A.11}$$

This quintic can be solved, and the only physically meaningful value of x is 1.0839. In other words, this slab model predicts that in an MEP state there is a constant ratio between surface and atmosphere temperatures irregardless of SST or optical depth.

Results were obtained for the MEP state with convection constrained by a single lapse rate, but these have not been included here. As before, the model was then used to determine lapse rates and enthalpy fluxes corresponding to the maximum entropy production state. Temperature and enthalpy flux profiles are shown for different SSTs and different values of τ_{LW} in Figures A.9 - A.12.

It will be noted that the temperature profiles for different SSTs are in constant proportion, and that there is not much difference between the profiles for the different optical depths, as predicted by the theoretical analysis above. All of the temperature profiles show a significant difference between the surface temperature and the temperature at the bottom of the atmosphere, in contrast to the energy-consistent models above. This is because greater enthalpy fluxes do not decrease the surface temperature in the fixed SST model. A similar discontinuity in MEP models has been remarked upon by Pascale et al. (2012). The enthalpy fluxes in the fixed SST models are generally greater than those in the energy consistent models, and conse-

quently there is greater heating of the atmosphere.
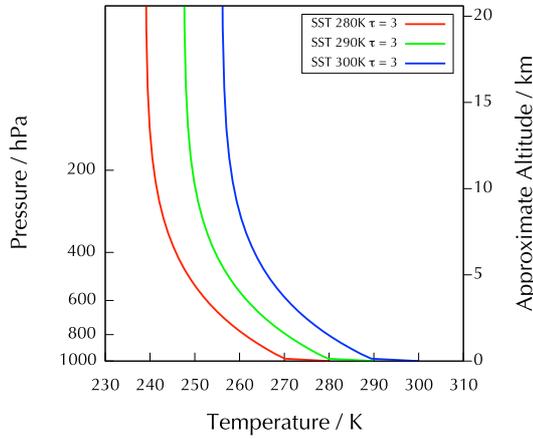
Figure A.9: *Temperature profile for MEP state for fixed SST model for a range of SSTs - note that ratio of profiles does not depend on height. LW optical depth is 3.*
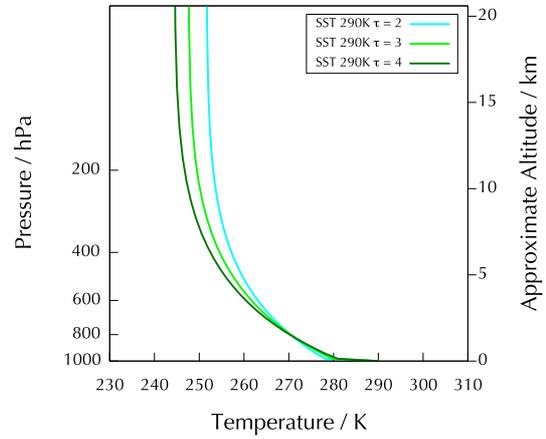
Figure A.10: *Temperature profile for MEP state for fixed SST model for a range of LW optical depths - note little sensitivity. SST is 290 K.*
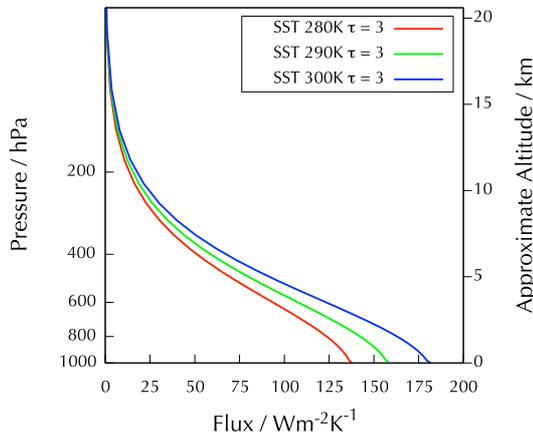
**Figure A.11:** *Enthalpy fluxes corresponding to profiles in Figure A.9*
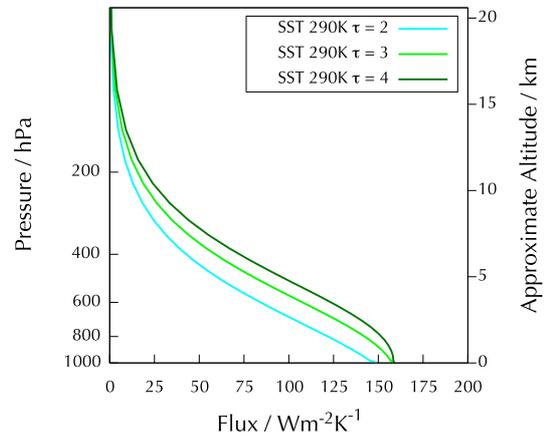
Figure A.12: *Enthalpy fluxes corresponding to profiles in Figure A.10*

The energy-consistent model has illustrated how with quite simple assumptions the MEP can be used to derive reasonable values for the enthalpy fluxes in the atmosphere and the temper-

ature lapse rate, at least in the lower atmosphere, consistent with other published work. Given the complexity of the turbulent processes that occur in the lower atmosphere, this result suggests that the MEP can provide a convincing broad narrative for the long term mean properties of the atmosphere, even if it is of limited usefulness for more detailed modelling studies.

References

Ambaum, M. H. P., 2010: *Thermal physics of the atmosphere*. John Wiley & Sons.

Arakawa, A., and W. H. Schubert, 1974: Interaction of a cumulus cloud ensemble with the large-scale environment, Part I. *Journal of the Atmospheric Sciences*, **31 (3)**, 674–701.

Bechtold, P., 2014: Atmospheric moist convection. Tech. rep., ECMWF.

Benedict, J. J., and D. A. Randall, 2009: Structure of the Madden–Julian oscillation in the super-parameterized CAM. *Journal of the Atmospheric Sciences*, **66 (11)**, 3277–3296.

Bergman, J. W., and P. D. Sardeshmukh, 2004: Dynamic stabilization of atmospheric single column models. *Journal of Climate*, **17 (5)**, 1004–1021.

Berrisford, P., D. Dee, K. Fielding, M. Fuentes, P. Kallberg, S. Kobayashi, and S. Uppala, 2009: The ERA-interim archive. Tech. Rep. 1, European Centre for Medium-Range Weather Forecasts, 1–16 pp.

Betts, A. K., and M. J. Miller, 1993: The Betts-Miller scheme. *The representation of cumulus convection in numerical models, Meteorological Monograph no. 46*, K. A. Emanuel, and D. J. Raymond, Eds., American Meteorological Society, 107–121.

Bolton, D., 1980: The computation of equivalent potential temperature. *Monthly Weather Review*, **108 (7)**, 1046–1053.

Boltzmann, L., 1896: *Vorlesungen über Gastheorie*, Vol. 1. JA Barth.

Carissimo, B. C., A. H. Oort, and T. H. V. Haar, 1985: Estimating the meridional energy transports in the atmosphere and ocean. *Journal of Physical Oceanography*, **15 (1)**, 82–91.

Carnot, S., 1824: *Reflections on the motive power of fire, and on machines fitted to develop that power*. Paris: Bachelier.

Clausius, R., 1867: *The mechanical theory of heat: with its applications to the steam-engine and to the physical properties of bodies*. J. van Voorst.

Daleu, C., 2013: Simulations of interacting regions of tropical deep convection coupled by

References

a weak-temperature gradient parameterization of the large-scale circulation. Ph.D. thesis, University of Reading.

Daleu, C. L., S. Woolnough, and R. Plant, 2012: Cloud-resolving model simulations with one- and two-way couplings via the weak temperature gradient approximation. *Journal of the Atmospheric Sciences*, **69 (12)**, 3683–3699.

Daleu, C. L., S. J. Woolnough, and R. S. Plant, 2015a: Transition from suppressed to active convection modulated by a weak temperature gradient–derived large-scale circulation. *Journal of the Atmospheric Sciences*, **72 (2)**, 834–853.

Daleu, C. L., and Coauthors, 2015b: Intercomparison of methods of coupling between convection and large-scale circulation: 1. Comparison over uniform surface conditions. *Journal of Advances in Modeling Earth Systems*, **7 (4)**, 1576–1601.

Daleu, C. L., and Coauthors, 2016: Intercomparison of methods of coupling between convection and large-scale circulation: 2. Comparison over nonuniform surface conditions. *Journal of Advances in Modeling Earth Systems*, **8 (1)**, 387–405.

Dorrestijn, J., D. T. Crommelin, A. P. Siebesma, H. J. J. Jonker, and C. Jakob, 2015: Stochastic parameterization of convective area fractions with a multicloud model inferred from observational data. *Journal of the Atmospheric Sciences*, **72 (2)**, 854–869.

Edman, J. P., and D. M. Romps, 2014: An improved weak-pressure-gradient scheme for single-column modeling. *Journal of the Atmospheric Sciences*, **71 (7)**, 2415–2429.

Emanuel, K. A., 1986: An air-sea interaction theory for tropical cyclones. Part I: Steady-state maintenance. *Journal of the Atmospheric Sciences*, **43 (6)**, 585–605.

Emanuel, K. A., 1994: *Atmospheric convection.* Oxford University Press.

Flato, G., and Coauthors, 2013: Evaluation of Climate Models. in: Climate Change 2013: The Physical Science Basis. Contribution of Working Group I to the Fifth Assessment Report of the Intergovernmental Panel on Climate Change. *Climate Change 2013*, **5**, 741–866.

Frank, W. M., 1977: The structure and energetics of the tropical cyclone II. Dynamics and energetics. *Monthly Weather Review*, **105 (9)**, 1136–1150.

Grabowski, W. W., and P. K. Smolarkiewicz, 1999: CRCP: A cloud resolving convection parameterization for modeling the tropical convecting atmosphere. *Physica D: Nonlinear Phenomena*, **133 (1)**, 171–178.

Gray, M., J. Petch, S. Derbyshire, A. Brown, A. Lock, H. Swann, and P. Brown, 2004: Version 2.3 of the Met Office Large Eddy Model: Part II. *Scientific documentation. Met Office, Exeter.*

Haertel, P. T., and G. N. Kiladis, 2004: Dynamics of 2-day equatorial waves. *Journal of the Atmospheric Sciences*, **61 (22)**, 2707–2721.

Herbert, C., D. Paillard, and B. Dubrulle, 2013: Vertical temperature profiles at maximum entropy production with a net exchange radiative formulation. *Journal of Climate*, **26 (21)**, 8545–8555.

Herman, M. J., and D. J. Raymond, 2014: WTG cloud modeling with spectral decomposition. *Journal of Advances in Modeling Earth Systems*, **6 (4)**, 1121–1140.

Holloway, C. E., 2017: Convective aggregation in realistic convective-scale simulations. *Journal of Advances in Modeling Earth Systems*, **9 (2)**, 1450–1472.

Holloway, C. E., S. J. Woolnough, and G. M. S. Lister, 2013: The effects of explicit versus parameterized convection on the MJO in a large-domain high-resolution tropical case study. part I: Characterization of large-scale organization and propagation. *Journal of the Atmospheric Sciences*, **70 (5)**, 1342–1369.

Holton, J. R., and G. J. Hakim, 2013: *An introduction to dynamic meteorology.* Academic press.

Huang, J., and M. B. McElroy, 2014: Contributions of the Hadley and Ferrel circulations to the energetics of the atmosphere over the past 32 years. *Journal of Climate*, **27 (7)**, 2656–2666.

Hung, M.-P., J.-L. Lin, W. Wang, D. Kim, T. Shinoda, and S. J. Weaver, 2013: MJO and convectively coupled equatorial waves simulated by CMIP5 climate models. *Journal of Climate*, **26 (17)**, 6185–6214.

Igel, M. R., and A. L. Igel, 2018: The energetics and magnitude of hydrometeor friction in clouds. *Journal of the Atmospheric Sciences*, **75 (4)**, 1343–1350.

Kamieniecki, J. A., M. H. P. Ambaum, R. S. Plant, and S. J. Woolnough, 2018: The implications of an idealized large-scale circulation for mechanical work done by tropical convection. *Journal of the Atmospheric Sciences*, in press.

Kim, Y.-H., and M.-K. Kim, 2013: Examination of the global Lorenz energy cycle using MERRA and NCEP re-analysis 2. *Climate Dynamics*, **40 (5-6)**, 1499–1513.

Kleidon, A., 2016: *Thermodynamic Foundations of the Earth System.* Cambridge University Press.

References

Kuang, Z., 2008a: Modeling the interaction between cumulus convection and linear gravity waves using a limited-domain cloud system–resolving model. *Journal of the Atmospheric Sciences*, **65 (2)**, 576–591.

Kuang, Z., 2008b: A moisture-stratiform instability for convectively coupled waves. *Journal of the Atmospheric Sciences*, **65 (3)**, 834–854.

Leonard, B., M. MacVean, and A. Lock, 1993: Positivity-preserving numerical schemes for multidimensional advection. Technical Memorandum 106055, NASA.

Lorenz, E. N., 1955: Available potential energy and the maintenance of the general circulation. *Tellus*, **7 (2)**, 157–167.

Lovelock, J. E., and L. Margulis, 1974: Atmospheric homeostasis by and for the biosphere: the Gaia hypothesis. *Tellus*, **26 (1-2)**, 2–10.

Mapes, B. E., 2004: Sensitivities of cumulus-ensemble rainfall in a cloud-resolving model with parameterized large-scale dynamics. *Journal of the Atmospheric Sciences*, **61 (18)**, 2308–2317.

Mapes, B. E., and X. Wu, 2001: Notes and correspondence convective eddy momentum tendencies in long cloud-resolving model simulations. *Journal of the Atmospheric Sciences*, **58 (5)**, 517–526.

Marquet, P., 2011: Definition of a moist entropy potential temperature: application to FIRE-I data flights. *Quarterly Journal of the Royal Meteorological Society*, **137 (656)**, 768–791.

Marquet, P., and T. Dauhut, 2018: Reply to the comments of Olivier Pauluis to the paper "a third-law isentropic analysis of a simulated hurricane". *arXiv preprint arXiv:1805.00834*.

Oort, A. H., and J. J. Yienger, 1996: Observed interannual variability in the hadley circulation and its connection to enso. *Journal of Climate*, **9 (11)**, 2751–2767.

Ooyama, K. V., 1982: Conceptual evolution of the theory and modeling of the tropical cyclone. *Journal of the Meteorological Society of Japan*, **60 (1)**, 369–380.

Ozawa, H., and A. Ohmura, 1997: Thermodynamics of a global-mean state of the atmosphere-a state of maximum entropy increase. *Journal of Climate*, **10 (3)**, 441–445.

Ozawa, H., A. Ohmura, R. D. Lorenz, and T. Pujol, 2003: The second law of thermodynamics and the global climate system: a review of the maximum entropy production principle. *Reviews of Geophysics*, **41 (4)**.

Paltridge, G. W., 1975: Global dynamics and climate-a system of minimum entropy exchange. *Quarterly Journal of the Royal Meteorological Society*, **101 (429)**, 475–484.

Paltridge, G. W., 2005: Stumbling into the MEP racket: An historical perspective. *Non-equilibrium Thermodynamics and the Production of Entropy*, Springer, 33–40.

Pascale, S., J. Gregory, M. Ambaum, R. Tailleux, and V. Lucarini, 2012: Vertical and horizontal processes in the global atmosphere and the maximum entropy production conjecture. *Earth System Dynamics*, **3 (1)**, 19–32.

Pauluis, O. M., 2011: Water vapor and mechanical work: A comparison of Carnot and steam cycles. *Journal of the Atmospheric Sciences*, **68 (1)**, 91–102.

Pauluis, O. M., 2016: The mean air flow as Lagrangian dynamics approximation and its application to moist convection. *Journal of the Atmospheric Sciences*, **73 (4)**, 4407–4425.

Pauluis, O. M., A. Czaja, and R. Korty, 2008: The global atmospheric circulation on moist isentropes. *Science*, **321 (5892)**, 1075–1078.

Pauluis, O. M., and J. Dias, 2012: Satellite estimates of precipitation-induced dissipation in the atmosphere. *Science*, **335 (6071)**, 953–956.

Pauluis, O. M., and I. M. Held, 2002a: Entropy budget of an atmosphere in radiative–convective equilibrium. Part I: Maximum work and frictional dissipation. *Journal of the Atmospheric Sciences*, **59 (2)**, 125–139.

Pauluis, O. M., and I. M. Held, 2002b: Entropy budget of an atmosphere in radiative–convective equilibrium. Part II: Latent heat transport and moist processes. *Journal of the Atmospheric Sciences*, **59 (2)**, 140–149.

Pauluis, O. M., and A. A. Mrowiec, 2013: Isentropic analysis of convective motions. *Journal of the Atmospheric Sciences*, **70 (11)**, 3673–3688.

Peixoto, J. P., and A. H. Oort, 1992: *Physics of Climate*. American Institute of Physics.

Peixoto, J. P., A. H. Oort, M. De Almeida, and A. Tomé, 1991: Entropy budget of the atmosphere. *Journal of Geophysical Research: Atmospheres*, **96 (D6)**, 10 981–10 988.

Petch, J. C., P. N. Blossey, and C. S. Bretherton, 2008: Differences in the lower troposphere in two- and three- dimensional cloud-resolving model simulations of deep convection. *Quarterly Journal of the Royal Meteorological Society*, **134 (636)**, 1941–1946.

Philander, S., 1990: *El Niño, La Niña and the Southern Oscillation*. Academic Press, San Diego,

CA.

Piacsek, S. A., and G. P. Williams, 1970: Conservation properties of convection difference schemes. *Journal of Computational Physics*, **6 (3)**, 392–405.

Plant, R. S., 2010: A review of the theoretical basis for bulk mass flux convective parameterization. *Atmospheric Chemistry and Physics*, **10 (8)**, 3529–3544.

Press, W. H., S. A. Teukolsky, W. T. Vetterling, and B. P. Flannery, 2007: Numerical recipes: the art of scientific computing. 2007. Cambridge University Press.

Randall, D., M. Khairoutdinov, A. Arakawa, and W. Grabowski, 2003: Breaking the cloud parameterization deadlock. *Bulletin of the American Meteorological Society*, **84 (11)**, 1547–1564.

Raymond, D., Ž. Fuchs, S. Gjorgjievska, and S. Sessions, 2015: Balanced dynamics and convection in the tropical troposphere. *Journal of Advances in Modeling Earth Systems*, **7 (3)**, 1093–1116.

Raymond, D. J., 2007: Testing a cumulus parametrization with a cumulus ensemble model in weak-temperature-gradient mode. *Quarterly Journal of the Royal Meteorological Society*, **133 (626)**, 1073–1085.

Raymond, D. J., 2013: Sources and sinks of entropy in the atmosphere. *Journal of Advances in Modeling Earth Systems*, **5 (4)**, 755–763.

Raymond, D. J., and X. Zeng, 2005: Modelling tropical atmospheric convection in the context of the weak temperature gradient approximation. *Quarterly Journal of the Royal Meteorological Society*, **131 (608)**, 1301–1320.

Romps, D. M., 2008: The dry-entropy budget of a moist atmosphere. *Journal of the Atmospheric Sciences*, **65 (12)**, 3779–3799.

Romps, D. M., 2012a: Numerical tests of the weak pressure gradient approximation. *Journal of the Atmospheric Sciences*, **69 (9)**, 2846–2856.

Romps, D. M., 2012b: Weak pressure gradient approximation and its analytical solutions. *Journal of the Atmospheric Sciences*, **69 (9)**, 2835–2845.

Romps, D. M., 2013: Rayleigh damping in the free troposphere. *Journal of the Atmospheric Sciences*, **71 (2)**, 553–565.

Schneider, T., 2006: The general circulation of the atmosphere. *Annual Review of Earth and Planetary Sciences*, **34 (1)**, 655–688.

Sentić, S., and S. L. Sessions, 2017: Idealized modeling of convective organization with changing sea surface temperatures using multiple equilibria in weak temperature gradient simulations. *Journal of Advances in Modeling Earth Systems*, **9 (2)**, 1431–1449.

Sentić, S., S. L. Sessions, and Ž. Fuchs, 2015: Diagnosing DYNAMO convection with weak temperature gradient simulations. *Journal of Advances in Modeling Earth Systems*, **7 (4)**, 1849–1871.

Sessions, S. L., S. Sugaya, D. J. Raymond, and A. H. Sobel, 2010: Multiple equilibria in a cloud-resolving model using the weak temperature gradient approximation. *Journal of Geophysical Research: Atmospheres*, **115 (D12)**.

Shaw, N., 1930: *Manual of Meteorology.* Cambridge University Press.

Sobel, A. H., G. Bellon, and J. Bacmeister, 2007: Multiple equilibria in a single-column model of the tropical atmosphere. *Geophysical Research Letters*, **34 (22)**.

Sobel, A. H., and C. S. Bretherton, 2000: Modeling tropical precipitation in a single column. *Journal of Climate*, **13 (24)**, 4378–4392.

Sobel, A. H., J. Nilsson, and L. M. Polvani, 2001: The weak temperature gradient approximation and balanced tropical moisture waves. *Journal of the Atmospheric Sciences*, **58 (23)**, 3650–3665.

Stein, T. H. M., C. E. Holloway, I. Tobin, and S. Bony, 2017: Observed relationships between cloud vertical structure and convective aggregation over tropical ocean. *Journal of Climate*, **30 (6)**, 2187–2207.

Steinheimer, M., M. Hantel, and P. Bechtold, 2008: Convection in Lorenz's global energy cycle with the ECMWF model. *Tellus A*, **60 (5)**, 1001–1022.

Stevens, B., and S. Bony, 2013: What are climate models missing? *Science*, **340 (6136)**, 1053–1054.

Tompkins, A., 2000: The impact of dimensionality on long-term cloud-resolving model simulations. *Monthly Weather Review*, **128 (5)**, 1521–1535.

Trenberth, K. E., and J. M. Caron, 2001: Estimates of meridional atmosphere and ocean heat transports. *Journal of Climate*, **14 (16)**, 3433–3443.

Tribus, M., and E. C. McIrvine, 1971: Energy and information. *Scientific American*, **225 (3)**, 179–188.

References

US Standard Atmosphere, 1976: NOAA-S/T76-1562. *Washington, DC: US Government Printing Office.*

Veiga, J., A. B. Pezza, T. Ambrizzi, V. Brahmananda Rao, S. Franchito, and M. Yoshida, 2013: The energy cycle associated to the Pacific Walker circulation and its relationship to ENSO. *Atmospheric and Climate Sciences*, **03**, 627–642.

von Helmholtz, H., 1891: Paper number V: On atmospheric motions. *Smithsonian Miscellaneous collections. The mechanics of the Earth's Atmosphere. A collection of Translations by Cleveland Abbe*, 78–93.

Waliser, D. E., and Coauthors, 2012: The "Year" of Tropical Convection (May 2008–April 2010): Climate variability and weather highlights. *Bulletin of the American Meteorological Society*, **93 (8)**, 1189–1218.

Wang, S., and A. H. Sobel, 2011: Response of convection to relative sea surface temperature: Cloud-resolving simulations in two and three dimensions. *Journal of Geophysical Research: Atmospheres*, **116 (D11)**, 1–19, d11119.

Wang, S., A. H. Sobel, and Z. Kuang, 2013: Cloud-resolving simulation of TOGA-COARE using parameterized large-scale dynamics. *Journal of Geophysical Research: Atmospheres*, **118 (12)**, 6290–6301.

Wing, A. A., and T. W. Cronin, 2016: Self-aggregation of convection in long channel geometry. *Quarterly Journal of the Royal Meteorological Society*, **142 (694)**, 1–15.

Wing, A. A., and K. A. Emanuel, 2014: Physical mechanisms controlling self-aggregation of convection in idealized numerical modeling simulations. *Journal of Advances in Modeling Earth Systems*, **6 (1)**, 59–74.

Yano, J., 2016: Formulation of the mass-flux convective parameterization. *Parameterization of Atmospheric Convection: Volume 1: Theoretical Background and Formulation*, R. S. Plant, and J.-I. Yano, Eds., Imperial College Press, 195–225.

Yano, J.-I., and M. H. P. Ambaum, 2017: Moist static energy: Definition, reference constants, a conservation law, and effects on buoyancy. *Quarterly Journal of the Royal Meteorological Society*, **143 (708)**, 2727–2734.

Yano, J.-I., and R. S. Plant, 2016: Closure. *Parameterization of Atmospheric Convection: Volume 1: Theoretical Background and Formulation*, R. S. Plant, and J.-I. Yano, Eds., Imperial College

Press, 325–401.

Zeng, X., and Coauthors, 2007: Evaluating clouds in long-term cloud-resolving model simulations with observational data. *Journal of the Atmospheric Sciences*, **64 (12)**, 4153–4177.

Zhang, C., J. Gottschalck, E. D. Maloney, M. W. Moncrieff, F. Vitart, D. E. Waliser, B. Wang, and M. C. Wheeler, 2013: Cracking the MJO nut. *Geophysical Research Letters*, **40 (6)**, 1223–1230.